UNIVERSITY OF SOUTHAMPTON

Faculty of Engineering and the Environment

Direct Numerical Investigations of Dilute Dispersed Flows in Homogeneous Turbulence

by

Aditya Uday Karnik

Thesis for the degree of Doctor of Philosophy

July 2012

UNIVERSITY OF SOUTHAMPTON
Faculty of Engineering and the Environment

Doctor of Philosophy

Direct Numerical Investigations of Dilute Dispersed Flows in Homogeneous Turbulence

by **Aditya Uday Karnik**

ABSTRACT

The motivation for the present work is to investigate particle-laden turbulent flows using accurate numerical simulations. In the present work, the carrier phase is modeled using direct numerical simulations (DNS) and the particles are tracked in a Lagrangian sense. Investigations of both one-way and two-way coupled particulate flows in homogeneous isotropic turbulence have been carried out.

The phenomenon of interest in one-way coupled simulations is *preferential accumulation*, which refers to the tendency of heavy particles in isotropic turbulence to collect in regions of high strain and low vorticity. Several measures and mechanisms of accumulation have been reported in the literature often showing conflicting scaling with particle and fluid parameters. In the present study, accumulation has been quantified using several indicators to give a unified picture. The present work addresses the scaling of preferential accumulation with Reynolds number and suggests that while the spacing between particle clusters does exhibit a dependence on Reynolds number, the structure of particle clusters as viewed by individual particles shows little dependence on Reynolds number. The effect of adding a gravitational settling force on the particles has also been explored. While the gravity force tends to homogenize the particle distribution at low Stokes numbers, at high Stokes numbers it tends to arrange the originally random distribution into streaks in the direction of gravity.

The ability of the Lorentz force to limit preferential accumulation has been the focus of the next part of the study. Charges are placed on particles to produce an electric field when the particles are inhomogeneously distributed. The electric field and thereby the Lorentz force tend to homogenize the particle distribution. It is interesting to note that the particle distribution attains a stationary state determined by the total amount of charge contained in the domain. It is demonstrated that in the presence of gravity, less amount of charge is required to homogenise particle distribution. Good agreement is observed for simulations of settling charged particles with experimental work.

The modification of carrier phase turbulence by particles is studied for mono-sized particles. The non-uniform modification of the fluid energy spectrum by particles has been demonstrated. It is seen that there is an increase in energy at high wavenumbers for microparticles ($St_k < 1$), whereas for high Stokes number particles, energy is damped at all scales. The effect of incorporating two-way coupling on particle distribution has also been reported. It is noted that increasing mass loading leads to attenuation of accumulation at low Stokes numbers while the effect is reversed at higher Stokes numbers.

DECLARATION OF AUTHORSHIP

I, **Aditya Uday Karnik**,
declare that the thesis entitled
Direct Numerical Investigations of Dilute Dispersed Flows in Homogeneous Turbulence
and the work presented in the thesis are both my own, and have been generated by me as a result of my own original research. I confirm that:

- this work was done mainly while in candidature for a research degree at University of Southampton. Part of the work (first year of study) was done while in candidature for a research degree at Imperial College London;
- The code used for this work was originally written by Mr. Stephen Scott as part of his PhD studies[1]. In the present work, the code was used to study certain phenomena in detail. Also the code was extended to include more features;
- where I have consulted the published work of others, this is always clearly attributed;
- where I have quoted from the work of others, the source is always given. With the exception of such quotations, this thesis is entirely my own work;
- parts of this work have been published as:

  Karnik, A. U., Shrimpton J. S., *Destruction of Preferential Accumulation by Lorentz force interaction*, 22^{nd} European conference on Liquid Atomization and Spray Systems, Sep.8-10, 2008, Italy.

  Scott, S.J., Karnik, A.U., Shrimpton, J.S., *On the Quantification of Preferential Accumulation*, International Journal of Heat and Fluid Flow, Vol. 30(4), 789-795, 2009.

  Karnik, A. U., Shrimpton J. S., *Mitigation of Preferential Concentration of Small Inertial Particles in Stationary Isotropic Turbulence Using Electrical and Gravitational Body Forces*, Accepted for publication in Physics of Fluids.

Signed: Aditya Uday Karnik
Date: 10-Jul-2012

Acknowledgements

I am indebted to Dr. John Shrimpton for making this endeavor possible. Without his caring support and encouragement it would have been impossible to take this work to completion. I am also thankful to him for introducing me to the world of multiphase flows.

Contents

List of Figures

List of Tables

Nomenclature

Symbols

$\bar{Q}$	time average of quantity Q	
$\langle Q \rangle$	Eulerian average of quantity Q	
$\tilde{Q}$	Lagrangian average over particle population of quantity Q	
$\mathbf{Q}$	vector quantity Q	
$\hat{Q}(\kappa)$	Fourier coefficient at wave-vector κ of function $Q(\mathbf{x})$	

Roman

$\hat{G}_i$	Fourier transform of non-linear convection term, page 12	ms^{-2}
$\hat{p}_f$	Fourier transform of dynamic pressure, page 12	$\mathrm{m}^2\mathrm{s}^{-2}$
$\hat{S}(\kappa)$	Fourier transform of term on RHS of equation 2.30, page 20	$\mathrm{NC}^{-1}\mathrm{m}^{-1}$
B_{nl}	coefficient for turbulent diffusivity due to non-local diffusion flux, page 79	
c	number of particles in a bin, page 38	
c_0	unspecified matching constant in functional form of radial distribution function, page 43	
c_1	exponent in functional form of radial distribution function, page 43	
c_2	exponent of charge term in functional form of RDF for charged particles, page 79	
D	measure of particle accumulation, page 39	
d_0	diameter of liquid jet, page 105	m
D_2	correlation dimension, page 41	
D_c	measure of particle accumulation, page 39	
d_p	particle diameter, page 18	m
D_{ij}	second-order velocity structure function, page 32	$\mathrm{m}^2\mathrm{s}^{-2}$
D_{LL}	longitudinal structure function, page 32	$\mathrm{m}^2\mathrm{s}^{-2}$
D_{NN}	transverse structure function, page 32	$\mathrm{m}^2\mathrm{s}^{-2}$
e	fluid enstrophy, $\omega_1^2+\omega_2^2+\omega_3^2$, page 37	s^{-2}
$E(\kappa)$	energy spectrum function, page 23	$\mathrm{m}^3\mathrm{s}^{-2}$
e'	relative deviation of local fluid enstrophy, page 37	
e_1	unit vector in x-direction, page 24	
E_i	component of Electric field at the particle location, page 19	NC^{-1}
E_{charge}	energy due to Coulomb interaction at Kolmogorov scales, page 79	$\mathrm{m}^2\mathrm{s}^{-2}$

E_{rms}	RMS magnitude of electric field in the domain, page 80	NC^{-1}
E_{turb}	energy of the Kolmogorov eddies, page 79	m^2s^{-2}
$f(r)$	longitudinal autocorrelation function, page 24	
g	acceleration due to gravity, page 18	$\text{m}\,\text{s}^{-2}$
$g(r)$	radial distribution function, page 40	
$g\left(d_p\right)$	radial distribution function at contact, page 43	
h	bin size, page 38	m
$h(r)$	pair correlation function, page 40	
j	$\sqrt{-1}$, page 11	
k	turbulent kinetic energy, page 23	m^2s^{-2}
L	box length, page 10	m
l_n	clustering length scale, page 41	m
L_{11}	Longitudinal integral length scale, page 24	m
$ln(x)$	Natural logarithm of x	
m	number of modes in an annular shell in wavenumber space, page 23	
$m(n)$	node density, page 23	
m_p	mass of particle, page 19	kg
N	Number of grid points, page 11	
n	particle number density, page 38	m^{-3}
$N(r)$	number of particles within a sphere of radius r centered on a base particle, page 41	
n'	relative deviation of local particle number density, page 37	
N_b	total number of bins, page 39	
N_p	total number of computational particles in a simulation, page 21	
n_p	number of particles in a bin, page 38	
N_s	number of real particles in a computational parcel for the charged particle simulations, page 19	
$N_b(c)$	number of bins with c particles, page 39	
P	total number of possible particle pairs , page 40	
p_f	fluid pressure, page 10	$\text{N}\,\text{m}^{-2}$
p_r	probability of finding two particles at a distance less than r, page 41	
P_{ik}	Projection tensor, page 12	
$P_m(c)$	measured probability of finding bins with c particles, page 38	
$P_p(c)$	probability of finding bins with c particles for a random particle distribution, page 39	
P_r	number of particle pairs with separation $r \pm \Delta r/2$, page 40	
Q	local charge density, page 19	Cm^{-3}
Q_0	initial volume charge density, page 105	Cm^{-3}
q_p	electric charge on a particle, page 19	C
Q_R	Rayleigh limit, page 19	C

Q_v	bulk charge density, page 19	Cm^{-3}
Q_z	volume charge density at section z, page 109	Cm^{-3}
r	scalar separation distance between two points, page 23	m
R^2	second invariant of rate of rotation tensor averaged over ensemble of particle trajectories, page 43	s^{-2}
R_{ij}	two-point correlation, page 23	$\mathrm{m}^2\mathrm{s}^{-2}$
$R_{lp,i}$	Lagrangian autocorrelation of particle velocity $u_{p,i}$, page 63	
Re_p	particle Reynolds number, page 18	
S^2	second invariant of rate of strain tensor averaged over ensemble of particle trajectories, page 43	s^{-2}
S_ϵ	dissipation skewness, page 25	
t	time	s
$t(r)$	transverse autocorrelation function, page 24	
T_E	eddy turnover time, page 24	s
T_L	forcing time-scale, page 15	s
u'	RMS turbulence velocity (also referred to as turbulence intensity), page 24	ms^{-1}
u_1	instantaneous fluid velocity component in x-direction, page 24	ms^{-1}
u_2	instantaneous fluid velocity component in y(or z)-direction, page 24	ms^{-1}
V	volume of domain , page 40	
V_b	bin volume, page 38	m^3
v_c	Coulomb velocity, page 80	ms^{-1}
v_c	non-dimensional Coulomb velocity, page 80	
v_g	gravitational settling velocity, page 26	$\mathrm{m\,s}^{-1}$
v_p	volume of computational particle (parcel) in two-way coupled simulations, page 21	m^3
x_E	electrical length scale, page 95	m
$x_{\min}$	distance to nearest particle, page 94	m
$\mathbf{a}_p$	particle acceleration due to drag force, page 21	ms^{-2}
$\mathbf{f}_c$	coupling force (per unit volume) exerted by particles on fluid, page 10	$\mathrm{N\,m}^{-3}$
$\mathbf{f}_d$	drag force on the particle, page 20	N
$\mathbf{f}_e$	Coulomb force per unit mass on the particle, page 18	ms^{-2}
$\mathbf{r}$	separation vector between two points in two-point correlation, page 23	m
$\mathbf{u}_f$	instantaneous fluid velocity, page 10	$\mathrm{m\,s}^{-1}$
$\mathbf{x}$	position	m
Re_λ	Taylor Reynolds number, page 25	
St_k	particle Stokes number, page 25	
T_L^*	non-dimensional forcing time-scale, page 15	

Greek

α_p	particle volume fraction, page 3	

Δ	grid spacing, page 11	m
δ_{ik}	Kronecker delta function, page 12	
Δt	time-step, page 12	s
ΔV_r	volume of the shell of thickness Δr and mean radius r, page 40	
ΔV	Control volume surrounding a node (= Δ^3), page 20	m^3
ϵ	dissipation rate, page 23	$m^2 s^{-3}$
ϵ_0	permittivity of free space, page 19	$N^{-1} m^{-2} C^2$
η	Kolmogorov length scale, page 24	m
γ	surface tension coefficient, page 19	$N m^{-1}$
κ	scalar wavenumber magnitude, page 23	m^{-1}
κ_0	lowest resolved wavenumber, page 11	m^{-1}
λ	mean number of particles in a bin, page 39	
λ_t	transverse Taylor length scale, page 25	m
ν_f	fluid kinematic viscosity, page 10	$m^2 s^{-1}$
Φ_{ij}	velocity spectrum tensor, page 23	$m^3 s^{-2}$
ϕ_p	particle mass loading, page 4	
ϕ_v	particle volume loading, page 48	
ρ_f	material density of fluid phase, page 4	$kg m^{-3}$
ρ_p	material density of particle phase, page 4	$kg m^{-3}$
σ	forcing amplitude, page 15	$m s^{-2}$
σ_m	standard deviation of measured particle distribution from an uniform distribution, page 39	
σ_p	standard deviation of random particle distribution from an uniform distribution, page 39	
σ_n	standard deviation of particle Reynolds number distribution over total number of particles, page 51	
τ_k	Kolmogorov time scale, page 24	s
τ_p	particle response time, page 18	s
θ	spray half-angle, page 105	
κ	wave-vector, page 11	m^{-1}
ω	fluid vorticity, $\nabla \times \mathbf{u}_f$, page 37	s^{-1}

Subscripts

Q_f	quantity Q associated with fluid phase
Q_i	Cartesian notation of vector quantity $\mathbf{Q}$
Q_p	quantity Q associated with particle phase

Superscripts

Q^*	non-dimensional quantity Q
Q^c	complex conjugate of Q
Q'	fluctuating component ($Q' = Q - \langle Q \rangle$)

Abbreviations

CFL	Courant-Friedrichs-Levy
DNS	Direct Numerical Simulations
EE	Eulerian-Eulerian
EL	Eulerian-Lagrangian
HIT	Homogeneous Isotropic Turbulence
LES	Large-eddy simulation
LHS	Left Hand Side
PSIC	Particle-Source-in-Cell
RDF	Radial Distribution Function, $g(r)$
RHS	Right Hand Side
RK3	Third order Runge-Kutta integration scheme
RMS	Root Mean Square

Chapter 1

Introduction

The general area of interest of this investigation is the dispersion of heavy particles in a turbulent flow. In this chapter, the general problem of interest is initially introduced. The particular phenomena of interest to the present work are highlighted here along with the situations where these phenomena may play a dominant role. The present work involves computational modeling and thus inevitably invokes several simplifying assumptions. These assumptions are mentioned here to clarify the domain of applicability of the present work. A background on previous attempts to study dispersion of particles in turbulent flows is then provided followed by an outline of the organisation of the rest of this report.

Dispersed multiphase flows are encountered in industrial, environmental and even astrophysical settings. Such flows are encountered in many energy conversion processes and chemical processing units. Some particular examples are fluidized bed reactors and inside combustion chambers of automobile engines. Fluidized bed reactors are a classic example of multiphase flows. It is noted that as yet their design is based mostly on empirical formulae derived from experience rather than a sound understanding of the physics of the flow. Similar is the case for electrostatic precipitators, which are used to remove pollutant particles from the exhaust of power plants. Another problem of interest is the dispersion of pollutants once they are released into the atmosphere. It would be useful to predict the concentration of pollutants at certain distances downstream of the source. The recent disruptions in airline traffic caused by the volcanic ash cloud are also a pertinent ex-

ample in this context.

The fundamental problem of interest is to understand how mixing of particles occurs in a turbulent flow. Turbulent flows are typically well-known for their mixing properties. However mixing of inertial particles in a turbulent medium is not so straight-forward and it has been observed that there are regimes of flow which can lead to inhomogeneous particle distributions. This de-mixing of particles is typically referred to as preferential accumulation. Particularly, preferential accumulation in a dilute suspension of heavy inertial particles in isotropic turbulent is addressed in the present work. Clustering of heavy inertial particles in turbulent flows occurs at different length scales depending on particle and fluid parameters. The fluid parameter of interest is typically the Reynolds number, signifying the relative importance of inertial and viscous effects in a flow. In the present work, the length scales associated with particle clusters are quantified using different measures. This quantification helps to study the scaling of preferential accumulation with the Reynolds number of the fluid turbulence. The study of this scaling is important to understand the phenomenon of clustering of particles in high Reynolds number situations. In many situations, gravity play a predominant role in the dispersion of particles. In the present work, the effect of gravity on dispersion characteristics of particles is also addressed.

Among the implications of preferential accumulation, perhaps the most highlighted one is its role in rain initiation by droplet collision in atmospheric clouds [11]. It is thought that agglomeration of droplets in clouds is enhanced due to accumulation of droplets. Preferential accumulation also has implications for the combustion process inside automobile engines. It is known that improper mixing of air and fuel droplets in the combustion chamber of a compression ignition engine leads to increased emissions of particulate pollutants. Thus the efficient combustion of fuel droplets in the combustion chamber is also a problem of interest to the present work. Accumulation is also thought to have played an important role in planet formation in the early solar system [12]. The impact of accumulation on settling velocities of inertial particles has also been widely investigated [13, 14]. Once the phenomenon of accumulation of particles is understood, the next step is to investigate ways to control this phenomenon. To this end, charging of particles has been systematically investigated in the present work. The relative significance of the gravitational and Coulomb body forces is studied systematically. The modification of carrier phase turbulence to

the presence of particles has also been addressed in the present work.

The work in the present thesis is limited to incompressible, isothermal flows without phase change or particle-particle collisions. The carrier flow configuration is limited to stationary homogeneous isotropic turbulence (HIT). The condition of stationary isotropy allows a reduction in the complexity of the analysis and lends itself to rigorous analysis - both theoretically and numerically. The motivation for these studies hinges on the assumption of statistical homogeneity, isotropy and universality of the small scales of turbulence. The Eulerian-Lagrangian formulation for dilute dispersed multiphase flows has been employed here. The carrier phase being continuous has been modeled in the Eulerian sense while the particles are tracked in Lagrangian sense. In the present work, the carrier phase turbulence is *accurately* resolved using DNS. The trajectories of up to a million particles are tracked and statistics of their positions and velocities (among other things) have been collected. Point-particle DNS has proved to be a valuable tool for probing phenomenon associated with dispersed flows. Collisions between particles have been neglected in the present work and thus the applicability of the present work is limited to dilute suspensions.

Particulate flows can be classified under several regimes depending on the dominant phenomenon in the flow. To clarify the regime considered in this work, the relevant parameters of interest are introduced here. One of the primary parameters governing the dynamics of particulate flows is the volume fraction of the particles, α_p. For a mixture of particles in a volume δV, volume fraction α_p is defined as [15],

$$\alpha_p = \lim_{\delta V \to \delta V^o} \frac{\delta V_p}{\delta V}, \tag{1.1}$$

where δV_p is the volume of the particles in volume δV and δV^o is the limiting volume that ensures a stationary average. Depending on the volume fraction of particles, particle-laden flows can be broadly classified into three categories, namely (1) collision-free flow, (2) collision-dominated flow and (3) contact-dominated flow. The present work is limited to collision-free or "dilute" particle-laden flows. It is assumed here that the time period between collisions of particles is much larger than the momentum response time of the particles and thus the collision interactions can be neglected. The present simulations have been restricted to the regime $\alpha_p \leq 10^{-2}$. The material density of the particle phase is denoted by ρ_p, while that of fluid phase is denoted by ρ_f. In the present work, the particles are much denser than the carrier fluid i.e. $\rho_p/\rho_f \sim \mathcal{O}(10^3)$. Thus in the present

work, though the volume fraction of the particles in the domain is small, the mass of the particles can be significant owing to the high density ratio. The mass loading (sometimes referred to as mass fraction) of the particles, ϕ_p, is defined as,

$$\phi_p = \alpha_p \frac{\rho_p}{\rho_f}. \tag{1.2}$$

At sufficiently large mass fractions, the momentum exchange between the dispersed and carrier phases alters the properties of carrier phase turbulence. This is typically referred to as two-way coupling and has also been addressed in the present work. A detailed exposition on the factors governing coupling between phases can be obtained from Crowe et al. [15]. The point-particle assumption requires the particles to be smaller than the smallest fluid length scales such that the flow around the particles is smooth. Particle wakes are not resolved in the present work. Also the drag law used for modeling the fluid-particle interaction implies that the flow around the particles is in the viscous regime and Reynolds numbers based on particle diameter are moderately low ($Re_p \leq 800$).

1.1 Background

Modeling dispersed flows is challenging due to the broad range of length and time scales associated with these flows. In practical situations, particles rarely appear in well-defined shapes and sizes and it is common practice to use the spherical particle approximation along with a equivalent nominal particle diameter. The length scales range from the nominal particle diameters to the length scale associated with largest vortical structures in the carrier fluid. Similarly the time-scales vary from the time it takes the particles to respond to ambient flow (which can be a fraction of the time-scale associated with the smallest eddies in the flow) to the time-scale of the largest eddies in the flow. The fundamental difficulty associated with modeling these flows arises from our yet incomplete understanding of single-phase turbulence[16]. The presence of particles or a dispersed-phase only serves to complicate the situation. It is common among researchers of single-phase turbulence to make simplifying assumptions in order to make the flow equations amenable to rigorous theoretical analysis. One such example is the analysis of homogeneous tur-

bulent flow subjected to rapid distortion by Batchelor and Proudman [17]. In a homogeneous flow, the statistical properties of turbulence are invariant to linear displacements of the co-ordinate system. A further simplification can be made by assuming the fluid velocity field $\mathbf{u}_f$ to be statistically invariant under reflections and rotations of the co-ordinate system. Such a class of turbulent flow is referred to as homogeneous isotropic turbulence (HIT). It is particularly educative to study HIT since it can be well approximated in wind-tunnel experiments. Also, according to Kolmogorov's hypothesis[18], the small scales of turbulence at high Reynolds numbers are supposed to be statistically isotropic. In view of our theoretical understanding of isotropic turbulence and also its accessibility to both well-defined numerical as well as experimental analysis, the present work is limited to simulations of HIT.

Here the different approaches to modeling single-phase fluid turbulence are briefly discussed, followed by a discussion on modeling approaches for dispersed-phase flows. Modeling single-phase turbulence continues to present challenges at the theoretical level due to its complexity [16]. There are three main approaches to modeling single-phase turbulence. In the direct numerical simulation (DNS) approach, all the scales of the flow are resolved and no ad-hoc modeling is used to solve the Navier-Stokes equations [19]. However it is computationally expensive to resolve all the scales, especially at the high Reynolds numbers associated with practical applications. DNS is thus limited to low Reynolds numbers. An intermediate approach is to resolve only the larger scales and model the effect of the unresolved scales on the resolved quantities. This approach is typically referred to as large-eddy simulation (LES). It is believed that the small scales of turbulence are more universal, in the spirit of Kolmogorov's theory, and justifies their modeling in a universal way. LES allows higher Reynolds numbers to be accessible to numerical solution, while at the same time retaining some accuracy. In the Reynolds averaged Navier-Stokes (RANS) approach, all the turbulent scales are modeled, allowing computations of practical flows. The RANS models are typically tuned to particular flow situations and lack universal applicability.

The presence of particles adds another level of complexity from a modeling point of view. Ideally we would like to resolve the flow field around each individual particle and calculate the forces acting on it by integrating the skin friction and pressure forces on its surface. Elghobashi [2] notes the major challenges facing simulation of dispersed-phase flows - (i) presence of a wide range of time

and length scales and (ii) enormous computational requirements to resolve flow around individual particles. The different regimes of dispersed flows based on particle parameters are shown in Figure 1.1 (reproduced from Elghobashi [2]). Numerical methods suffer from the lack of computing power to resolve the vast range of scales present in dispersed flows. With the present computing power, it is not possible to resolve the flow around large numbers of individual particles. This inevitably calls for simplifying assumptions to be invoked to make the problem numerically tractable. Modeling approaches for dispersed-phase flows can be broadly categorized into two classes viz. Eulerian-Lagrangian(EL) and Eulerian-Eulerian(EE). In the EL approach (sometimes referred to as the "trajectory" approach), the carrier phase is modeled in an Eulerian sense while the particles are tracked individually in the Lagrangian sense. The particle trajectory is tracked by integrating the particle equation of motion. On the other hand, in the EE approach, the particles are modeled as a separate inter-penetrating phase with its associated continuum transport equations. Suitable models are used based on particle sizes and volume fractions to describe the interaction between the two phases in the EE approach. Both the approaches and their merits and de-merits are discussed in the review by Mashayek and Pandya [20]. It is natural to model particles in the Lagrangian sense owing to our fairly good understanding of forces acting on an individual particle. The EL approach, though computationally expensive, involves comparatively less ad-hoc modeling (for the particle phase) and is used here.

1.2 Thesis outline

The rest of the thesis is organized into chapters as follows:

Chapter 2 describes the numerical approach adopted in this study and gives details of the PANDORA code used for computations in this study. This chapter also describes the initial simulations done using PANDORA to validate the code.

Chapter 3 describes the work related to preferential accumulation of particles. A literature survey of studies investigating this phenomenon is also included in this chapter. The effect of gravitational body force on particles is also systematically addressed in this chapter.

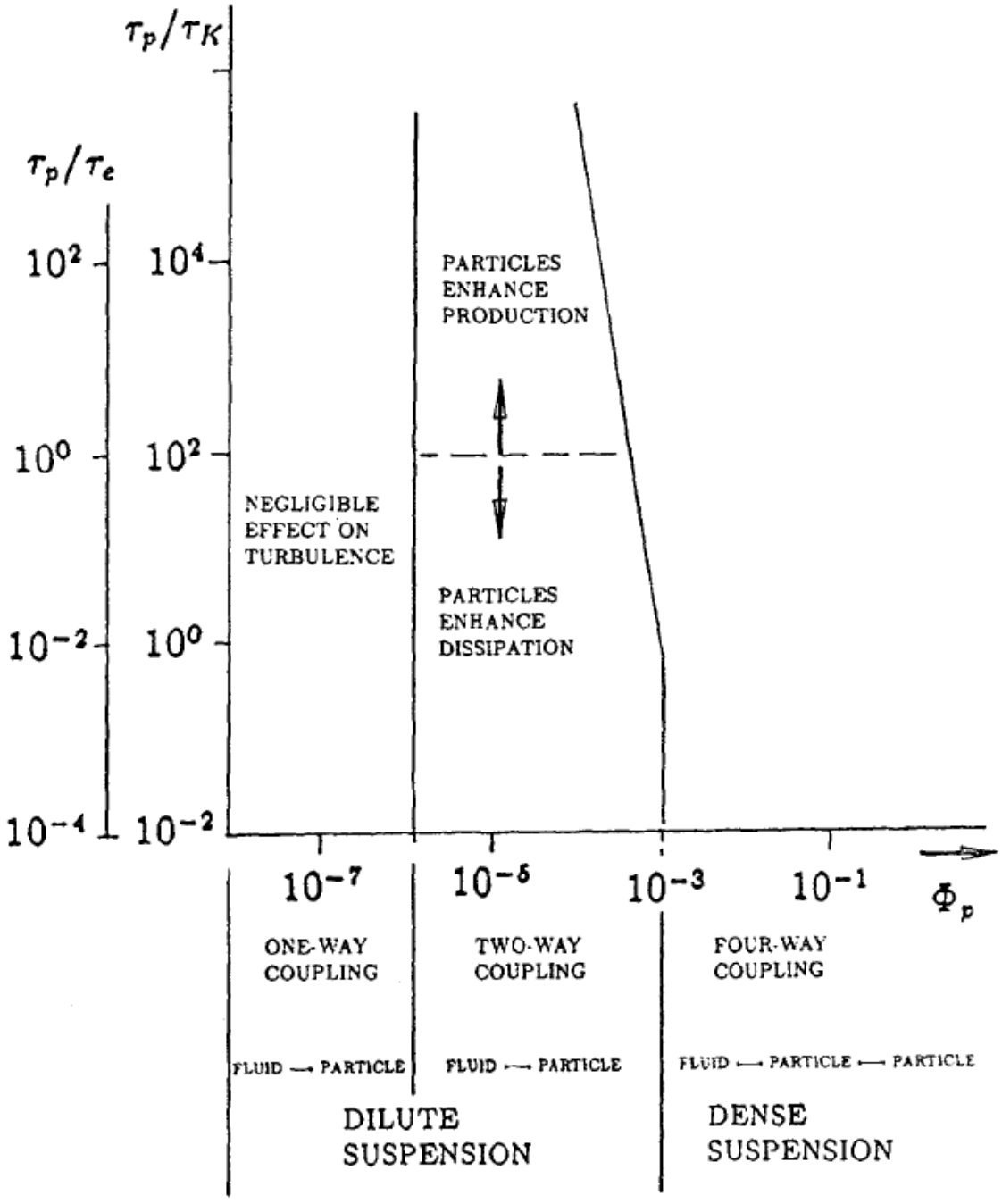

Figure 1.1: Map of regimes of interaction between particles and turbulence (reproduced from Elghobashi [2]). In this figure, τ_p, τ_e and τ_K represent the particle response time, eddy turnover time and Kolmogorov time scales respectively; Φ_p represents the volume fraction of particles.

Chapter 4 describes the work done on controlling accumulation using charges on particles.

Chapter 5 describes the work related to modification of carrier phase turbulence due to presence of particles (two-way coupling).

Finally, chapter 6 summarises the outcomes of the present study and discusses the potential avenues for further research using PANDORA .

Chapter 2

Numerical method and implementation

A point-particle pseudo-spectral DNS code (named PANDORA) is used to simulate motion of small, heavy particles in forced homogeneous isotropic turbulence (HIT). PANDORA was originally developed by Scott [1] as a tool to validate the maximum entropy method used for closure of Eulerian particle models. It was originally developed as a one-way coupled code neglecting the effect of particles on the fluid turbulence. Presently PANDORA can also account for the back effect of particles on fluid turbulence (two-way coupling). In the present work, PANDORA has also been extended to include electrostatic charge and thus a corresponding Coulomb force on the particles.

With the advent of supercomputers, a large body of work has focussed on numerical modeling of turbulent flows (see review by Rogallo and Moin [21]). One of the widely used research tools for studying turbulent flows is direct numerical simulations (DNS) [19]. DNS of isotropic turbulence was first carried out by Orszag and Patterson [22] and used for analysis of particle-laden flows by Riley and Patterson [23]. However isotropic turbulence is inherently decaying in nature and thus the turbulent kinetic energy is eventually completely dissipated in absence of energy input. For the purpose of the present study, it is desirable to deal with stationary flows allowing statistics to be collected over long averaging periods. In the present code, stationarity is achieved by means of addition of a forcing acceleration at large scales. The details of the forcing scheme are presented later in section 2.1.5. The present form of the code derives itself from the algorithm for simulation of homogeneous flows employed by Rogallo [24].

The rest of the chapter is organised as follows. The details of numerical simulation of fluid phase are presented in section 2.1. The particle phase implementation is described in section 2.2. The averaging conventions used to define the different quantities obtained from the simulations are described in section 2.3. Results of preliminary validation runs using PANDORA are presented in section 2.4.

2.1 Fluid phase implementation

2.1.1 Governing equations

All simulations in this study are limited to an incompressible carrier phase and hence only the mass and momentum conservation equations are invoked. The governing equations in physical space are,

$$\frac{\partial u_{f,i}}{\partial x_i} = 0\,, \tag{2.1}$$

$$\frac{\partial u_{f,i}}{\partial t} + u_{f,k}\frac{\partial u_{f,i}}{\partial x_k} = -\frac{1}{\rho_f}\frac{\partial p_f}{\partial x_i} + \nu_f \frac{\partial^2 u_{f,i}}{\partial x_k x_k} + \frac{1}{\rho_f} f_{c,i}\,, \tag{2.2}$$

where $\mathbf{u}_f$ is the instantaneous fluid velocity, p_f is the pressure, ν_f is the fluid kinematic viscosity, ρ_f is the fluid material density and $\mathbf{f}_c$ is the force (per unit volume) exerted by the particles on the fluid (two-way coupling). Throughout the present work, we deal with stationary turbulence and thus the explicit dependence of all quantities on time is omitted. Also, the forcing acceleration term in the momentum equation has been dropped in equation 2.2.

Equations 2.1 and 2.2 are solved on a cube of side $L = 2\pi$ using the pseudospectral method with periodic boundary conditions in all three directions.

2.1.2 Pseudo-spectral method

Pseudo-spectral methods have been widely used for direct numerical simulations of homogeneous isotropic flows beginning with the work of Orszag and Patterson [22].

The fluid velocity field is represented as the three-dimensional Fourier series

$$\mathbf{u}_f(\mathbf{x}) = \sum_{\kappa} e^{j\kappa.\mathbf{x}} \hat{u}_f(\kappa), \tag{2.3}$$

where $j = \sqrt{-1}$, κ is the wave-vector and the summation is over all the resolved wavenumbers in the simulation.

In physical space, the discrete fluid velocity field in a cube of side L is represented at N grid points in each direction. The co-ordinates of the grid points in (say) the x-direction are given by

$$x_{1,p} = p\Delta, \qquad p = 0, 1, 2, ..., N-1, \tag{2.4}$$

where $\Delta = L/N$ is the grid spacing. In the present work, the number of grid points in each co-ordinate direction is the same and thus $\Delta = \Delta x = \Delta y = \Delta z$. For N grid points in one direction, the corresponding N wavenumbers or components of wave-vector in any one direction (say x-direction) are given by

$$\kappa_1 = k\kappa_0, \qquad k = -N/2+1, -N/2+2, ...0, 1, 2..., N/2, \tag{2.5}$$

where $\kappa_0 \equiv 2\pi/L$ is the lowest resolved wavenumber. In the present work, κ_0 is unity since cube of side $L = 2\pi$ is employed. Assuming equal number of grid points in each direction, the velocity components in Fourier space are given by

$$\hat{u}_i(\kappa) = \frac{1}{N^3} \sum u_i(\mathbf{x}) e^{-j\kappa.\mathbf{x}}, \tag{2.6}$$

where the summation is over all the N^3 grid points in physical space.

In Fourier space, the continuity and momentum equations (equations 2.1 and 2.2) reduce to

$$\kappa.\hat{\mathbf{u}}(\kappa) = 0, \tag{2.7}$$

$$\frac{\mathrm{d}\hat{u}_{f,i}}{\mathrm{d}t} + \nu_f \kappa^2 \hat{u}_{f,i} = -j\kappa_i \hat{p}_f - \hat{G}_i, \tag{2.8}$$

where $\hat{p}_f$ is the Fourier coefficient of the dynamic pressure p_f/ρ_f and $\hat{G}_i$ is the Fourier coefficient of the non-linear convection term (second term on LHS of equation 2.2). Using equation 2.7, the momentum equation in Fourier space can be further reduced to

$$\frac{\mathrm{d}\hat{u}_{f,i}}{\mathrm{d}t} = -\nu_f \kappa^2 \hat{u}_{f,i} - P_{ik}\hat{G}_k, \tag{2.9}$$

where the projection tensor P_{ik} is

$$P_{ik} = \delta_{ik} - \frac{\kappa_i \kappa_k}{\kappa^2}. \tag{2.10}$$

2.1.3 Time stepping

The third order Runge-Kutta scheme (RK3) is used for numerical integration of equation 2.9 in time. RK3 involves two intermediate evaluations of the velocity as well as its temporal derivative, $F(\mathbf{u})$. The subscript f and superscript $\hat{}$ for the velocity $\mathbf{u}$ is dropped here since the same RK3 scheme is used to integrate the equation for particle velocity. For the purpose of evaluating the fluid velocity, $F(\mathbf{u})$ represents the RHS of equation 2.9 calculated using velocity $\mathbf{u}$. The procedure of the RK3 scheme is outlined below. The focus is on showing how the velocity field at the $(n+1)^{\text{th}}$ time-step, $\mathbf{u}_{n+1}$, is evaluated from that at the n^{th} time-step, $\mathbf{u}_n$, where the time-step size is Δt. The subscripts 'rk1' and 'rk2' are used here to denote the values at the two intermediate steps. The values at the first intermediate step are given by

$$\mathbf{u}_{\text{rk1}} = \mathbf{u}_n + \frac{1}{3}\Delta t\, F(\mathbf{u}_n), \tag{2.11}$$

$$F_{\text{rk1}} = -\frac{5}{9}F(\mathbf{u}_n) + F(\mathbf{u}_{\text{rk1}}). \tag{2.12}$$

The values at the second intermediate step are given by

$$\mathbf{u}_{\mathrm{rk2}} = \mathbf{u}_{\mathrm{rk1}} + \frac{15}{16}\Delta t\, F_{\mathrm{rk1}}, \tag{2.13}$$

$$F_{\mathrm{rk2}} = -\frac{153}{128}F_{\mathrm{rk1}} + F(\mathbf{u}_{\mathrm{rk2}}). \tag{2.14}$$

The final value of velocity at the $(n+1)^{\mathrm{th}}$ time-step, $\mathbf{u}_{n+1}$, is then given by

$$\mathbf{u}_{n+1} = \mathbf{u}_{\mathrm{rk2}} + \frac{8}{15}\Delta t\, F_{\mathrm{rk2}}. \tag{2.15}$$

It should be noted that the fluid velocity field so obtained, $\hat{\mathbf{u}}_f$, is corrected to enforce the continuity equation 2.7. The intermediate velocity fields are also corrected in similar manner.

The time-step Δt used in the simulations is governed by the Courant-Friedrichs-Levy (CFL) number. The CFL number in all simulations in the present study is 0.75. Thus the time-step, $\Delta t = 0.75\,\Delta t_{\mathrm{CFL}}$ for all simulations, where

$$\Delta t_{\mathrm{CFL}} = \frac{\Delta}{(|u_{f,1}| + |u_{f,2}| + |u_{f,3}|)_{\max}}. \tag{2.16}$$

In equation 2.16, $u_{f,1}$, $u_{f,2}$, $u_{f,3}$ are the three components of the fluid velocity at a particular node and the denominator represents the maximum value of $(|u_{f,1}|+|u_{f,2}|+|u_{f,3}|)$ among all the nodes. The time-step for all simulations is much lower than the Kolmogorov time-scale of the fluid turbulence, as reported in table 2.3.

2.1.4 Removal of aliasing errors

In the pseudospectral algorithm, the non-linear term is evaluated in real space due to the prohibitive cost associated with calculating the convolution sums in Fourier space. In one dimension, the direct summation implies $\mathcal{O}(N^2)$ operations. In three dimensions, the cost is $\mathcal{O}(N^4)$ operations, provided the tensor product nature of multidimensional spectral approximations is utilised as discussed in Orszag [25] [26]. In the present work, the FFTW [27] library is used which enables the non-linear term to be evaluated in $\mathcal{O}(N\log_2 N)$ operations in one dimension ($\mathcal{O}(N^3\log_2 N)$ op-

erations in three dimensions assuming equal number of grid points in each direction). The aliasing errors associated with evaluating the non-linear term in real space are removed by setting the modes with wavenumber magnitude of any one component greater than $N/3$ to zero both prior to and after the transform operation. The magnitude of the maximum resolved wavenumber in the simulations is thus $\kappa_{\max} = N/\sqrt{3}$.

2.1.5 Forcing scheme

Homogeneous isotropic turbulent flows are essentially decaying in nature. Energy is continuously dissipated at the small scales of these flows. Numerical investigation of stationary, isotropic turbulence requires some form of energy input, at the large scales, to allow smaller scales to develop and dissipate *realistically*. Thus energy must continuously be added at large scales in an unbiased fashion to maintain stationarity. In this section the calibration of a forcing scheme developed by Eswaran and Pope [28], which is implemented in the present code, is described.

In a turbulent flow with a wide separation between the large and small scales, the Kolmogorov hypotheses [18] support the assumption that the small-scale statistics are not influenced by the mechanism of energy production at large scales. The forcing method of Eswaran and Pope [28] is elaborated here keeping in mind that future users of PANDORA need to estimate forcing parameters for high Reynolds number simulations.

The forcing of large scales is essentially achieved by adding a forcing acceleration $\hat{\mathbf{a}}^F(\kappa, \mathbf{t})$ to the low wave-number band of Navier-Stokes equation in Fourier space

$$\frac{\partial \hat{\mathbf{u}}_f(\kappa, t)}{\partial t} = \hat{\mathbf{a}}(\kappa, t) + \hat{\mathbf{a}}^F(\kappa, t), \tag{2.17}$$

where $\hat{\mathbf{a}}(\kappa, t)$ represents all spatial terms of the Navier-Stokes equation (RHS of equation 2.9). All nodes within a sphere of radius K_F (excluding the node at the origin) are subjected to this additional stochastic acceleration.

The forcing acceleration is specified according to an Uhlenbeck-Ornstein stochastic process

$$\hat{\mathbf{b}}(\kappa, t+\Delta t) = \hat{\mathbf{b}}(\kappa, t)\left(1 - \frac{\Delta t}{T_L}\right) + \hat{\theta}\left(\frac{2\sigma^2 \Delta t}{T_L}\right)^{\frac{1}{2}}, \tag{2.18}$$

where σ is the forcing amplitude and T_L is a forcing time-scale. The stochastic process represents a vector of three independent complex stochastic processes with complex random vector $\hat{\theta}$. Each component of $\hat{\theta}$ conforms to a Gaussian distribution with a mean of zero and standard deviation of one. Continuity is satisfied by projection of $\hat{\mathbf{b}}(\kappa, t)$ onto the plane normal to κ

$$\hat{\mathbf{a}}^F(\kappa, t) \equiv \hat{\mathbf{b}}(\kappa, t) - \frac{\kappa}{|\kappa|}\kappa \cdot \hat{\mathbf{b}}(\kappa, t). \tag{2.19}$$

Thus the forcing is governed by the forcing amplitude σ and the forcing time-scale T_L. The procedure to estimate these parameters, as described by Eswaran and Pope [28], involves making arbitrary choices for viscosity, ν_f, and non-dimensional forcing time-scale, $T_L^* \equiv T_L^{4/3}(\sigma\kappa_0)^{2/3}$. The choice of these parameters is by no means obvious and appropriate values for these parameters can only be inferred from the data presented in literature using this particular forcing scheme ([28],[10],[29]). The objective of the forcing exercise is to obtain a flow with the desired Reynolds number, Re_λ and Kolmogorov length-scale, η. To obtain these flow-characterizing parameters, one needs to specify the following input parameters - κ_0, the lowest wavenumber; $\kappa_{\max}$, the highest wavenumber; κ_F, the maximum wavenumber of forced modes; ν_f, the kinematic viscosity of the fluid and a non-dimensional forcing time-scale T_L^*. The smallest scales resolved by the computations are of the order of $(1/\kappa_{\max})$ while the smallest turbulent scales are of the order of the Kolmogorov length scale η. Thus, the non-dimensional quantity $\kappa_{\max}\eta$ is an indicator of the spatial resolution of a given grid. Higher the value of this quantity, better is the spatial resolution of the grid. Studies by Eswaran and Pope [28] indicate that values of $\kappa_{\max}\eta$ near unity are near the limit of good resolution. $\kappa_{\max}$ is governed by the dealiasing scheme being employed to remove aliasing errors as described in section 2.1.4.

Here the step-by-step procedure followed to calculate the forcing amplitude σ and forcing time-scale T_L is described. Whenever required, arbitrary choices for parameters have been made based on data provided in Overholt and Pope [30]. It should be noted that different approaches to select

the forcing parameters have been tried in the literature in order to obtain the desired turbulence characteristics. In their recent work, Yeung et al. [29] updated the forcing parameters from their previous work [10] in order to use the same forcing amplitude, σ, for all simulations.

The summary is as follows:

- Choose radius of the sphere within which nodes are to be forced i.e. κ_F. The typical values of κ_F used in literature are $\sqrt{2}\kappa_0$ or $2\sqrt{2}\kappa_0$ ([28],[10]). For all simulations in the present work, the maximum wavenumber of forced modes, $\kappa_F = 2\sqrt{2}\kappa_0$.
- Calculate the number of forced nodes N_F based on the chosen value of κ_F. N_F is the number of wave-vectors $\kappa(\kappa_1,\kappa_2,\kappa_3)$ such that their magnitude, $|\kappa| = \sqrt{\kappa_1^2+\kappa_2^2+\kappa_3^2}$ is less than the forcing radius, κ_F. For the above-mentioned values of κ_F, i.e. $\sqrt{2}\kappa_0$ and $2\sqrt{2}\kappa_0$, the corresponding values of N_F are 18 and 92 respectively.
- The radius of the sphere containing the physically significant wave-numbers, $\kappa_{\max}$, depends on the dealiasing scheme being employed. In the present work, the $2/3^{rd}$ rule has been employed for dealiasing, resulting in $\kappa_{\max} = N/\sqrt{3}$.
- Choose the value of the parameter $\kappa_{\max}\eta$ to obtain *good* spatial resolution. Knowing $\kappa_{\max}$ from the previous step - allows for estimation of the predicted Kolmogorov microscale η.
- The predicted Reynolds number can be estimated by the empirical relation [28]:

$$Re_\lambda \approx \frac{8.5}{\left(\eta\kappa_0\right)^{5/6} N_F^{2/9}}. \tag{2.20}$$

  It is also possible to specify a target Reynolds number, roughly equal to the predicted Reynolds number, and work out the Kolmogorov length scale, η (and thus the non-dimensional resolution $\kappa_{\max}\eta$). Obviously, any target Reynolds number less than the predicted Reynolds number would result in higher values of η and $\kappa_{\max}\eta$, implying better resolution.
- Choose the value of fluid viscosity ν_f.
- The value of energy-dissipation rate ϵ can be predicted using the relation for Kolmogorov microscale:

$$\eta \equiv \left(\nu_f^3/\epsilon\right)^{1/4} \tag{2.21}$$

- Choose a value for non-dimensional forcing time-scale T_L^*. As an estimate, it is worth noting that Yeung and Pope [10] used $T_L^* = 0.15$ in their work. For the purpose of the present simulations, T_L^* is calculated based on the data provided in Overholt and Pope [30].

- The value of non-dimensional dissipation rate $\epsilon^* \equiv \sigma^2 T_L$ can be estimated using the empirical relation [28]:

$$\epsilon \equiv \frac{4\epsilon^* N_F}{1 + T_L^* (N_F)^{1/3} / \beta}. \tag{2.22}$$

  Eswaran and Pope demonstrate that the energy-dissipation (and thus the Kolmogorov microscale) is accurately predicted by this relation for $\beta = 0.8$.

- The forcing amplitude σ and forcing time-scale T_L are then obtained using the relations [28]:

$$\sigma = \frac{\epsilon^{*2/3}}{{T_L}^{*1/2}} \tag{2.23}$$

$$T_L = \frac{T_L^*}{\epsilon^{*1/3} \kappa_0^{2/3}}. \tag{2.24}$$

2.1.6 Parallelization

PANDORA has been written keeping in mind that it would be run on supercomputing clusters with parallel processing architecture. The physical space domain has been sliced in the x_2 direction, with each slice residing on a single processor. The Fourier space information has been parallelized in the x_3 direction.

2.2 Particle phase implementation

Particles are modeled in a Lagrangian sense in PANDORA . The position, $\mathbf{x}_p$, and velocity, $\mathbf{u}_p$, of a certain particle are given by

$$\frac{\mathrm{d}x_{p,i}}{\mathrm{d}t} = u_{p,i}, \tag{2.25}$$

$$\frac{\mathrm{d}u_{p,i}}{\mathrm{d}t} = \frac{u_{f,i}(\mathbf{x}_p) - u_{p,i}}{\tau_p} \left[1 + 0.15 {Re_p}^{0.687}\right] + g\delta_{i3} + f_{e,i}, \tag{2.26}$$

where $u_{f,i}(\mathbf{x}_p)$ is the fluid velocity evaluated at the particle location, τ_p is the particle response time, Re_p is the particle Reynolds number, g is the scalar acceleration due to gravity and $\mathbf{f}_e$ is the Coulomb force (per unit mass) acting on the particle. The particle response time τ_p is given by

$$\tau_p = \frac{d_p^2 \rho_p}{18 \nu_f \rho_f}, \tag{2.27}$$

where d_p is the particle diameter. The particle Reynolds number is given by

$$Re_p = \frac{|\mathbf{u}_f(\mathbf{x}_p) - \mathbf{u}_p| \, d_p}{\nu_f}. \tag{2.28}$$

Equation 2.26 only accounts for the viscous and pressure drag force and neglects the other forces on the particle present in the equation of particle motion derived by Maxey and Riley [31]. The neglected forces include the force due to fluid pressure gradient and viscous stresses, inertia force of added mass and viscous force due to unsteady relative acceleration (also referred to as Basset history force). Elghobashi and Truesdell [32] have shown that the neglected forces are at least one order of magnitude less than the viscous drag force and thus justifies the present approach. The assumptions associated with using equation 2.26 are summarised below:

- particle Reynolds number, $Re_p \leq 800$.
- particle diameter, d_p, has to be much less than the Kolmogorov length scale, η.
- particle density is much greater than the fluid density.
- the collisions between particles are neglected.

All simulations in the present work satisfy the above conditions.

The fluid velocity at particle location is evaluated using a third-order polynomial method [33]. The total number of particles in a simulation is maintained constant by making use of the periodic boundary conditions. Thus particles going out from one side of the domain re-appear on the other side.

2.2.1 Implementation of charges on particles

Presence of electric charge on the particles is taken into account by adding an electrical force, $\mathbf{f}_e$ to the right-hand side of equation 2.26,

$$f_{e,i} = \frac{q_p}{m_p} E_i(\mathbf{x}_p), \tag{2.29}$$

where q_p and m_p are the electric charge on the particle and mass of the particle respectively. $E_i(\mathbf{x}_p)$ is the electric field at the particle location. The electric field is interpolated to particle location using the same third-order polynomial method as used for interpolating fluid velocities to particle location. The electric field E_i over the domain is given by the divergence theorem

$$\frac{\partial E_i}{\partial x_i} = \frac{Q}{\epsilon_0}, \tag{2.30}$$

where Q is the local charge density (C/m^3)and ϵ_0 is the permittivity of free space (8.854×10^{-12} F/m). Note that the parameter that is varied in the simulations is the bulk charge density Q_v i.e. ratio of total charge in the domain to the domain volume V. The computational particles are treated as *parcels* as far as attaining the required charge density level is concerned. In order to attain the required bulk charge density, it is assumed that a single *computational* particle represents an ensemble of identical *real* particles. Say the number of *real* particles contained in a *computational* particle in N_s, then the local charge density Q is given by

$$Q = n\, N_s\, q_p, \tag{2.31}$$

where n is the local particle number density and q_p is the charge on single *real* particle.

In the simulations reported in this work, the charge on a single real particle q_p is limited to 80% of the Rayleigh limit Q_R, which represents the maximum charge that can be placed on a liquid droplet, given by

$$Q_R = \pi \sqrt{8\gamma\epsilon_0 d_p^3}, \tag{2.32}$$

where, γ is the surface tension coefficient. For all simulations in this study, surface tension coefficient of $\gamma = 0.05 N/m$ is used.

For PANDORA , being a pseudo-spectral code, it is convenient to evolve the electric field in spectral space. Using a Fourier series representation, the electric field is expressed as a truncated Fourier series

$$\mathbf{E}(\mathbf{x}) = \sum_{\kappa} \hat{\mathbf{E}}(\kappa)\, e^{j\kappa\cdot\mathbf{x}}. \tag{2.33}$$

The Fourier space equivalent of equation 2.30 is then given by -

$$\kappa\,.\,\hat{\mathbf{E}}(\kappa) = \hat{S}(\kappa), \tag{2.34}$$

where $\hat{S}(\kappa)$ is the Fourier mode (at wave-vector κ) of the term on RHS of equation 2.30.

The real space electric field is obtained from the Fourier space information by Fourier transform (equation 2.33). The FFTW library is used to transform the electric field from Fourier space to real space.

2.2.2 Implementation of two-way coupling

The incorporation of effect of particles on the turbulence is based on the particle-source-in-cell (PSIC) method of Crowe [34]. Details of the two-way coupling implementation can also be found in Boivin et al. [35]. The challenge for numerical modeling is to introduce appropriate modification terms in the fluid phase equations. The idea is to identify modification terms which would mimic the interphase momentum (consequently energy and dissipation) transfer as closely as possible.

The method adopted in the present work is described here. Incorporation of two-way coupling is reflected by the presence of the interphase coupling force $\mathbf{f}_c$ on RHS of equation 2.2. The particles and the fluid essentially communicate through the drag force. Thus the coupling force (per unit volume), $\mathbf{f}_c$, at any node is evaluated as the summation of contributions from the drag force, $\mathbf{f}_d$, from all particles contained in the Eulerian control volume ΔV surrounding that node

$$\mathbf{f}_c = \frac{1}{\Delta V} \sum_{\text{particles in}\,\Delta V} \mathbf{f}_d. \tag{2.35}$$

It should be noted that the particles are treated as *parcels* for the purpose of two-way coupled simulations. This essentially means that the particle volume is governed by the desired mass loading ϕ_p for a simulation and not the physical volume of the particle. The contribution from drag force on a particle is thus given by,

$$\mathbf{f}_d = -\rho_p \, v_p \, \mathbf{a}_p. \tag{2.36}$$

In equation 2.36, $\mathbf{a}_p$ is the particle acceleration due to drag force given by the first term on RHS of equation 2.26, ρ_p is particle density and v_p is the volume of a *parcel* given by

$$v_p = \frac{1}{N_p} \frac{\phi_p \rho_f}{\rho_p}, \tag{2.37}$$

where N_p is the number of particles used in the simulation.

2.3 Averaging conventions

The purpose of this section is to define the averaging conventions followed subsequently for all results reported in this work.

Eulerian volume average

Since all the work reported in this thesis deals with homogeneous configurations, the most commonly encountered Eulerian average is the spatial or volume average. This average is represented by angle brackets $\langle\rangle$ in the present work. Consider an instantaneous scalar quantity ϕ measured at N nodes in the domain. Then the instantaneous spatial average is defined as follows

$$\langle\phi\rangle = \frac{1}{N} \sum_{i=1}^{N} \phi_i. \tag{2.38}$$

Temporal average

The quantities averaged over time are represented by an overbar (e.g. $\bar{\phi}$). Consider a continuous scalar quantity f which has reached a stationary state. Then the temporal average starting at a arbitrary time t_i over a time period T is defined as follows

$$\bar{\phi} = \frac{1}{T} \int_{t_i}^{t_i+T} \phi \, \mathrm{d}t. \tag{2.39}$$

Lagrangian average

The Lagrangian properties averaged over a particle population are represented by a tilde (e.g. $\tilde{f}$). Consider a scalar quantity ϕ_i measured for particle i. The Lagrangian average over a population of N_p particles is then defined as follows

$$\tilde{\phi} = \frac{1}{N_p} \sum_{i=1}^{N_p} \phi_i. \tag{2.40}$$

2.4 Code validation

The different fluid phase quantities associated with turbulent flows are defined in section 2.4.1. The quantities associated with the particle phase are defined in section 2.4.2. Initially, simulations were performed without particles to obtain stationary fluid turbulence. Also a few simulations were performed to validate the forcing scheme and evaluate the required forcing parameters. Results from these validation runs are presented in section 2.4.3.

2.4.1 Fluid phase quantities

It is useful to introduce the different quantities typically used to characterise turbulent flows. In this study, we are primarily interested in the important length and time scales associated with turbulent flows. The other quantities of interest include the distribution of turbulent energy at differ-

ent scales. The correlation between instantaneous fluid velocities at two points has been used by Taylor [36] to define length scales associated with turbulence. The general two-point correlation is defined as

$$R_{ij}(\mathbf{r}) \equiv \langle u_i(\mathbf{x}+\mathbf{r})\, u_j(\mathbf{x}) \rangle . \tag{2.41}$$

The velocity spectrum tensor Φ_{ij} is the Fourier transform of the two-point velocity correlation R_{ij}. It is straightforward to show that

$$\Phi_{ij}(\kappa) = \hat{u}_i(\kappa)\hat{u}_j(-\kappa). \tag{2.42}$$

In the present work, we deal exclusively with isotropic turbulence and thus the quantity of interest is the distribution of energy at different scalar wavenumbers (or length-scales). The energy spectrum function $E(\kappa)$ provides information about the energy content at scalar wavenumber magnitude $|\kappa| = \kappa$. The energy spectrum function is calculated by binning the contribution from each mode, $\frac{1}{2}\Phi_{ii}(\kappa)$, to the bin containing κ. The bins are centered at integer values $\kappa = n\kappa_0$ with span $\kappa \pm \kappa_0/2$. To compensate for the nonuniform distribution of nodes in the spherical shells forming the wavenumber bands, the spectrum function calculated in this manner is smoothed by dividing it by the node density. For a bin centered on $n\kappa_0$ containing contributions from m modes, the node density $m(n)$ is given by

$$m(n) = \frac{m}{\frac{4}{3}\pi\left[(n+\frac{1}{2})^3 - (n-\frac{1}{2})^3\right]}. \tag{2.43}$$

The turbulent kinetic energy is obtained by integration of $E(\kappa)$ over all κ,

$$k = \sum_{\kappa} E(\kappa). \tag{2.44}$$

The dissipation rate is given by

$$\epsilon = \sum_{\kappa} 2\nu_f \kappa^2 E(\kappa). \tag{2.45}$$

The RMS turbulence velocity (or turbulence intensity), u', is given by

$$u' = \sqrt{\frac{2\,k}{3}}. \tag{2.46}$$

For isotropic turbulence, only the scalar separation r needs to be considered and R_{ij} can be expressed in terms of two scalar functions - the longitudinal autocorrelation function, $f(r)$, and transverse autocorrelation function, $t(r)$,

$$f(r) = \frac{\langle u_1(\mathbf{x}+e_1 r)\, u_1(\mathbf{x})\rangle}{\langle u_1^2\rangle}, \tag{2.47}$$

$$t(r) = \frac{\langle u_2(\mathbf{x}+e_1 r)\, u_2(\mathbf{x})\rangle}{\langle u_2^2\rangle}. \tag{2.48}$$

The longitudinal integral length scale, L_{11}, which is characteristic of the size of large eddies, is defined as

$$L_{11} \equiv \int_0^\infty f(r)\mathrm{d}r. \tag{2.49}$$

In isotropic turbulence, L_{11} is given by

$$L_{11} = \frac{\pi}{2u'^2}\sum_\kappa \frac{E(\kappa)}{\kappa}. \tag{2.50}$$

The time-scale associated with large eddies is the eddy turnover time, T_E, defined as

$$T_E \equiv \frac{L_{11}}{u'}. \tag{2.51}$$

Following Kolmogorov's hypotheses, the length scale of the smallest eddies is given by

$$\eta \equiv \frac{\nu_f^{3/4}}{\epsilon^{1/4}}, \tag{2.52}$$

where ν_f is the fluid kinematic viscosity and ϵ is the dissipation rate of the turbulent flow under consideration. The corresponding time scale of the smallest eddies is defined as

$$\tau_k \equiv \frac{\nu_f^{1/2}}{\epsilon^{1/2}}. \tag{2.53}$$

The length and time scales, η and τ_k are referred to as the Kolmogorov length and time scale respectively. Taylor [36] defined an intermediate length scale between η and L_{11}. The transverse Taylor microscale, λ_t is defined as

$$\lambda_t = \left[-\frac{1}{2}t''(0)\right]^{-1/2}, \tag{2.54}$$

where $t''(0) = (\partial^2 t/\partial r^2)_{r=0}$ is the second derivative of the transverse autocorrelation function, $t(r)$, at the origin. In isotropic turbulence,

$$\lambda_t^2 = \frac{15\nu_f u'^2}{\epsilon}. \tag{2.55}$$

The Taylor Reynolds number,

$$Re_\lambda \equiv \frac{u'\lambda_t}{\nu_f}, \tag{2.56}$$

is one of the most important quantities used to characterise turbulent flows.

The dissipation skewness, defined by equation 2.57, provides an additional measure of small-scale accuracy.

$$S_\epsilon = \frac{1}{35}\left(\frac{15\nu}{\epsilon}\right)^{\frac{3}{2}} \int_0^{\kappa_{max}} 4\nu\kappa^4 E(\kappa)\,\mathrm{d}\kappa. \tag{2.57}$$

2.4.2 Particle phase quantities

For a mono-dispersed particle phase with particle density ρ_p, particle diameter d_p and total number N_p, the additional non-dimensional parameters are the volume loading α_p, non-dimensional size d_p/η and particle Stokes number St_k. The definition of Stokes number poses the need to determine a suitable fluid timescale which influences particle dispersion. Given the multi-scale nature of turbulence, the choice of appropriate fluid timescale is by no means obvious. As will be discussed later, it has been consistently observed [4, 13, 37] that PC is most pronounced when the particle response time is nearly the same as the Kolmogorov time scale of the fluid turbulence. Thus the Kolmogorov time scale is the appropriate time scale for defining the Stokes number in the context of the present work. The Stokes number in the present study is defined as

$$St_k = \frac{\tau_p}{\tau_k}, \tag{2.58}$$

where τ_p is the particle response time and τ_k is the Kolmogorov timescale.

In the present study, the targeted mean Stokes number is attained by changing the particle di-

ameter. It should be noted that though the fluid turbulence is statistically stationary, there are instantaneous departures of the Kolmogorov timescale from its mean value. Consequently, the instantaneous Stokes number can be different from the mean value.

The gravitational force is characterised by the gravitational settling velocity, defined as follows,

$$v_g = \tau_p g \,, \tag{2.59}$$

where τ_p is the particle response time and g is the acceleration due to gravity. The direction of g is in the negative x_3 (Z-direction) for all simulations reported in this study. The gravitational settling velocity represents the terminal velocity attained by an inertial particle in still fluid. The corresponding non-dimensional gravitational settling velocity is defined as,

$$v_g^* = \frac{v_g}{u'} \,, \tag{2.60}$$

where u' is the RMS turbulence velocity.

$\langle n \rangle$ is the mean particle number density in the domain, defined as

$$\langle n \rangle = \frac{N_p}{V}. \tag{2.61}$$

2.4.3 Validation runs

Initially simulations were performed only for fluid (without particles) to attain statistically stationary turbulence. These simulations were started from a prescribed energy spectrum. The velocity field and the instantaneous forcing parameters for each Reynolds number were then stored in separate restart files for the subsequent study of particle accumulation. These restart files, generated at the end of the initial runs, were then used to start all particle simulations for that Reynolds

number. Thus the statistically steady fluid turbulence attained in these simulations is used as the starting point for all particle runs described in later chapters. This ensured that all simulations for a given Reynolds number have the same underlying fluid realisation and thus the effect of changing particle properties could be systematically investigated. Particles were initialized at random positions within the computational domain and released with initial velocity equal to the local fluid velocity. It was verified that the same results were obtained even if the particles were initially uniformly distributed. The comparison data has been presented in section 3.4. The results of these initial fluid simulations are described here.

The procedure described in section 2.1.5 has been employed to estimate forcing parameters for grids ranging from 32^3 to 256^3. The maximum wavenumber in one direction is limited to $N/3$ (nearest lower integer value) due to the truncation technique employed to remove the *aliasing* errors. The maximum resolved wavenumber in the (3-D) simulations is thus $\kappa_{\max} = N/\sqrt{3}$. Arbitrary choices for the forcing parameters are made based on a certain target Reynolds number for each grid resolution. Following the work of Overholt and Pope [30], $v_f = 0.025$ for all simulations in the present work. The non-dimensional spatial resolution parameter $\kappa_{max}\eta$ is chosen to be greater than 1.5 for all grid resolutions, which is adequate for higher-order quantities such as dissipation [10].

With the aforementioned choices, the forcing parameters and the corresponding expected flow-characterizing parameters are listed in table 2.1 along with those used in Yeung and Pope [10] (titled YP64 and YP128). The Reynolds numbers mentioned in table 2.1 are the *a priori* estimates except those for YP64 and YP128, which are the time-averaged output values. Similarly, the values of the non-dimensional quantity $\kappa_{\max}\eta$ mentioned in table 2.1 are the *a priori* estimates while those for YP64 and YP128 simulations are the time-averaged output values.

Eulerian statistics were collected at every time step during the simulations. The Eulerian statistics were volume-averaged for all nodes in the computational domain. All statistics were written to a file at each time step and subsequently time averaged at the end of the simulations. An initial period of about 5 to 10 eddy turnover times was discarded before calculating the stationary statistics.

	N^3	32^3	64^3	128^3	256^3	YP64	YP128
Forcing radius	κ_F/κ_0	$2\sqrt{2}$	$2\sqrt{2}$	$2\sqrt{2}$	$2\sqrt{2}$	$2\sqrt{2}$	$2\sqrt{2}$
Maximum wavenumber	$\kappa_{\max}/\kappa_0$	$N/\sqrt{3}$	$N/\sqrt{3}$	$N/\sqrt{3}$	$N/\sqrt{3}$	$\sqrt{2}N/3$	$\sqrt{2}N/3$
Number of forced modes	N_F	92	92	92	92	92	92
Fluid viscosity, m^2s^{-1}	ν_f	0.025	0.025	0.025	0.025	0.025	0.025
Forcing amplitude, ms^{-2}	σ	0.03743	0.212	2.0	12.0	0.1432	0.1432
Forcing time-scale, s	T_L	0.92807	0.321	0.069	0.04	0.6369	0.6369
Non-dimensional dissipation	ϵ^*	0.0013	0.014	0.276	5.76	0.01306	0.01306
Non-dimensional forcing timescale	T_L^*	0.101	0.075	0.045	0.072	0.15	0.15
Non-dimensional resolution	$\kappa_{max}\eta$	1.57	1.70	1.55	1.48	1.50	2.96
Taylor Reynolds number	Re_λ	24	41	78	144	38	38

Table 2.1: Forcing parameters used in present runs and those used by Yeung and Pope [10] (YP64-YP128).

Figures 2.1, 2.2, 2.3 and 2.4 show the evolution of the turbulent kinetic energy and dissipation once stationarity has been achieved. Figure 2.5 shows the evolution of dissipation skewness for the different grid resolutions.

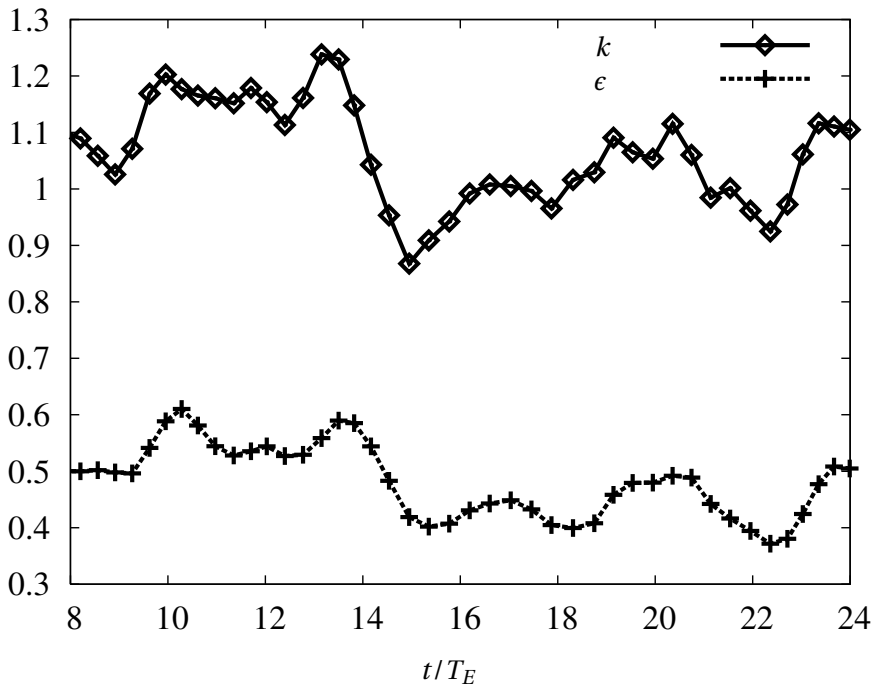

Figure 2.1: Evolution of the turbulence kinetic energy, k and dissipation rate, ϵ for the 32^3 simulation. The time is normalised by the average eddy-turnover time from the steady region.

For each grid resolution, the statistically stationary values of different turbulence quantities are listed in table 2.2. It should be noted that the obtained Reynolds numbers are in good agreement with the target Reynolds numbers listed in table 2.1. The non-dimensional spatial resolution

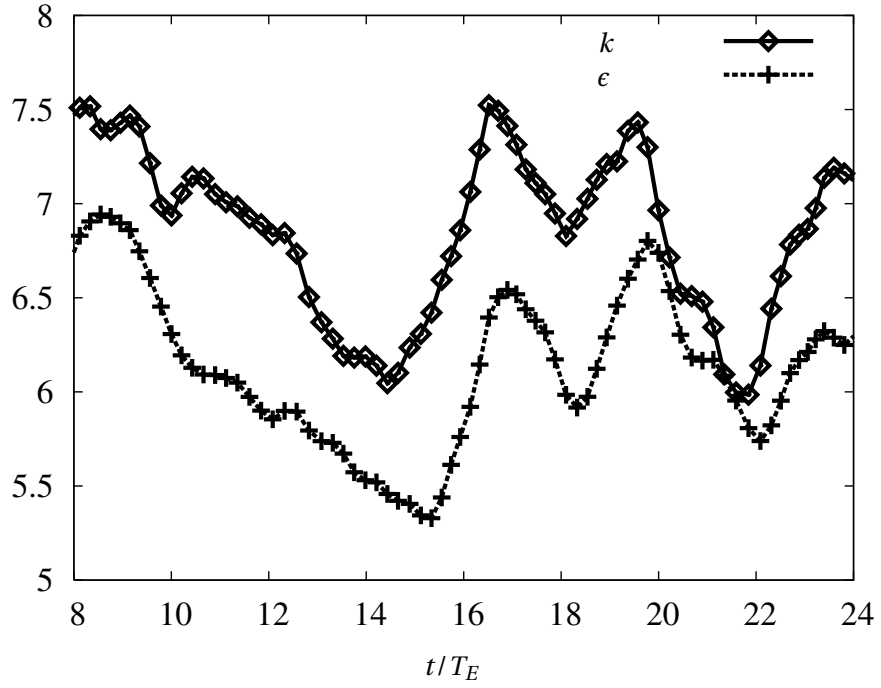

Figure 2.2: Evolution of the turbulence kinetic energy, k and dissipation rate, ϵ for the 64^3 simulation. The time is normalised by the average eddy-turnover time from the steady region.

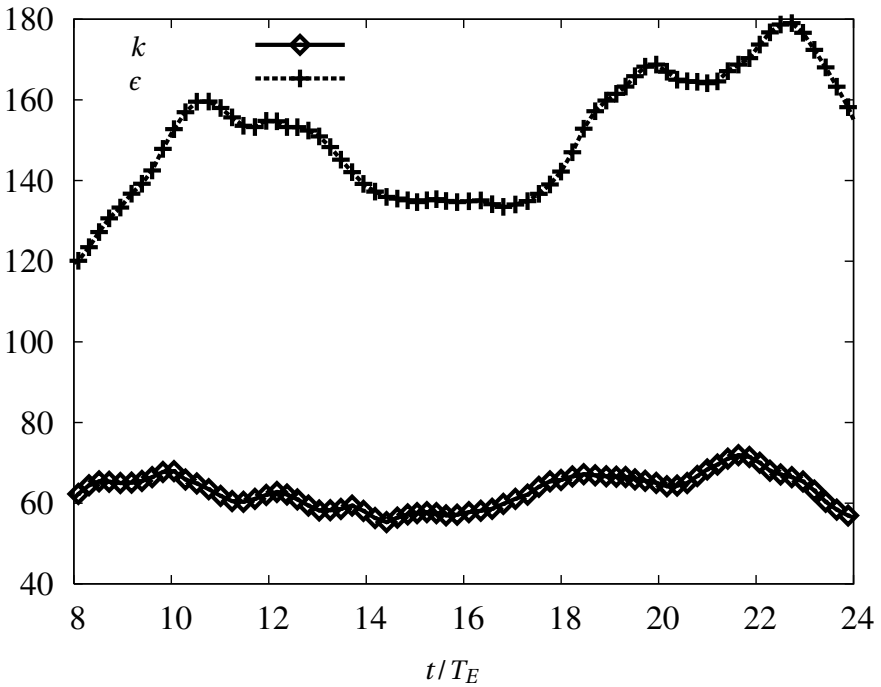

Figure 2.3: Evolution of the turbulence kinetic energy, k and dissipation rate, ϵ for the 128^3 simulation. The time is normalised by the average eddy-turnover time from the steady region.

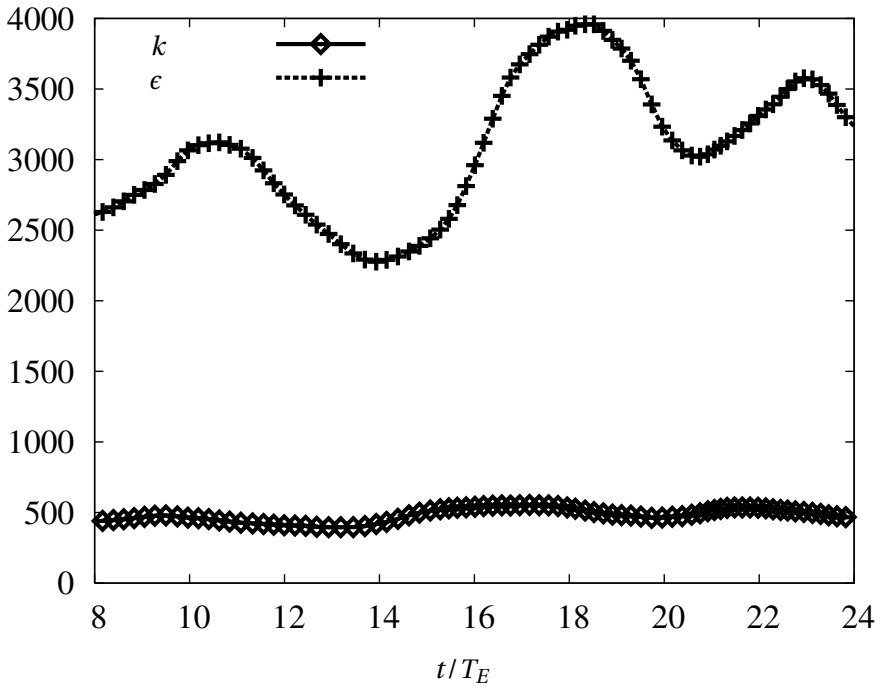

Figure 2.4: Evolution of the turbulence kinetic energy, k and dissipation rate, ϵ for the 256^3 simulation. The time is normalised by the average eddy-turnover time from the steady region.

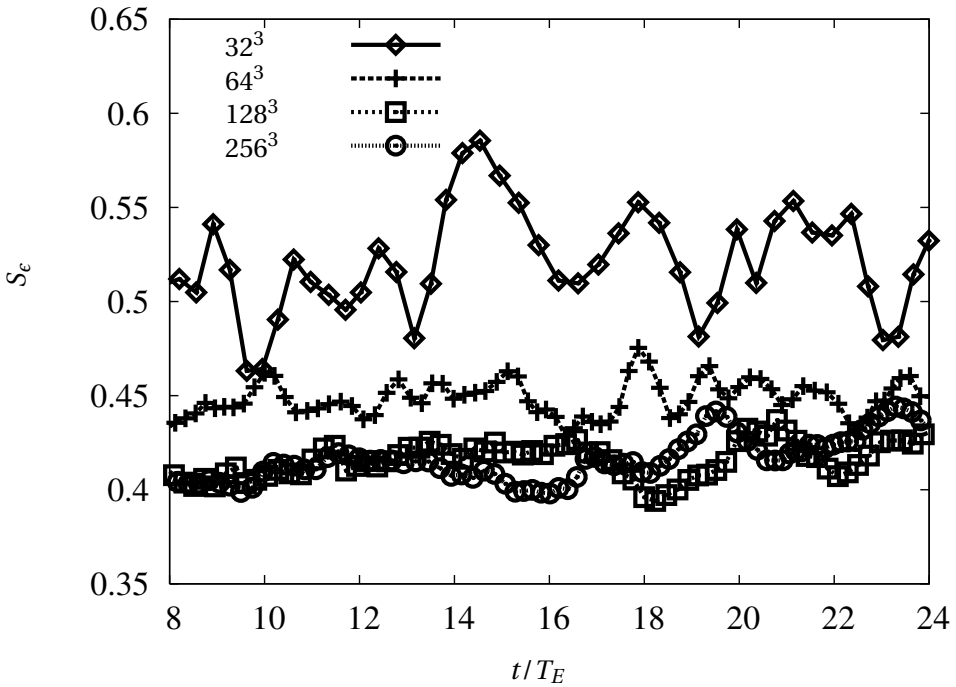

Figure 2.5: Evolution of the dissipation skewness, S_ϵ for different grid resolutions. The time is normalised by the average eddy-turnover time from the steady region.

parameter $\kappa_{max}\eta$ as measured during the validation runs is greater than 1.29 for all simulations, which is an indicator of good resolution. The values of S_ϵ obtained from the simulations are close to 0.5, which is the asymptotic value for this parameter at high Reynolds numbers [38].

	N^3	32^3	64^3	128^3	256^3
Non-dimensional resolution	$\kappa_{max}\eta$	1.404	1.293	1.330	1.330
Kolmogorov length scale	η	0.076	0.040	0.018	0.009
Kolmogorov time scale	τ_k	0.230	0.063	0.013	0.003
Longitudinal integral length scale	L_{11}	1.224	1.035	0.857	0.811
Transverse Taylor microscale	λ_t	0.734	0.522	0.324	0.196
Eddy turnover time	T_E	1.486	0.482	0.138	0.047
Turbulence intensity	u'	0.829	2.157	6.252	17.384
Turbulent kinetic energy	k	1.031	6.978	58.63	453.3
Dissipation rate	ϵ	0.482	6.415	141.7	2968.3
Taylor Reynolds number	Re_λ	24.2	45.0	80.6	136.0
Dissipation skewness	S_ϵ	0.521	0.446	0.417	0.414

Table 2.2: Flow characteristics for 32^3, 64^3, 128^3 and 256^3 domains. All quantities are time-averaged quantities and the overbar is omitted for simplicity. Units of all quantities mentioned in the nomenclature.

The time-step size Δt is evaluated at every time-step based on the CFL criterion specified in section 2.1.3. The average time-step for the different runs is specified in table 2.3. It should be noted that the average time-step is much smaller than the smallest turbulence time-scale, τ_k, for all simulations.

Re_λ	$\Delta t / \tau_k$
24.2	0.12
45.0	0.08
80.6	0.06
136.0	0.04

Table 2.3: Average time-steps used for simulations at different Reynolds numbers.

In addition to the quantities introduced in section 2.4.1, certain additional quantities are described here to further probe the structure of the simulated turbulent flows.

The second-order velocity structure function, D_{ij} is the covariance of the difference in velocity between two points $\mathbf{x}+\mathbf{r}$ and $\mathbf{x}$,

$$D_{ij}(\mathbf{r},\mathbf{x}) = \langle [u_i(\mathbf{x}+\mathbf{r}) - u_i(\mathbf{x})]\,[u_j(\mathbf{x}+\mathbf{r}) - u_j(\mathbf{x})] \rangle. \tag{2.62}$$

In isotropic turbulence, D_{ij} can be written as

$$D_{ij}(\mathbf{r}) = D_{NN}(r)\delta_{ij} + [D_{LL}(r) - D_{NN}(r)]\frac{r_i r_j}{r^2}, \tag{2.63}$$

where D_{LL} and D_{NN} are the scalar longitudinal and transverse structure functions respectively. In isotropic turbulence, D_{ij} is determined by the single scalar function, D_{LL}. The transverse structure function, D_{NN} is uniquely determined by D_{LL}. For purpose of validation, correlations have been calculated in the x-direction, thus,

$$D_{LL} = D_{11}, \quad D_{NN} = D_{22} = D_{33}. \tag{2.64}$$

According to Kolmogorov's first similarity hypothesis, for locally isotropic turbulence (in dissipation range length-scales), D_{ij} is uniquely determined by ϵ and ν. Thus according to this hypothesis, there is a universal, non-dimensional function D^*_{LL} such that,

$$D^*_{LL}(r) = \epsilon^{-2/3} r^{-2/3} D_{LL}(r). \tag{2.65}$$

According to Kolmogorov's second similarity hypothesis, in the inertial subrange, D_{LL} is independent of ν_f, which, using dimensional analysis, implies,

$$D^*_{LL}(r) = \epsilon^{-2/3} r^{-2/3} D_{LL}(r) = C(\text{constant}), \tag{2.66}$$

$$D^*_{NN}(r) = \epsilon^{-2/3} r^{-2/3} D_{NN}(r) = \frac{4}{3} C(\text{constant}). \tag{2.67}$$

where C is a universal constant.

Figures 2.6 and 2.7 show the structure functions calculated during validation runs using PANDORA . A plateau region in the D^*_{LL} and D^*_{NN} curves is representative of the inertial subrange. It is seen that for the 32^3 and 64^3 runs, there is no distinct inertial subrange. At the highest

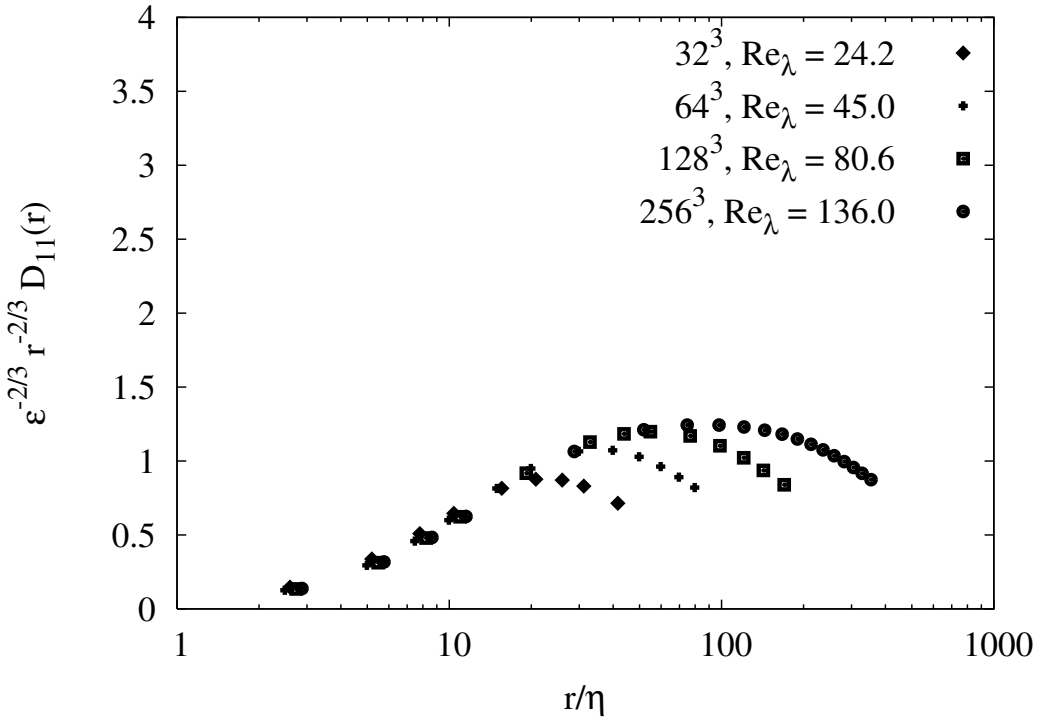

Figure 2.6: Second-order longitudinal velocity structure functions at different Taylor Reynolds numbers.

Reynolds number simulated in the present study, a distinct inertial subrange in seen between roughly $30\eta - 100\eta$.

2.4.4 Concluding remarks

The primary objective of the validation runs has been to demonstrate that the code is capable of sustaining stationary fluid turbulence. This has been achieved using the forcing scheme proposed by Eswaran and Pope [28]. It has been observed that the flow charaterising statistics reach a stationary state thus validating the forcing scheme and the procedure for evaluating the forcing parameters. Moreover the stationary Reynolds numbers obtained from the simulations are in excellent agreement with those predicted *a priori*. The value of the dissipation skewness is near 0.5 for all the simulations indicating that the small scales of the flow are uninfluenced by the forcing scheme. This value is consistent with both numerical [38] and experimental results published in literature. Finally, it is interesting to note that at high Reynolds numbers, there are atleast two decades of length scales separating the Kolmogorov and integral length scales. The phenomenon

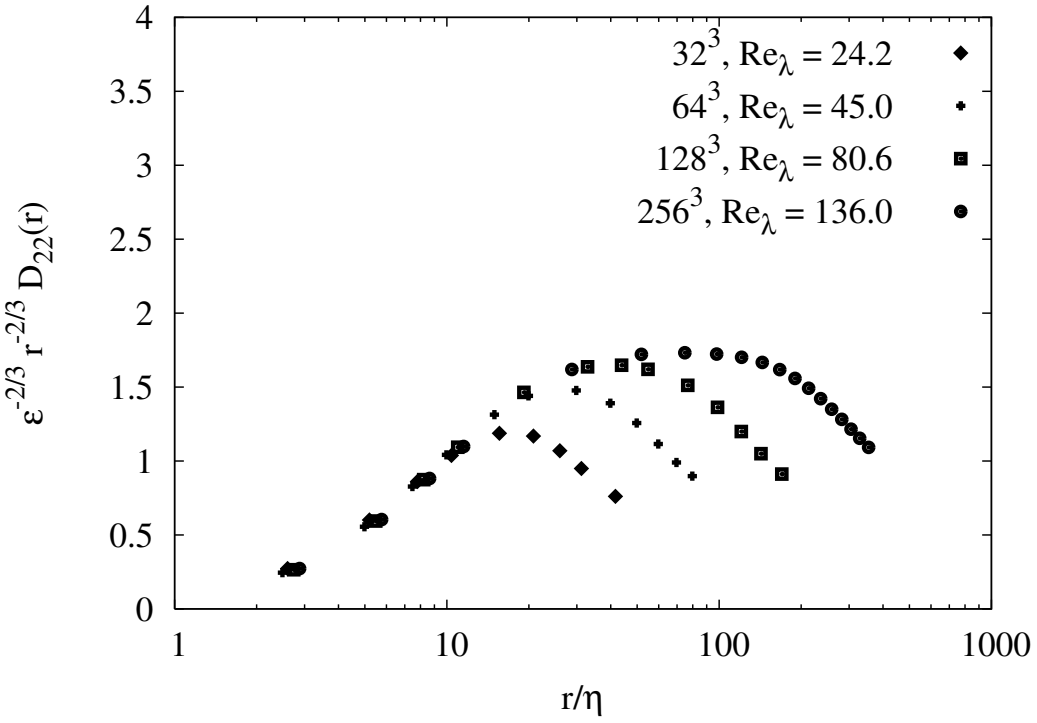

Figure 2.7: Second-order transverse velocity structure functions at different Taylor Reynolds numbers.

of particle clustering at different length scales is investigated in subsequent chapters.

Chapter 3

Preferential accumulation of particles in one-way coupled scenario

It has been observed in present and previous studies that under certain conditions, an initially uniform distribution of particles organizes itself into a highly segregated configuration. This accumulation of particles can be explained in different ways. A survey of our current understanding of different mechanisms of clustering is carried out. A simple way of explaining clustering is to attribute it to the centrifugal effect of the eddies resulting in collection of particles along their edges. Instantaneous preferentially accumulated configurations are attributed to the deviation of particle trajectories from the fluid pathlines leading to lower concentration of particles in the vortex cores and correspondingly larger concentration in the region between eddies. It is important to note that in this interpretation there would be two length scales associated with clustering - the size of the structures causing the clustering and the size of the particle clusters themselves. In the present work, different measures have been employed to estimate these length scales. Of particular interest to the work presented in this chapter is the dependence of these length scales on the fluid Reynolds number, particle response time and the strength of gravitational body force on the particles. The predominant role of Kolmogorov scale eddies in causing accumulation, also observed in previous work in literature, is also demonstrated in the present work. The Reynolds number scaling of preferential accumulation has been a matter of debate in the literature. Wang et al. [39]

reported a linear scaling of accumulation with Reynolds number while Collins and Keswani [40] suggested that clustering is not enhanced at large Reynolds numbers. It should be noted that the Reynolds numbers in both these DNS studies are very limited. The maximum Taylor Reynolds number in the study by Wang et al. [39] is only 75 while that in study by Collins and Keswani [40] is 152. To extrapolate the findings of these studies to practical problems of interest, which inevitably involve much higher Reynolds numbers (e.g. rain initiation in cumulus clouds [11]), is not straightforward and continues to be an area of active research. In the present work, DNS of HIT is performed over a range of fluid Reynolds numbers and particle Stokes numbers to investigate accumulation behavior. The range of Stokes numbers investigated in the present work is broader than in previous studies. The role of gravitational settling in inertial clustering is also explored in this chapter. Introducing the gravitational body force enables us to perform a parametric study of a situation where the particles tend to jump from one eddy to another at an enhanced rate. It is well known that in the presence of gravity, particles tend to disperse less in the lateral directions due to the so-called *crossing trajectories* effect. The sensitivity of the different measures of accumulation to strength of gravitational force is investigated.

3.1 Aims and Objectives

In this chapter, a systematic investigation of accumulation for different fluid and particle parameters is carried out. The effect of a gravitational settling force is also investigated. The fluid turbulence is characterised by its Taylor Reynolds number, Re_λ (introduced in section 2.4.1). The particle inertia and settling velocity are characterised by the non-dimensional parameters, St_k and v_g^* (both introduced in section 2.4.2). In the work presented in this chapter, we use different measures for quantifying preferential concentration and probe their dependence on Re_λ, St_k and v_g^*. The different measures used for quantifying accumulation are outlined in section 3.2. The scaling of bin-size dependent measures like D with Reynolds number has not been addressed in previous studies and the present study fills this gap. The length scale of the particle clusters is estimated in this study by using a binning technique while the spacing between clusters is estimated from the Eulerian correlation of particle number density. Other measures derived from fractal geometry are also invoked. The sensitivity of the indicators of accumulation to each of the above stated

parameters is systematically investigated and reported here. The results presented in this chapter are limited to one-way coupling, neglecting the influence of particles on the fluid turbulence. The one-way coupling assumption is justified by the dilute nature of the suspension.

3.2 Indicators of preferential accumulation

Before proceeding to discuss the literature on accumulation of particles, it is useful to define the indicators of accumulation used in the literature. The different measures of accumulation are introduced in this section. It is hoped that this will make it easier for the reader to follow the subsequent discussion. The averaging conventions used here have been defined in section 2.3. Preferential accumulation essentially refers to the tendency of particles to remain in particular regions of the flow. Thus it is desirable to capture the correlation between regions of above/below average particle number densities and underlying fluid properties in these regions. The correlation between deviation of local enstrophy, e', and deviation of local particle number density, n', is used to demonstrate preferential accumulation in low-vorticity areas. For the purpose of calculating $\langle n'e' \rangle$, the domain is subdivided into small cubes or bins (demonstrated in two dimensions in figure 3.1). The measure is calculated as an Eulerian average over the spatial domain. The mean enstrophy in the domain is defined as

$$\langle e \rangle = \frac{1}{N_b} \sum_{j=1}^{N_b} \left(\omega_1^2 + \omega_2^2 + \omega_3^2 \right)_j . \tag{3.1}$$

The number of bins used for calculating $\langle n'e' \rangle$ is the same as the number of nodes for that simulation, N^3. For each bin, n' and e' are defined as follows

$$n' = \frac{n - \langle n \rangle}{\langle n \rangle} , \tag{3.2}$$

$$e' = \frac{e - \langle e \rangle}{\langle e \rangle} , \tag{3.3}$$

where n and e are the volume-averaged particle number density and enstrophy within the bin respectively. For n_p particles in a bin of volume, $V_b = h^3$, the local particle number density in that

bin is given by

$$n = \frac{n_p}{V_b}. \tag{3.4}$$

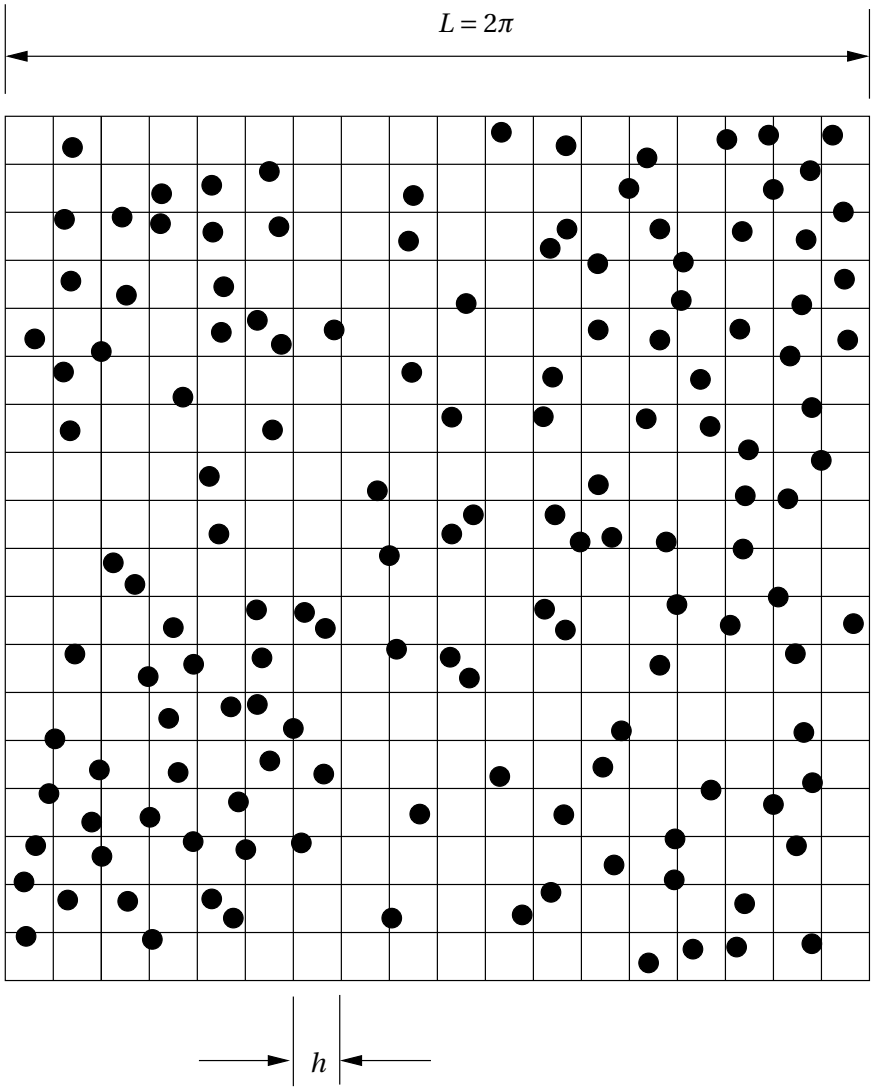

Figure 3.1: Schematic representation of *binning* process for calculating $\langle n'e' \rangle$ and D measures.

Several other measures are based on binning of particles. Here the procedure to calculate the D measure[3, 4] is described. Similar to the $\langle n'e' \rangle$ measure, the domain is divided into small uniform bins of side h. The next step is to count the number of bins with a certain number of particles, c (e.g. in figure 3.1, c = 0,1,2). The probability of finding bins with c particles, $P_m(c)$, is then given by,

$$P_m(c) = \frac{N_b(c)}{N_b}\,, \tag{3.5}$$

where $N_b(c)$ is the number of bins with c particles and N_b is the total number of bins. For a uniform distribution of N_p particles, the number of particles in each bin would be $\lambda = N_p/N_b$. The departure of the measured particle distribution from an uniform distribution can be quantified by the variance of the particle distribution, defined as,

$$\sigma_m^2 = \sum_{c=0}^{N_p} (c-\lambda)^2 P_m(c). \tag{3.6}$$

For a random distribution of particles, the probability of finding c particles in a bin is a random variable that is Poisson distributed. The Poisson distribution or probability of finding bins with c particles for randomly distributed particles, $P_p(c)$is defined as,

$$P_p(c) = \frac{e^{-\lambda}\,\lambda^c}{c!}. \tag{3.7}$$

The corresponding variance of N_p randomly distributed particles is given by

$$\sigma_p^2 = \sum_{c=0}^{N_p} (c-\lambda)^2 P_p(c). \tag{3.8}$$

The D measure, used by Fessler et al. [3] to characterise non-homogeneous distribution of particles in their channel-flow experiments, is defined as

$$D = \frac{\sigma_m - \sigma_p}{\lambda}. \tag{3.9}$$

Another bin-size sensitive global measure of accumulation is the D_c measure [13], defined as follows

$$D_c = \sum_{c=0}^{N_p} \left(P_m(c) - P_p(c)\right)^2. \tag{3.10}$$

Both D and D_c measures essentially convey the same information about particle distribution and therefore only the D measure is reported in the present study. The D measure characterises the deviation of the observed particle distribution from a perfectly random distribution. For a random distribution of particles, the D measure would be identically zero. Also it is easily seen from the definition of D that bins containing mean number of particles ($c = \lambda$), do not add value to the D measure. Preferential accumulation of particles is characterised by large positive values of D. This is attributed to the presence of bins containing much more particles than the mean value as well

as the presence of a large number of voids. It should be noted that the D measure for a uniform distribution of particles (i.e. equal particles in all bins) is negative since $\sigma_m = 0$. The D measure being a function of the bin-size, h, the most appropriate way to report the D measure is to show its variation with h and note its peak value along with the bin-size at which the peak occurs. In the context of the present work, the peak bin-size non-dimensionalised by the Kolmogorov length scale provides insight into particle accumulation phenomenon.

The particle-particle spacing in clusters can be estimated using the radial distribution function (RDF) [41, 42]. The RDF, $g(r)$, is calculated by binning particle pairs according to their separation distances and then evaluating the RDF over annular shells of thickness Δr. The RDF for a distribution of N_p particles is obtained by calculating

$$g(r) = \frac{P_r/\Delta V_r}{P/V}\,, \tag{3.11}$$

where P_r is the number of particle pairs separated by a distance $r \pm \Delta r/2$, ΔV_r is the volume of the shell of thickness Δr located at radius r. $P = N_p(N_p-1)/2$ is the total number of pairs in the simulation and $V = L^3$ is the total volume of the domain. The RDF has been used by researchers to estimate the effect of clustering on frequency of particle collisions [41, 42]. The RDF essentially represents the probability of finding particle pairs with a radial separation distance r. For a uniform particle distribution $g(r)$ is identically unity. Values of RDF exceeding unity are indicators of accumulation at that length scale r. Keeping in mind the importance of the Kolmogorov length scale in the context of accumulation, the length scale r in non-dimensionalised by the Kolmogorov length scale, η, while reporting results for the RDF. The size of particle clusters can be estimated by looking at the length scale where the RDF becomes less than unity. Another equivalent measure used by researchers [40, 43] is the pair correlation function, defined as $h(r) \equiv g(r) - 1$.

The correlation dimension, D_2, is a measure derived from the RDF which enables characterisation of particle distribution by a single parameter irrespective of the scale at which accumulation occurs. This measure, introduced by Grassberger and Procaccia [44], is part of a spectrum of generalised dimensions used to characterise multi-fractal sets. The correlation dimension is defined as

$$D_2 = \lim_{r\to 0}\left(\frac{1}{\log r}\right)\log\sum_{r}^{r+\mathrm{d}r} p_r^2\,, \tag{3.12}$$

where r is a variable length scale and p_r is the probability that the separation distance between two particles is less than r [45]. D_2 is representative of the probability of finding two particles at a distance less than a given r: $P_r \sim r^{D_2}$ [5, 7]. If the particles are uniformly distributed, the number of particles within a sphere of radius r centered on a base particle, $N(r)$, will scale with the volume of the sphere (r^3). The correlation dimension is then defined as the slope of $\log(N(r))$ vs $\log(r)$. In the present implementation, D_2 is computed by binning all the particle pairs, P_r, according to their separation distance r and calculating the slope of the curve $\log(P_r)$ versus $\log(r)$ over a range of r where a linear dependence exists. For an uniform distribution, D_2 equals the space dimension (3 for 3-D). Deviation of D_2 from the space dimension is an indicator of preferential accumulation. Another measure used in the present work is the clustering length scale, l_n, defined as

$$l_n = \frac{\pi}{2\langle n \rangle^2} \sum_{\kappa} \frac{N(\kappa)}{\kappa} d\kappa \,, \tag{3.13}$$

$$N(\kappa) = \frac{\hat{n}(\kappa)\,\hat{n}^c(\kappa)}{2}, \tag{3.14}$$

where $\hat{n}(\kappa)$ is the Fourier transform of the number density distribution field and $\hat{n}^c(\kappa)$ is its complex conjugate. The summation is over all the resolved wavenumbers in the simulation. $N(\kappa)$ is defined along the lines of the fluid kinetic energy, $E(\kappa)$, to obtain a length scale consistent with fluid integral length scale. This length scale provides a convenient measure of the extent of the region over which the particle number density field is correlated.

A detailed study of the above indicators helps to estimate the two length scales associated with clustering of particles. The measures involving *binning* provide a way to estimate the size of particle clusters. The spacing between clusters is estimated from the extent of correlation of the particle number density field. A survey of the findings of previous studies in this context is presented next in section 3.3.

3.3 Background

Preferential accumulation of particles in turbulent flow has been observed in a multitude of situations like free shear flows[46], wall-bounded flows[47] and homogeneous flows[13, 43, 48, 49].

The earliest speculation of the tendency of inertial particles to accumulate in regions of low vorticity was proposed by Maxey [14]. In a thorough review of preferential accumulation, Eaton and Fessler [50] examined accumulation in different flows including free shear flows, wall bounded flows, homogeneous flows, complex jets and separated flows for very small volume loadings such that the effect of particle-particle collisions could be neglected. They highlighted the role of coherent vortical structures, which are observed in all the above mentioned flow configurations, as the basic mechanism that causes preferential accumulation. Particles tend to be thrown out of vortex cores and get accumulated in the convergence region between eddies. The instantaneous eddy structures thus govern the particle concentration distribution. It should be borne in mind that the turbulent eddies persist only for a finite time. Eaton and Fessler [50] note that preferential accumulation is observed only for particles with a certain response time. Numerous experiments and simulations have confirmed that this particular response time is nearly equal to the time-scale of the dominant turbulent eddies for the flow under consideration. Particles with a smaller response time tend to follow the fluid pathlines and thus continue to be distributed randomly. On the other hand, particles with very high response time are sluggish and hence do not significantly respond to the eddy motions during the lifetime of the eddy. The non-dimensional parameter characterising this behavior is the Stokes number, defined as the particle response time non-dimensionalised using an appropriate turbulence time-scale.

At low Reynolds numbers, the dominant eddies in the fluid turbulence are the Kolmogorov scale eddies [51]. Numerous low Reynolds number studies have found out that accumulation is most pronounced for Stokes number based on the Kolmogorov time-scale , $St_k \approx 1.0$. In their DNS, Squires and Eaton [37] found that particle distribution is most inhomogeneous for $St_k = 0.65$. The Taylor Reynolds number in their simulation was $Re_\lambda = 38.7$ and trajectories of 10^6 particles were followed. They found that particles tend to accumulate in regions of low vorticity and high strain. The DNS studies of Wang and Maxey [13] at $Re_\lambda = 31$ also showed that accumulation is maximum for $St_k \approx 1.0$ particles, though the focus of their study was on the settling velocities of particles under the influence of gravity. Hogan and Cuzzi [6] studied particle accumulation using DNS at three Taylor Reynolds numbers - $Re_\lambda = 40, 80, 140$ and St_k ranging from 0.2 to 6. They employed the D_c and D_2 measures (described in section 3.2) and found that accumulation is maximum at $St_k \approx 1.0$. Sundaram and Collins [41] did a systematic analysis to gather collision statistics across a

wide range of Stokes numbers at $Re_\lambda = 54.2$. The Stokes numbers studied in their work vary from 1.0 to 8.0 based on the Kolmogorov time-scale. Their results confirmed the qualitative picture of depletion of particles from high vorticity areas and corresponding accumulation in low vorticity areas. Quantitatively they observed that the D_c measure and the RDF at contact, $g(d_p)$, show the same trend with Stokes number as the study by Squires and Eaton [37]. It is observed though that the peak in $g(d_p)$ occurs at slightly lower Stokes number ($St_k = 0.4$) than the peak in D_c, which occurs at $St_k = 1.0$. Wang et al. [39] observe a peak in RDF at contact at $St_k \approx 1.0$ in their DNS studies. The peak in the studies of Sundaram and Collins [41] and Wang et al. [39] occur at different values of St_k owing to the significant uncertainty and artificial repeated collisions in the work of Sundaram and Collins [41] [52]. Fessler et al. [3] investigated particle concentration at the centerline of a turbulent channel flow, where the flow is close to homogeneous conditions, and found evidence of particle accumulation. The Taylor Reynolds number of their experiment was nearly 150 and they investigated behavior of particles with Stokes numbers ranging from 0.74 to 41. For the Reynolds number studied in their experiment, they found that accumulation is maximum for $St_k \approx 2.0$ using the D measure. They also observed that the spacing between particle clusters was much larger than the size of the clusters themselves. Aliseda et al. [49] performed wind-tunnel experiments at $Re_\lambda \approx 75$ and estimated the size of particle clusters to be around 10η. At the limit of small Stokes numbers, Chun et al. [53] developed a theory which predicts exponential growth of the RDF even at sub-Kolmogorov scales. The model developed by Chun et al. [53] suggests that the steady state RDF is a result of the balance between a mean inward drift velocity between a particle pair and the effect of turbulent diffusion. The functional form of the RDF suggested by their study is as follows

$$g(r) = c_0\left(\frac{\eta}{r}\right)^{c_1}, \tag{3.15}$$

$$c_1 = 3.61 St_k {\tau_k}^2 \left[S^2 - R^2\right], \tag{3.16}$$

where c_0 is an unspecified matching coefficient whose value depends upon how the locally smooth flow transitions to turbulence at larger separations. S^2 and R^2 are the second invariant of rate of strain and rate of rotation tensors respectively, averaged over ensemble of particle trajectories. The exponential growth of RDF at sub-Kolmogorov scales is attributed by Chun et al. [53] to a negative drift velocity which essentially results from the particles sampling more strain regions of the

flow than rotational regions. Salazar et al. [54] performed both experiments and DNS at Reynolds numbers from 108 to 147 and obtained identical radial distribution functions. The common observation in the studies mentioned thus far is that accumulation is mainly influenced by action of Kolmogorov scale eddies. It should be noted that as the Stokes number tends to zero, the particles resemble fluid tracer particles. On the other hand, at large Stokes numbers, the effect of the fluid turbulent fluctuations is dwarfed by the particle inertia and therefore the particle motion is essentially unresponsive to the flow. Thus the observation of an optimum Stokes number at which accumulation is maximum is not surprising.

Although the above discussion attributes accumulation to the role of the smallest eddies in the flow, it has also been shown in other studies that at higher Reynolds numbers larger eddies do play an important role. As discussed earlier, the coherent structures in the flow field are expected to influence the distribution of inertial particles. As the Reynolds number increases, the range of scales of the fluid structures also goes up, leading to increasingly complex particle configurations. It should be noted that DNS investigations in the early 90's ([13, 37]) were at low Reynolds numbers and as such the scale separation between inertial and dissipative scales was limited. Several recent studies have focussed on the multi-scale nature of accumulation at high Reynolds numbers. In a comprehensive and meticulous study, Yoshimoto and Goto [48] point out to the possibility of preferential accumulation even when the particle response time is much larger than the Kolmogorov time scale in high Reynolds number turbulence. High Re_λ implies presence of wider range of continuous time scales between the Kolmogorov time scale (τ_k) and the eddy turnover time scale of turbulence (T_E). It is seen from their results for $Re_\lambda = 188$ that the length scales of the voids in particle distribution range from Kolmogorov length scale η to turbulent length scale $L_\epsilon \equiv u'^3/\epsilon$. They argued that the void sizes observed in particle distributions at high Reynolds numbers reflect the multi-scale nature of coherent eddies. This is consistent with the power law distribution of hole sizes observed by Boffetta et al. [55] in two-dimensional turbulence. Boffetta et al. [55] suggest that the geometry of particle distribution is influenced by fluid structures characterised by a large set of time scales. The picture that emerges from these studies is that preferential concentration is prevalent at higher Stokes numbers (greater than unity) and is influenced by larger size eddies. In contrast, at very small Stokes numbers, the clustering is governed by the compressible nature of the particle velocity field (discussed in Balkovsky et al. [56]). By relating the

particle velocity field to the fluid velocity, Balkovsky et al. [56] showed that the particle concentration is intermittent and that segregation of particles continues indefinitely in time. Balkovsky et al. [56] also point out the scale invariance at small scales, but note that deviations from uniform distribution for higher Stokes numbers are expected to depend on a broader range of scales. Wood et al. [4] conducted experimental studies to extend the range of Reynolds numbers across which accumulation was studied. The Taylor Reynolds number for their experiments was nearly 230. They used three classes of particles corresponding to Stokes numbers 0.57, 1.33 and 8.10. Using the D measure, they observed that accumulation is maximum at $St_k \approx 1.0$ even at the higher Reynolds number used in their experiment. It is observed from their experimental results that the length scale at which peak D occurs is larger for higher Stokes number particles. This indicates that heavier/larger (high St_k) particles are influenced by the larger eddies in the flow. The bin size dependence of D suggests a peak around bin-size of $8-20\eta$, which is a broader range than found in experiments at lower Re ([49], [3]). Saw et al. [43] reported clustering of particles in HIT at high Reynolds numbers (Re_λ = 440 to 660). Using the pair correlation function to quantify clustering, they observe that strong clustering is mainly limited to scales of 10 times the Kolmogorov length scale and below.

The dependence of clustering phenomenon on Reynolds number has been the subject of many studies. This is important if the findings established from low Reynolds number DNS studies have to be extrapolated to real-world situations. Reade and Collins [42] conducted DNS for Taylor Reynolds numbers ranging from 37.1 to 87.5 and observed a weak increasing trend of accumulation with Reynolds number. The accumulation was characterised by the RDF in their simulations. Similar weak scaling of RDF with Reynolds number was observed by Wang et al. [39] in their DNS study spanning Taylor Reynolds numbers from 24 to 75. Hogan and Cuzzi [6] used both the D_c and D_2 measures for characterising accumulation. They conducted DNS for a much broader Taylor Reynolds number range - 40 to 140. The D_2 measure did not show any dependence on the Reynolds number for the range of Reynolds number investigated in their study. It should be pointed out that they wrongly concluded that D_c measure was also independent of Reynolds number. They normalised the curves for variation of D_c with Stokes number for all Reynolds numbers with the peak value of D_c at that Reynolds number and observed that all the curves fall on top of each other. While this justifies that the qualitative dependence of D_c on Stokes number is inde-

pendent of Re_λ, there is no means to suggest the trend of peak value of D_c with Reynolds number. It should be borne in mind that D_2 and D_c measures depict different qualities of the particle distribution and need not show the same scaling with Reynolds number. Collins and Keswani [40] studied the scaling of RDF with Reynolds number using DNS investigation at Taylor Reynolds numbers from 65 to 152. They found that the RDF saturates to a constant value with increasing Re_λ, for the range of Re_λ in their study. The RDF showed a weakly increasing trend with Reynolds number at higher Stokes number, while at lower Stokes number the effect was negligible. Bec et al. [5], using DNS to probe the dependence of accumulation on Reynolds number, point out that accumulation is independent of Reynolds number at the dissipative scales. They also point out that the same argument may not apply at higher Re_λ. They note the direct relationship between particle distribution and structure of fluid acceleration in the inertial range. van Aartrijk and Clercx [7] used the correlation dimension D_2 as a measure of accumulation and investigated accumulation in both HIT and stratified turbulence. They concluded that accumulation is only weakly dependent on Reynolds number, a conclusion similar to Collins and Keswani [40]. The picture that emerges from this survey is that while the scaling of RDF and its derived measure, D_2 has been well documented in literature, the scaling of D and D_c measures has not been adequately addressed.

The influence of gravity on the dispersion of particles has also been the subject of numerous studies. Wang and Maxey [13] performed DNS of heavy particles in homogeneous isotropic turbulence (HIT) to investigate settling velocities of particles. The Reynolds number at which they investigated concentration distribution of particles was $Re_\lambda = 31$. They observed that the settling velocities of particles in isotropic turbulence are greater than those in a quiescent fluid. Moreover they found that the enhancement of settling velocity is maximum when the particle response time is nearly equal to the Kolmogorov time scale. They quantified the non-homogeneity in the particle distribution using the D_c measure and found that this measure peaks when $St_k \approx 1.0$. The enhanced settling velocity of particles with near-Kolmogorov scale response times has been attributed to preferential accumulation by Aliseda et al. [49]. Addition of a body force (gravity, Coulomb interaction) on the particles can significantly affect the particle dispersion. Yudine [57] hypothesized that heavy particles settling through fluid eddies would disperse less due to what he called the *crossing-trajectories* effect. The motion of a particle from one eddy to another causes it

to lose its correlation faster, leading to a lower dispersion coefficient. Evidently this phenomenon is governed by the relative magnitudes of the particle free-fall velocity and the fluid turbulence intensity. When the particle free-fall velocity is greater than the turbulent fluctuations, the particle dispersion coefficient has been observed to decrease by approximately the inverse of the free-fall velocity [58].

It is noted that alternate mechanisms of accounting for particle clustering have also been proposed recently. Recent studies have linked the multi-scale nature of particle distribution to the clustering of zero-acceleration points in the fluid. Goto and Vassilicos [59] also observe self-similar particle clustering in their simulations of two-dimensional turbulence (similar to results reported by Yoshimoto and Goto [48]). The argument relating the 'stickiness' of zero-acceleration points for particles was initially introduced by Chen et al. [60]. Chen et al. [60] found a good correlation between acceleration stagnation points of fluid and particle clusters for particle response times smaller than the integral scale of turbulence. Their argument essentially implies that zero-acceleration point clusters trap inertial particles. Goto and Vassilicos [61] formalized the so-called 'sweep-stick mechanism' for clustering of heavy particles in three-dimensional turbulence. Primarily the mechanism can be summarized by considering the particle velocity when St_k is small [14], with $\mathbf{u}_p \approx \mathbf{u}_f(\mathbf{x}_p, t) - \tau_p \mathbf{a}(\mathbf{x}_p, t)$. Thus particles on $\mathbf{a} = 0$ points move with these points with velocity $\mathbf{u}_f$. Goto and Vassilicos [61] point out that the 'sweep-stick mechanism' explains the Stokes number dependence of particle clustering summarized as follows. At smaller Stokes numbers only the small-scale eddies are resonant with the particles, while at larger St_k, larger voids appear because particles are resonant with larger eddies. This growth of void size continues until τ_p reaches the integral time-scale of turbulence.

To summarize, is is observed that the Reynolds numbers accessible to DNS are very limited and thus the scaling of accumulation with Reynolds number remains an open question. However the predominant role of Kolmogorov size eddies in causing accumulation is undisputed and some theories predict a vanishingly small effect of Reynolds number on accumulation. These predictions have been corroborated by the saturating behavior of RDF with Reynolds number for the limited range of Reynolds numbers accessible to DNS studies. The scaling of bin-size dependent measures like D with Reynolds number has not been adequately addressed in the literature. In the

present work, different measures of particle distribution have been used to provide a unified picture of accumulation. Using different measures allows us to probe different aspects of the particle distribution.

3.4 Simulation details

The simulations described here follow from the runs for fluid turbulence described in section 2.4.3. In this section, details of particle parameters used for investigating preferential accumulation are provided. The simulations are divided into two categories - (i) without gravity and (ii) with gravity. For the first set of simulations, the parameters are the fluid Reynolds number, Re_λ, and the particle Stokes number, St_k. For a certain fluid Reynolds number (and thus certain mean Kolmogorov timescale), the desired particle Stokes number is attained by setting the particle diameter to a particular value. It is noted however that the actual Stokes number varies during the simulation as the instantaneous Kolmogorov timescale may vary from its stationary mean. Simulations are performed for six eddy turnover times to allow the particles to equilibrate with the fluid and then statistics are taken over the next $8-10$ eddy turnover times. For the simulations incorporating gravitational force, the additional parameter is the non-dimensional gravitational settling velocity v_g^*. In the present study, simulations are reported for $v_g^* = 0.1, 0.2, 0.5, 1.0, 2.0$. The gravitational force acts in the negative x_3 direction for all the simulations.

The Taylor Reynolds numbers investigated in this study are primarily, $Re_\lambda = 24.2, 45.0, 80.6$. A few simulations at $Re_\lambda = 136.0$ are also reported. The flow characteristics for each of these Reynolds numbers are detailed in table 2.2. The time-step size Δt for all simulations at a given Reynolds number is the same as reported in table 2.3. It should be noted that the time-step is less than the particle response time τ_p for all simulations.

The density ratio of particle phase to fluid phase, ρ_p/ρ_f, is 1000 for all simulations reported in this study. The properties of the different particle types employed for each of the Reynolds numbers are listed in table 3.1. It should be noted that the range of Stokes numbers investigated at $Re_\lambda = 136.0$ is limited.

Re_λ	St_k	ϕ_v	d_p/η
	0.2	1.97×10^{-5}	0.06
	0.5	7.86×10^{-5}	0.09
	0.8	1.58×10^{-4}	0.12
	1.0	2.22×10^{-4}	0.13
24.2	3.0	1.15×10^{-3}	0.23
	6.0	3.24×10^{-3}	0.33
	10.0	6.97×10^{-3}	0.42
	20.0	1.97×10^{-2}	0.60
	25.6	2.89×10^{-2}	0.68
	0.2	1.91×10^{-6}	0.05
	0.5	7.56×10^{-5}	0.08
	0.8	1.53×10^{-5}	0.11
	1.0	2.14×10^{-5}	0.12
45.0	3.0	1.11×10^{-4}	0.21
	6.0	3.14×10^{-4}	0.30
	10.0	6.77×10^{-4}	0.38
	20.0	1.91×10^{-3}	0.54
	32.0	3.84×10^{-3}	0.68
	0.2	2.39×10^{-7}	0.06
	0.5	9.44×10^{-7}	0.09
	0.8	1.91×10^{-6}	0.12
	1.0	2.67×10^{-6}	0.13
80.6	2.6	1.15×10^{-5}	0.21
	5.2	3.24×10^{-5}	0.30
	10.4	9.16×10^{-5}	0.42
	20.8	2.59×10^{-4}	0.59
	41.6	7.33×10^{-4}	0.84
	0.5	1.06×10^{-7}	0.09
136.0	1.0	2.99×10^{-7}	0.12
	2.0	8.44×10^{-7}	0.18
	5.0	3.34×10^{-6}	0.28

Table 3.1: Reynolds numbers, Stokes numbers, particle volume fraction and particle sizes for simulations investigating preferential accumulation.

The local particle number density field is calculated simply by counting the number of particles in each volume surrounding a computational node in the domain and dividing by the total number of particles. A few runs were conducted to study the effect of number of particles on the particle statistics. It was found that the difference between using 10^5 and 10^6 particles was not significant for the purpose of the present study. Thus the number of particles, N_p, used in all the simulations reported in this study is 10^5.

For all the simulations, particles are initially randomly distributed throughout the domain. Tests were conducted to verify the influence of initial particle distribution on the final particle configuration. It is observed from figure 3.2 that the D measures of preferential accumulation are independent of the initial particle distribution at $Re_\lambda = 45.0$. Similar agreement has been observed for other indicators of accumulation at the other Reynolds numbers reported in the present study.

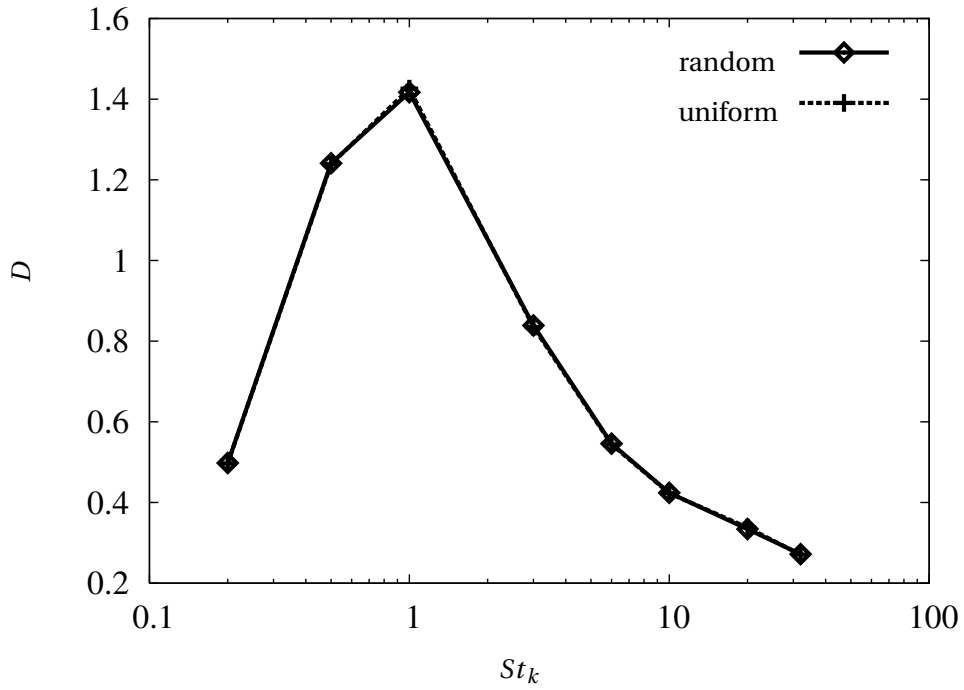

Figure 3.2: Variation of D measure with Stokes number for both random and uniform initial particle distributions at $Re_\lambda = 45.0$. The number of particles used in both simulations is 262144 (=64^3). For uniform distribution, the particles are initialised at the discrete grid points where fluid velocity field is evaluated in physical space.

3.5 Results

Initially it is verified that the particle Reynolds numbers attained in the simulations are less than the limit of applicability of the modified Stokes drag law ($Re_p \leq 800$). The particle Reynolds number increases with increasing settling velocities and thus it has to be monitored for the high non-dimensional settling velocities. Figure 3.3 shows the particle Reynolds numbers for various Stokes numbers and non-dimensional settling velocities for $Re_\lambda = 80.6$. The error-bars in figure 3.3 correspond to $\pm\sigma_n$, the standard deviation of particle Reynolds number variation over the particle

population. It can be seen that the Re_p values are well within the range of validity of the modified Stokes drag law. The Re_p values for the other fluid Reynolds numbers used in this study are of the same order of magnitude as those shown in figure 3.3 and thus within the acceptable limit ($Re_p \leq 800$).

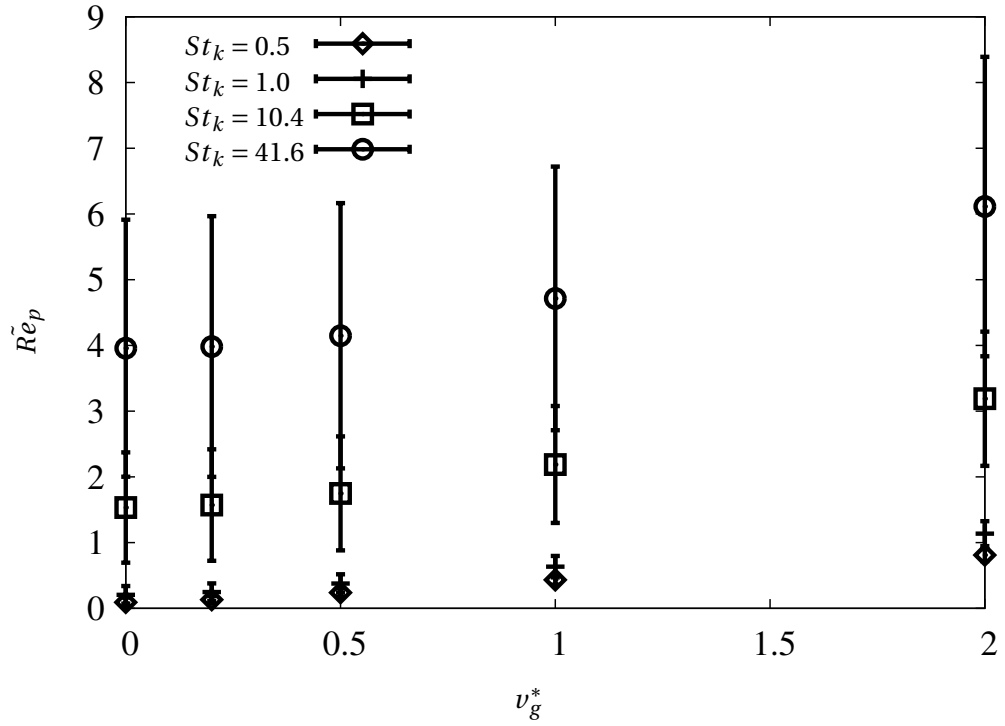

Figure 3.3: Variation of particle Reynolds number (averaged over all the particles) with non-dimensional gravitational settling velocity, v_g^*, for $Re_\lambda = 80.6$.

Simulations have been performed both with and without incorporating the effect of gravity on the particles. Initially results are presented for the cases where gravitational force is neglected in the particle equation of motion. The influence of gravitational settling is separately investigated in section 3.6. Figure 3.4 gives a qualitative picture of particle distribution at different Stokes numbers for $Re_\lambda = 24.2$. It should be noted that the snapshots are taken at the same instant and thus the underlying fluid flow field is the same for all the cases. There appear to be significantly more voids in the particle distribution at $St_k \approx 1.0$. The focus of the present study is to quantify the picture presented in figure 3.4 using the different measures described in section 3.2 and investigate their dependence on fluid and particle parameters.

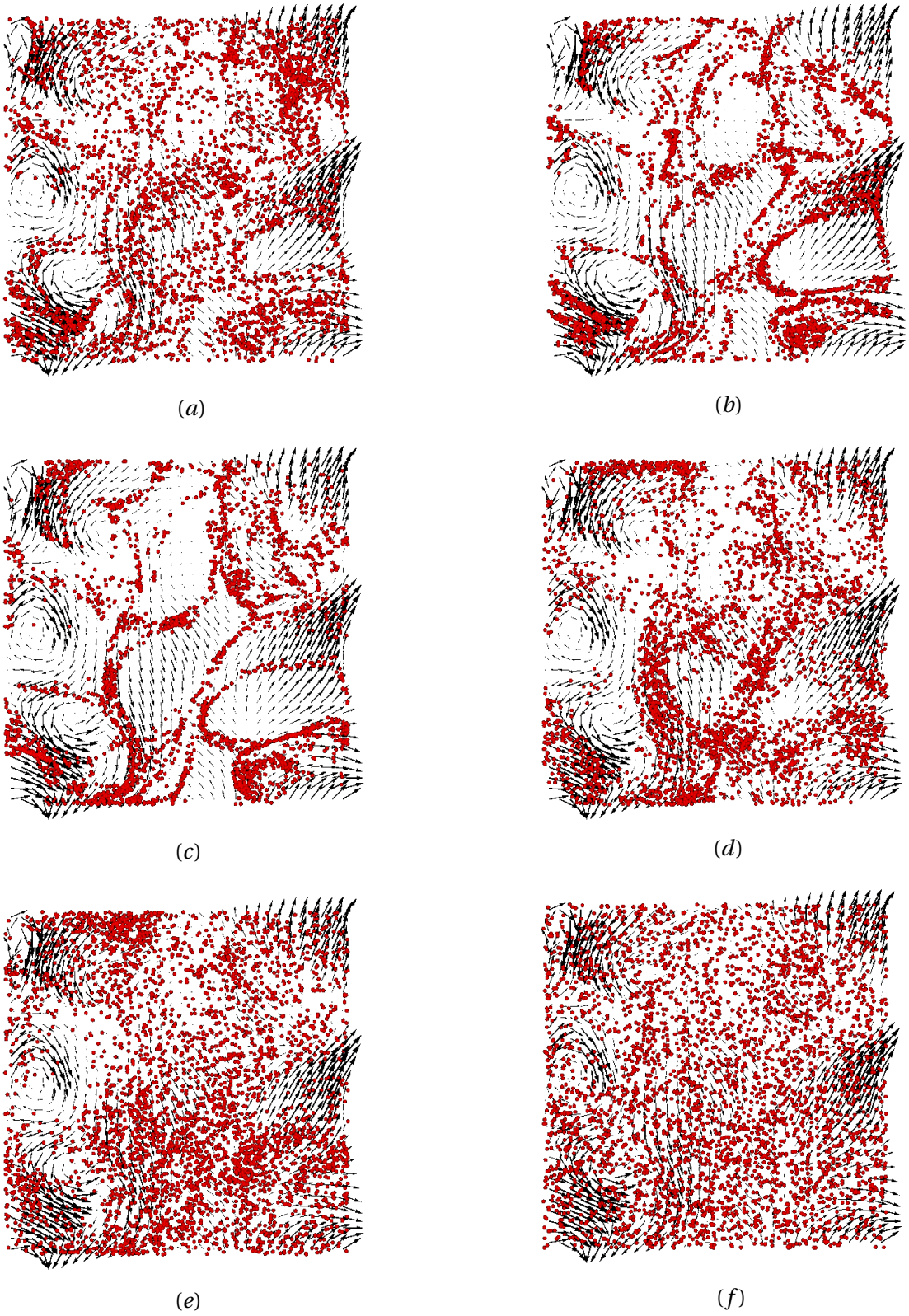

Figure 3.4: Fluid velocity vectors and particle positions for $Re_\lambda = 24.2$ at increasing Stokes numbers - (a) 0.2 (b) 0.5 (c) 1.0 (d) 3.0 (e) 6.4 (f) 20.0.

3.5.1 Measures involving spatial binning

The D and $\langle n'e' \rangle$ measures are Eulerian measures which serve to quantify particle distribution. The method of calculating these measures includes binning of particles in small bins of particular size h as illustrated in figure 3.1. As such the D measure is a function of the bin-size h used for calculating it. Here a systematic analysis of dependence of the D measure on the non-dimensional bin-size, h/η, is presented. Figures 3.5, 3.6, 3.7 and 3.8 show the dependence of D measure on bin-sizes for $Re_\lambda = 24.2$, 45.0, 80.6 and 136.0 respectively.

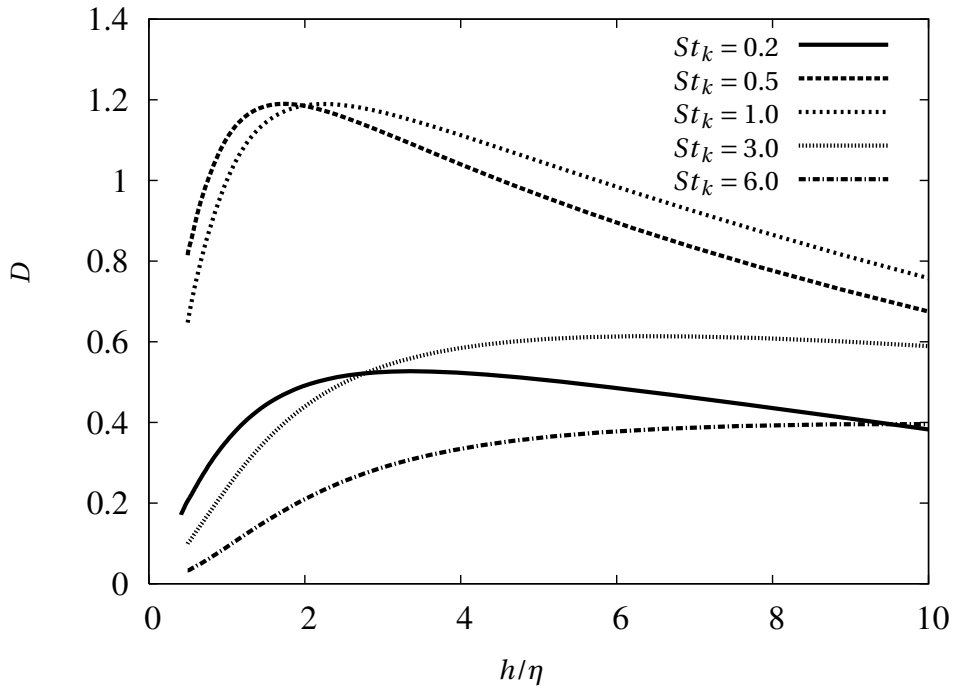

Figure 3.5: Dependence of D measure on non-dimensional bin-size, h/η, at different Stokes numbers for $Re_\lambda = 24.2$.

It is observed that in the accumulated condition, the D measure reaches a peak for a particular non-dimensional bin-size, h/η. It is noted that the Stokes number corresponding to maximum value of D measure goes up with increasing Reynolds number, consistent with experimental observations by Wood et al. [4]. For example, the maxima is attained at $St_k = 1.0$ for $Re_\lambda = 80.6$, while that for $Re_\lambda = 136.0$ is attained at $St_k = 2.0$. The non-dimensional bin-size at which D reaches a maxima can be thought of as the characteristic size of the particle clusters [49]. Smaller bins would contain only parts of a cluster and larger bins would contain information from more than one cluster and thus both distributions would be more homogeneous. An estimate of cluster sizes

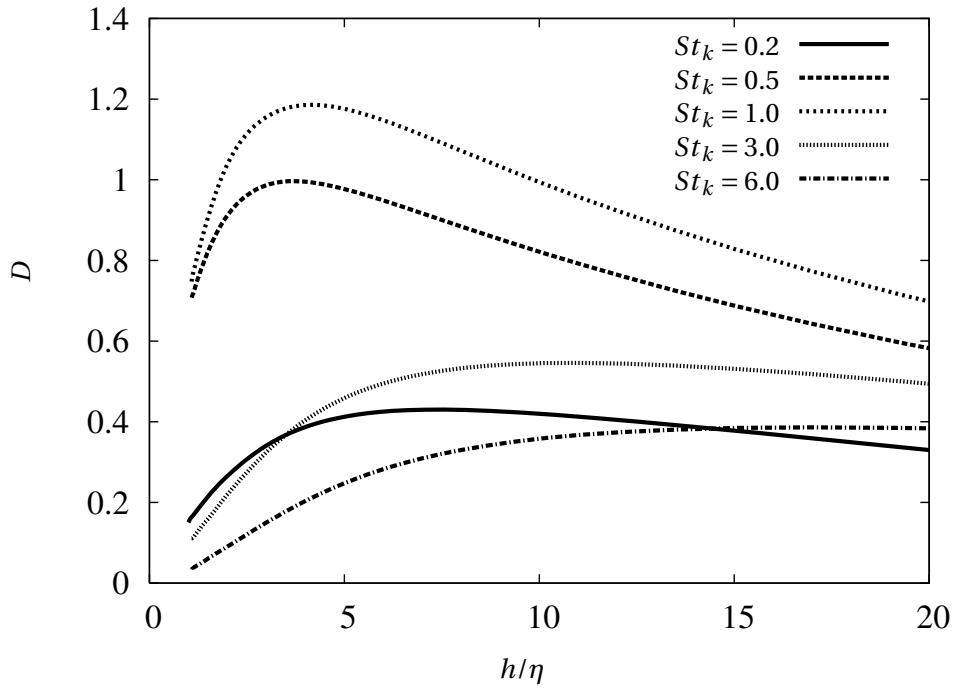

Figure 3.6: Dependence of D measure on non-dimensional bin-size, h/η, at different Stokes numbers for $Re_\lambda = 45.0$.

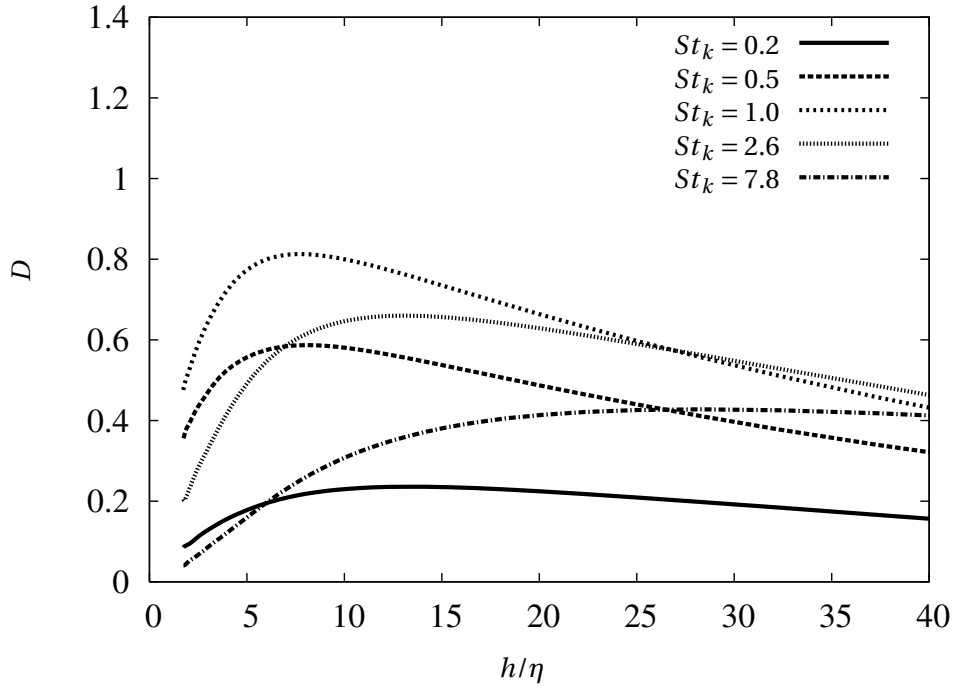

Figure 3.7: Dependence of D measure on non-dimensional bin-size, h/η, at different Stokes numbers for $Re_\lambda = 80.6$.

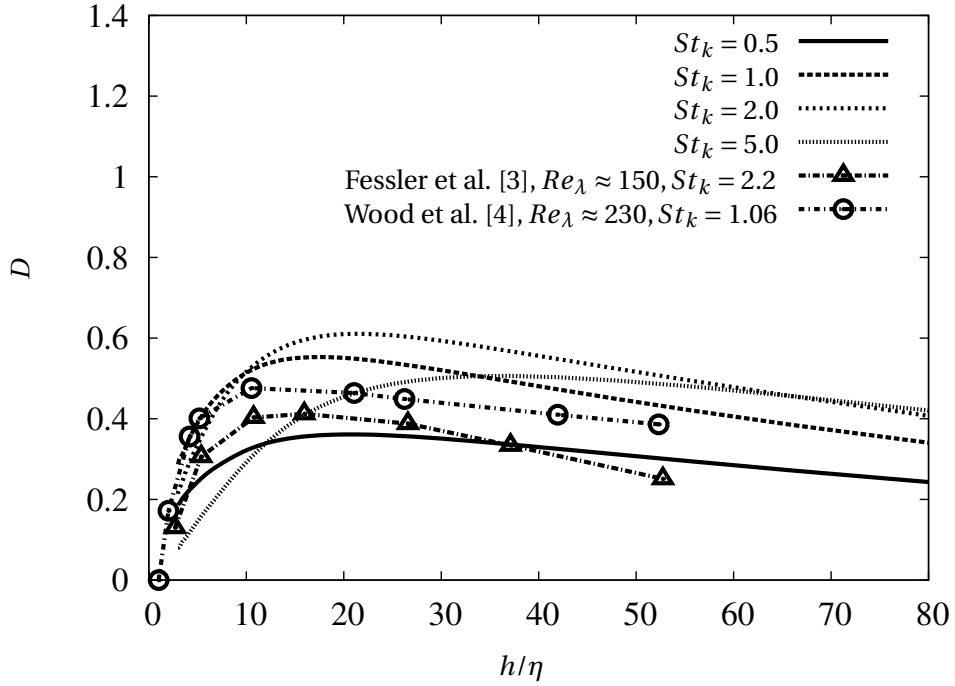

Figure 3.8: Dependence of D measure on non-dimensional bin-size, h/η, at different Stokes numbers for $Re_\lambda = 136.0$. Also shown are results from experiments by Fessler et al. [3] and Wood et al. [4].

can be obtained by noting the h/η corresponding to the peak of the D measure at $St_k = 1.0$. The cluster sizes inferred in this way at $St_k = 1.0$ are 2.1η, 4.7η, 7.4η and 18.2η for $Re_\lambda = 24.2$, 45.0, 80.6 and 136.0 respectively. This observation compares well with the cluster size 10η at $Re_\lambda = 75$ observed by Aliseda et al. [49] in their experiments. It is observed that at Stokes numbers near unity, there is a sharp peak (particular length scale) at which accumulation is most prominent, thus signifying that the particle distribution is dominated by clusters of a particular size. On the other hand, at very low or high Stokes numbers, there is a range of cluster sizes present in the distribution. Particularly, the high Stokes number particles are observed to cluster even at length scales an order of magnitude greater than the Kolmogorov length scale. This can be qualitatively explained by the interaction of these sluggish particles with a broad range of eddy sizes. The shift in the peak of D measure to small scales at smaller Stokes number is consistent with the observations of Fessler et al. [3] in their experiments. The highest Reynolds number simulation in this study ($Re_\lambda = 136$) is comparable to the channel-flow experiment of Fessler et al. [3] since the ratio of the Taylor length scale to the Kolmogorov length scale in both situations is roughly 20. Fessler et al. [3] found maximum overall concentration at $St_k = 2.8$ and non-dimensional bin-size, $h/\eta = 15.8$

in their experiments. These values compare very well with the optimum Stokes number, $St_k = 2.0$, and bin-size, $h/\eta = 18.2$, observed in the present simulations (Figure 3.8) at about the same turbulence level. Moreover the D measure dependence on bin-size captured in the simulations is remarkably similar to that reported by Fessler et al. [3] at the centerline (nearly homogeneous section) of their channel flow experiments. The quantitative discrepancy between simulations and experiment of Fessler et al. [3] can be attributed to the difference in mean particle number density for these cases. The bin-size dependence for the highest Re_λ in the present simulations also agrees qualitatively with the experimental data from Wood et al. [4] as observed in figure 3.8. The Reynolds number in the experiment of Wood et al. [4] is much higher, which may account for the quantitative discrepancy, along with the two-way coupling effect inherent in experiments. It is also observed that the peak value of the D measure goes down with Reynolds number.

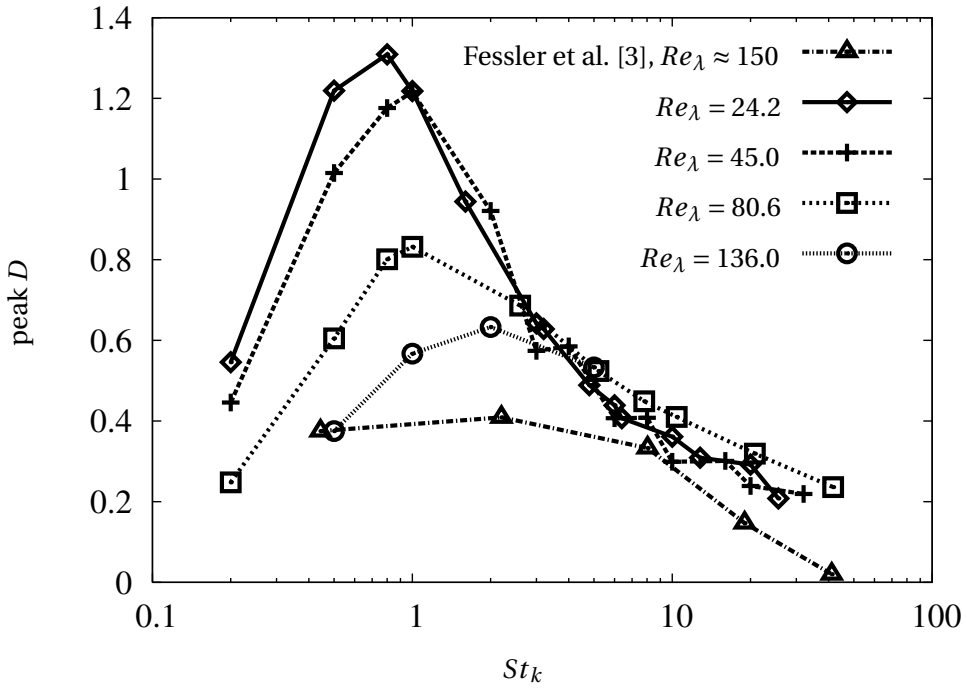

Figure 3.9: Variation of peak D measure with Stokes number for $Re_\lambda = 24.2, 45.0, 80.6, 136.0$ compared with experimental data from Fessler et al. [3]. The D value shown is the peak value (irrespective of bin-size) for a snapshot of particle distribution.

Though the bin-size dependence of the D measure allows us to probe the scale at which particles are accumulated, it is desirable to associate a single value of D with a given particle distribution. This would facilitate isolation of the effect of Stokes number on the D measure regardless of bin-size. Figure 3.9 shows the variation of peak D values with Stokes numbers for the different

Reynolds numbers investigated in the present work and also compares the simulation results with the experimental data reported by Fessler et al. [3]. It is observed that the results from the present study tend to the experimental results of Fessler et al. [3] with increasing Reynolds numbers. It is interesting to note that for Stokes numbers less than unity, preferential concentration decreases significantly with increasing Taylor Reynolds numbers. While at higher Stokes numbers, preferential concentration is relatively higher for higher Taylor Reynolds numbers though overall there is almost no preferential accumulation at these high Stokes numbers. It is observed that there is a decrease in D with Reynolds number for Stokes numbers less than 3. The values of D are essentially a reflection of the presence of bins having greater or lower number of particles than the mean number, λ. Figure 3.10 captures this feature by showing the probability of presence of bins with c particles at a particular bin-size. The bin-size chosen for figure 3.10 is $h/\eta = 2.1$, the size at which D reaches a maxima for $St_k = 1.0$ and $Re_\lambda = 24.2$. It is seen from figure 3.10 that when the particles are preferentially accumulated, there are nearly three times as many voids (c=0) in the domain than a random distribution. For the $St_k = 1.0$ case, the particle concentration in one of the bins is as high as 50 times the mean concentration (not seen in figure). Also it can be noted that at $St_k = 6.0$, the distribution is closest to a Poisson distribution.

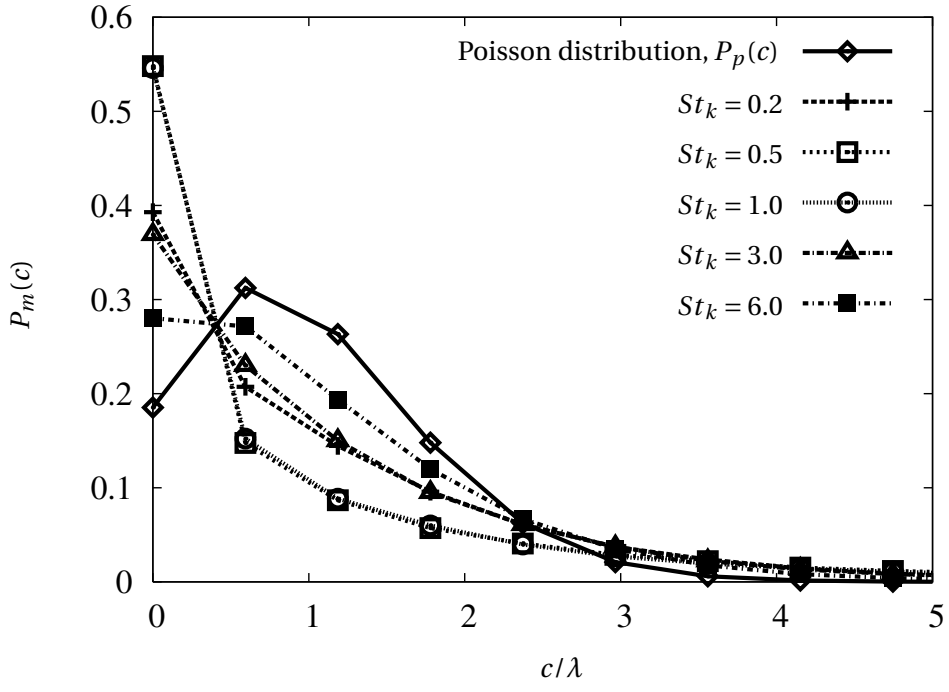

Figure 3.10: Particle number density distribution function for a random distribution and different Stokes numbers for $Re_\lambda = 24.2$ at $h/\eta = 2.1$.

As discussed in section 3.3, it is well documented that particles tend to reside in low vorticity areas of the flow when they are preferentially concentrated. The quantity $\langle n'e' \rangle$ takes increasing negative values as the particles accumulate in low-vorticity regions. Figure 3.11 shows the variation of $\langle n'e' \rangle$ with Stokes number for different Reynolds numbers. The negative values of $\langle n'e' \rangle$ indicate that regions of above/below average particle number density correspond to regions of below/above average vorticity respectively. Thus the $\langle n'e' \rangle$ measure clearly demonstrates the tendency of particles to accumulate in areas of low vorticity, reaching a minima in the Stokes number range of $St_k \approx 0.5 - 1.0$. In addition, it is also noted that the variation of this measure, across the range of Stokes numbers considered, reduces for the more turbulent simulations. At the highest Reynolds number in the simulations, particles with Stokes numbers $St_k = 5$ and $St_k = 0.5$ have similar $\langle n'e' \rangle$ values and thus demonstrate same affinity to low vorticity areas.

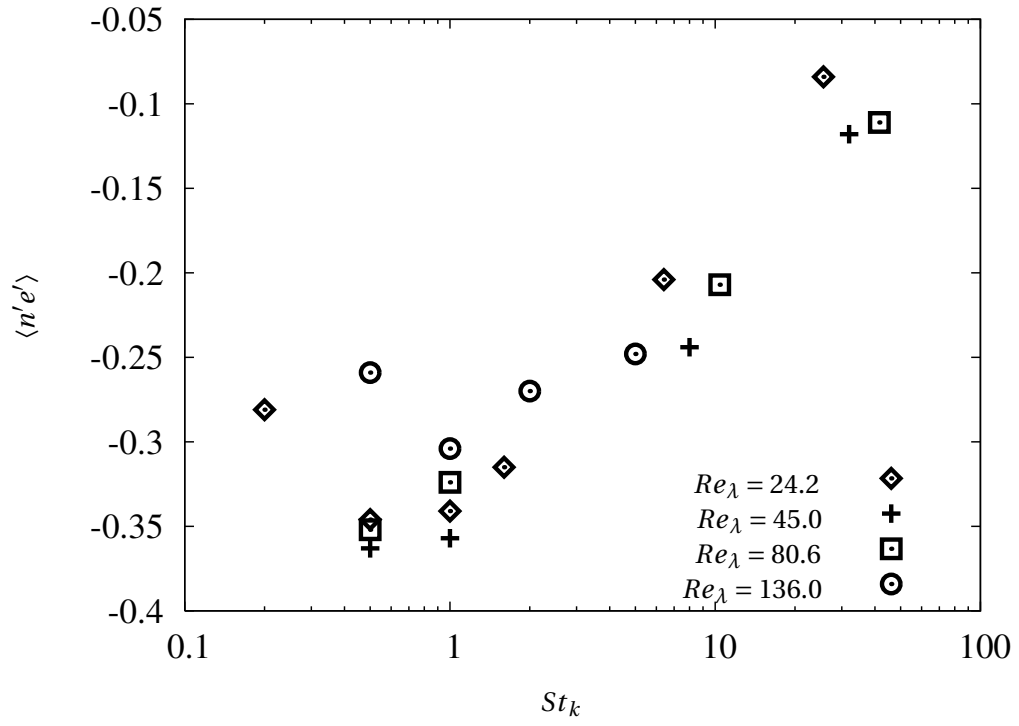

Figure 3.11: Variation of correlation of particle number density and enstrophy,$\langle n'e' \rangle$, with Stokes number for $Re_\lambda = 24.2, 45.0, 80.6, 136.0$.

In order to further investigate the scaling of preferential accumulation with Reynolds number, the particle number density spectra are calculated for each simulation by taking the Fourier transform of the particle number density field. The clustering length scale, l_n (Equation 3.13), is defined by analogy with the carrier flow integral length scale. The variation of clustering length scale across

St_k for different Re_λ is shown in Figure 3.12. It is observed that the clustering length scale also shows a peak for $St_k \approx 1.0$. It is noted that the difference in peak and asymptotic value reached at higher St_k is much smaller at highest Re_λ. This is attributed to the fact that at higher St_k and Re_λ, the clusters are more diffuse structures. It is suggested that whilst the process of preferential accumulation is governed by small scale features of the turbulence for low Reynolds numbers, at higher Reynolds numbers, the clustering is influenced by a broad range of eddy sizes.

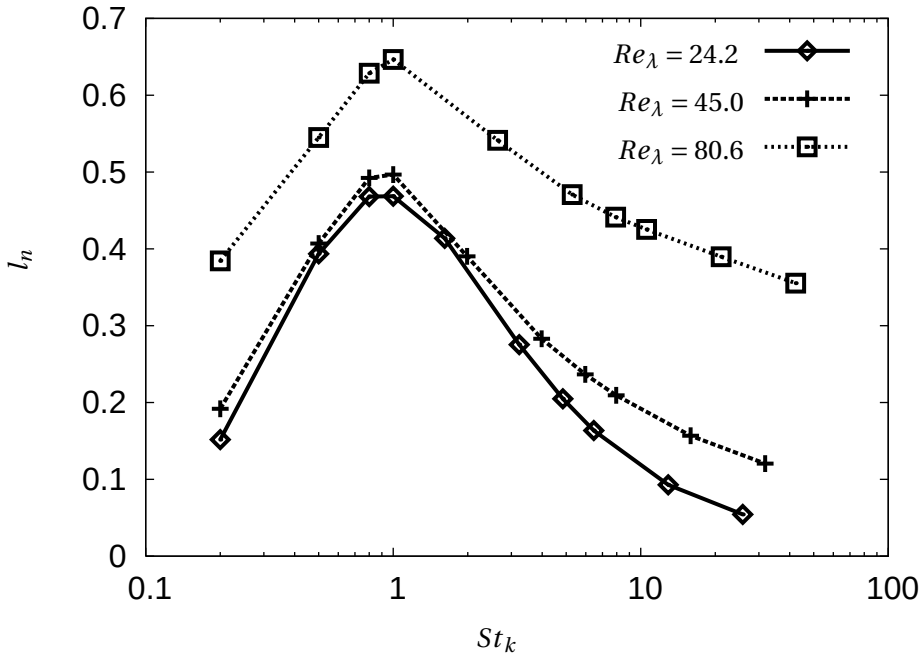

Figure 3.12: Variation of clustering length scale, l_n, with Stokes number for different Reynolds numbers.

3.5.2 Radial distribution function and correlation dimension

As discussed earlier, accumulation occurs over a range of scales extending from the smallest dissipative eddies to the integral scales of turbulence. The radial distribution function (RDF), introduced in section 3.2, is one of the measures which captures the multi-scale nature of accumulation. Radial densities significantly greater than unity would be an indicator of accumulation at corresponding radial scales. Figures 3.13, 3.14 and 3.15 show the radial distribution functions at different Stokes numbers for Re_λ = 24.2, 45.0 and 80.6 respectively. It is apparent that in the preferentially accumulated condition the RDF values jump by an order of magnitude to values of roughly 50. It is also observed that accumulation exists over a very wide range of scales - from the

Kolmogorov scales to order of around ten times the Kolmogorov length scale.

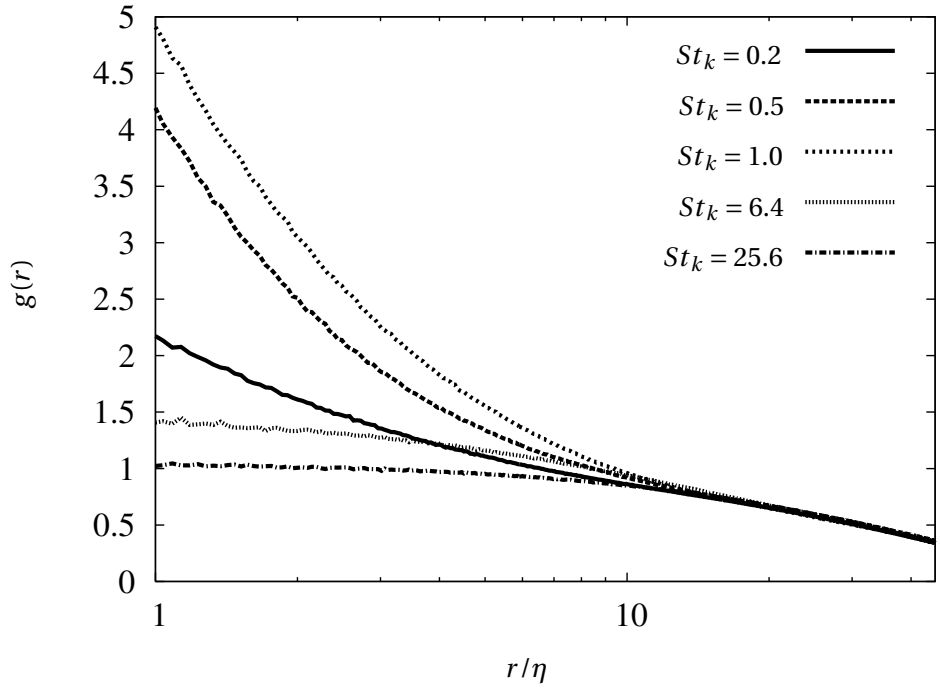

Figure 3.13: Radial distribution functions at different Stokes numbers for $Re_\lambda = 24.2$.

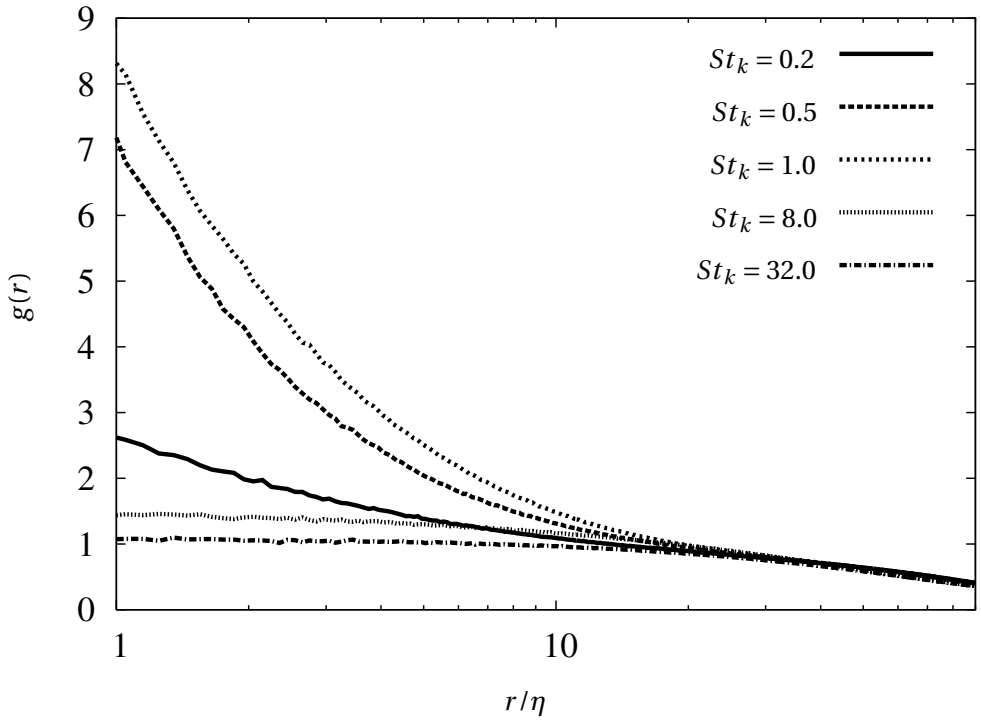

Figure 3.14: Radial distribution functions at different Stokes numbers for $Re_\lambda = 45.0$.

It is interesting to probe the clustering at the scale of the small-scale eddies. The RDF evaluated

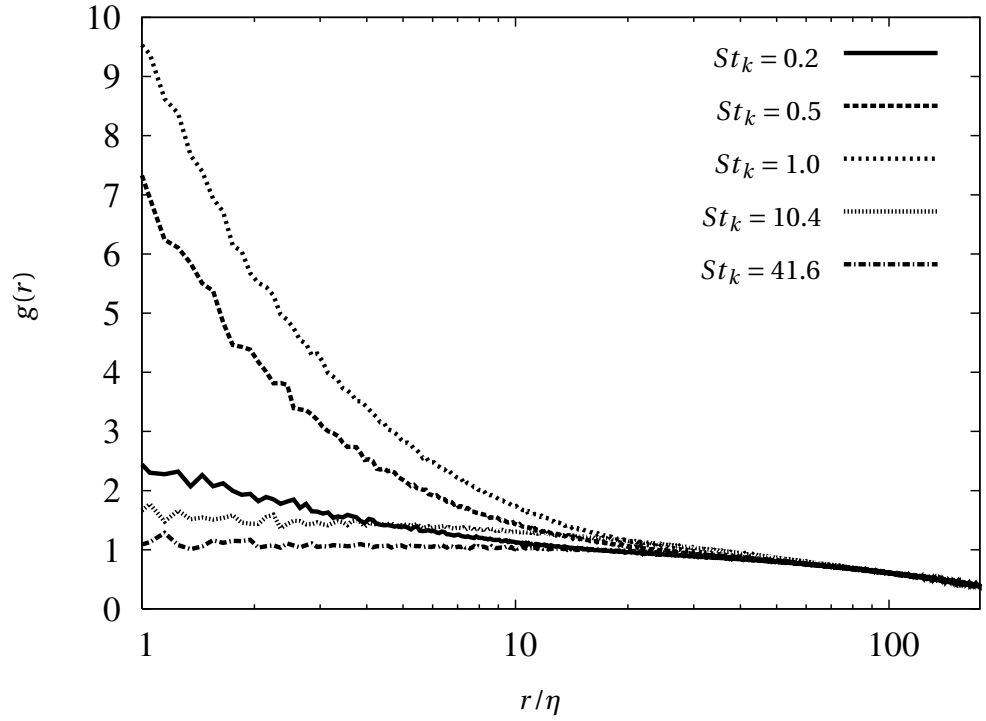

Figure 3.15: Radial distribution functions at different Stokes numbers for $Re_\lambda = 80.6$.

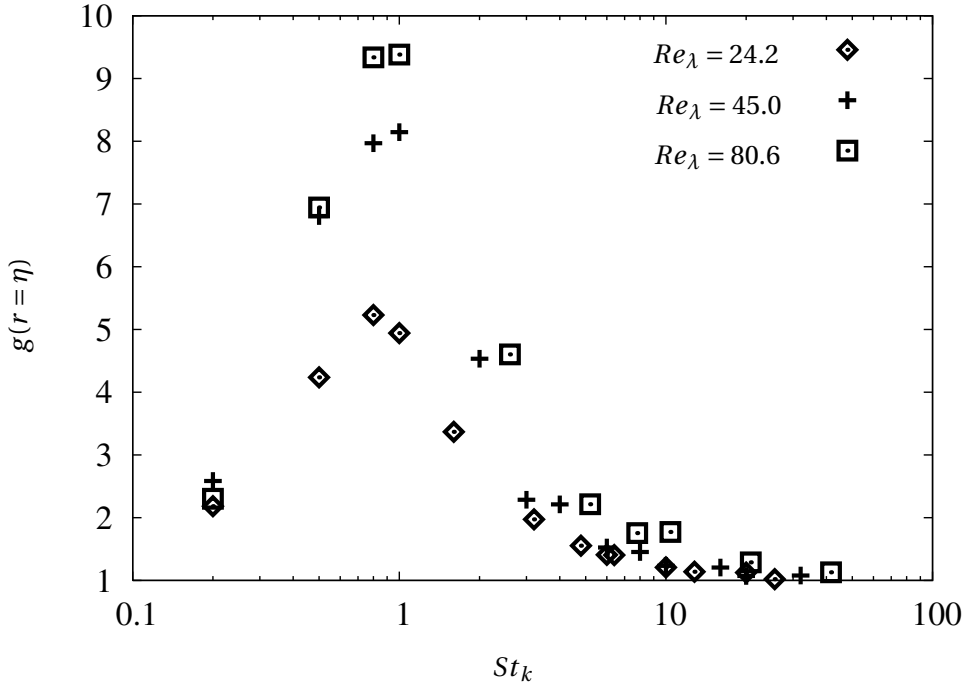

Figure 3.16: Variation of RDF evaluated at $r = \eta$ for different Reynolds and Stokes numbers.

at $r/\eta = 1.0$ is shown in figure 3.16 for different Reynolds numbers. This plot indicates that the RDF values are higher for increasing Reynolds numbers for the Reynolds numbers considered in

this study. Reade and Collins [42] also observed that a growth in RDF evaluated at $r/\eta = 0.025$ with increasing Reynolds numbers. In addition, dependence of accumulation on Stokes number is captured, showing a peak value for $St_k \approx 1.0$ at all Reynolds numbers.

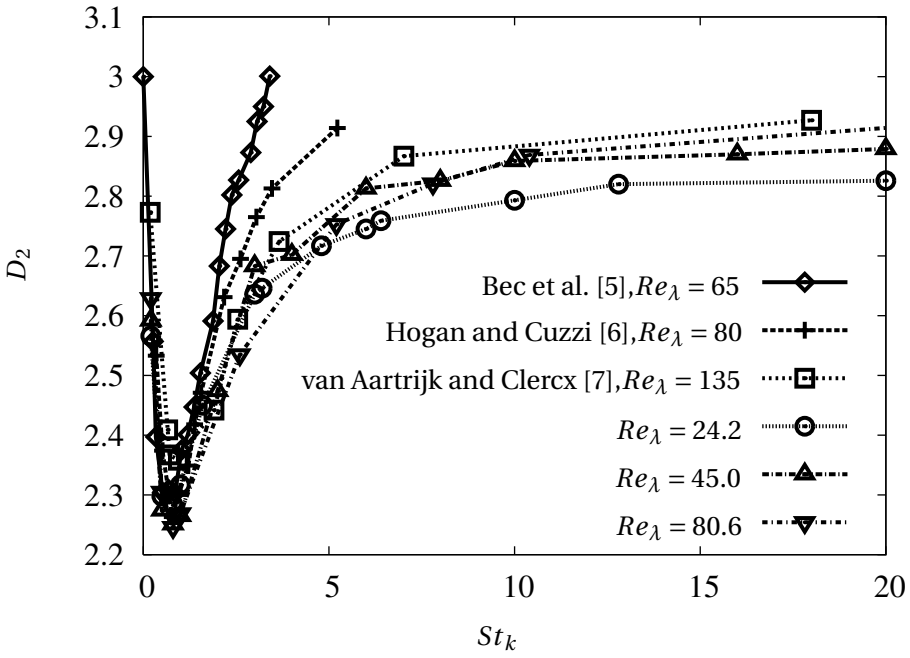

Figure 3.17: Variation of D_2 measure with Stokes number for $Re_\lambda = 24.2, 45.0, 80.6$ and compared with data from Bec et al. [5], Hogan and Cuzzi [6] and van Aartrijk and Clercx [7]

.

Figure 3.17 shows the variation of correlation dimension, D_2 with St_k for different Reynolds numbers, compared with results from Bec et al. [5], Hogan and Cuzzi [6] and van Aartrijk and Clercx [7]. The dependence of the D_2 measure on Stokes number shows the same pattern as the other measures pointing to maximum accumulation around $St_k \approx 1.0$. It is observed that the D_2 measure exhibits only a weak dependence on Reynolds number, consistent with similar conclusion by Collins and Keswani [40]. The D_2 measure can be thought of as a qualitative indicator of scaling of particle-particle separations in a cluster. It is evident that D_2 is insensitive to the range of eddy sizes in the carrier flow. It is noted that the Kolmogorov length scale decreases by an order of magnitude from the lowest to highest Reynolds number. Thus D_2 being nearly independent of Reynolds number, only serves to demonstrate that the structure of a cluster of particles as viewed by a single particle within the cluster continues to remain the same with increasing Re_λ.

3.6 Effect of gravitational settling

The magnitude of the gravitational settling force has been characterised in the present work by the non-dimensional settling velocity v_g^* (introduced in in section 2.4.2). v_g^* is representative of the magnitude of the terminal velocity imparted to the particles by gravitational force scaled by the intensity of fluid turbulence fluctuations. Simulations have been performed up to $v_g^* = 2.0$ to investigate the effect of increasing the settling force. The primary effect of increasing the settling force is the so-called *crossing trajectories* effect first proposed by Csanady [58]. This effect is manifested in the form of loss of the Lagrangian particle velocity autocorrelation in the direction perpendicular to the direction of the settling force. The Lagrangian particle velocity autocorrelation, $R_{lp,i}$, is defined as

$$R_{lp,i}(s) = \frac{\langle\langle u_{p,i}(t)\, u_{p,i}(t+s)\rangle\rangle}{\langle\langle u_{p,i}(t)^2\rangle\rangle}. \tag{3.17}$$

Since gravity acts in the negative x_3 direction in all the simulations, the Lagrangian particle velocity autocorrelation in the x_1 (or x_2) direction is of particular interest in the present context. The trajectories of all the particles in the simulation are stored for the purpose of calculating $R_{lp,1}$. The autocorrelation of u_1 is then calculated as a function of the separation in time s. The averages in equation 3.17 are ensemble averages over different sampling times along the trajectory of the particle. For the purpose of greater statistical accuracy, the autocorrelation curves are averaged over the trajectories of all the particles in the simulation.

Initially, particle velocity autocorrelations in x-direction for zero gravity case are plotted in figures 3.18 and 3.19 for different fluid Reynolds numbers and particle Stokes numbers. It is clear that the velocities of the high Stokes number particles stay correlated for longer time.

The so-called crossing trajectories effect is seen in figures 3.20 and 3.21. With increasing v_g^*, the particles tend to lose autocorrelation of their velocities in x-direction much faster. This is due to the fact that the particle rapidly passes through several different eddies as it settles in the direction of gravity.

The loss in autocorrelation with increasing v_g^* implies that the particle dispersion in the direction perpendicular to gravity is reduced. To observe this effect, initially the mean displacement of par-

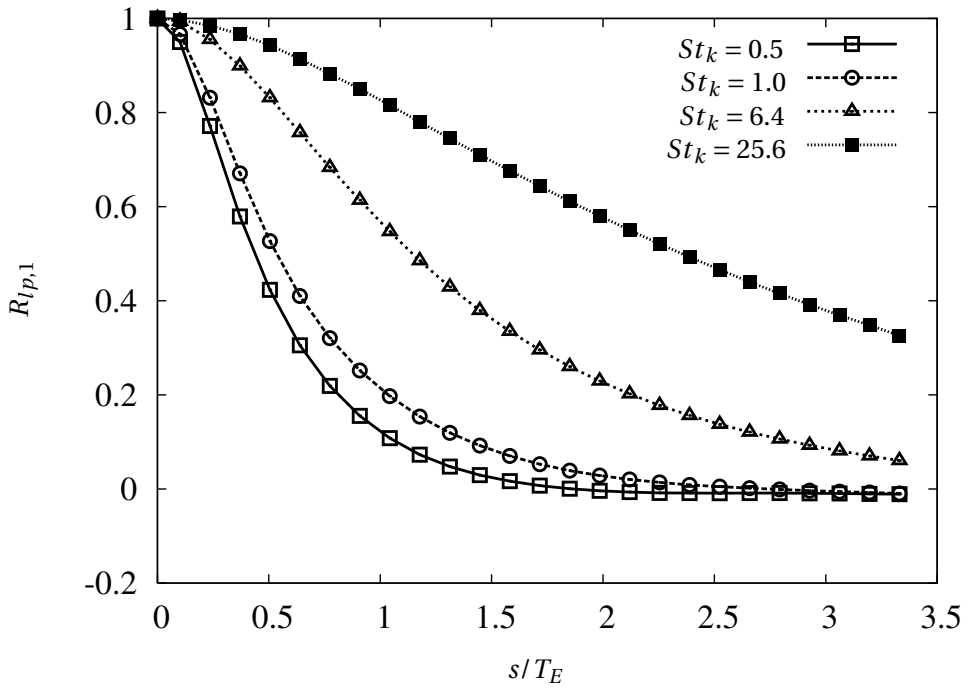

Figure 3.18: Lagrangian autocorrelation coefficient of particle velocity in x-direction, $R_{lp,1}$ at different Stokes numbers for Re_λ = 24.2. for zero gravity case. Note the time axis is non-dimensionalised using fluid turbulence eddy turnover time as reference.

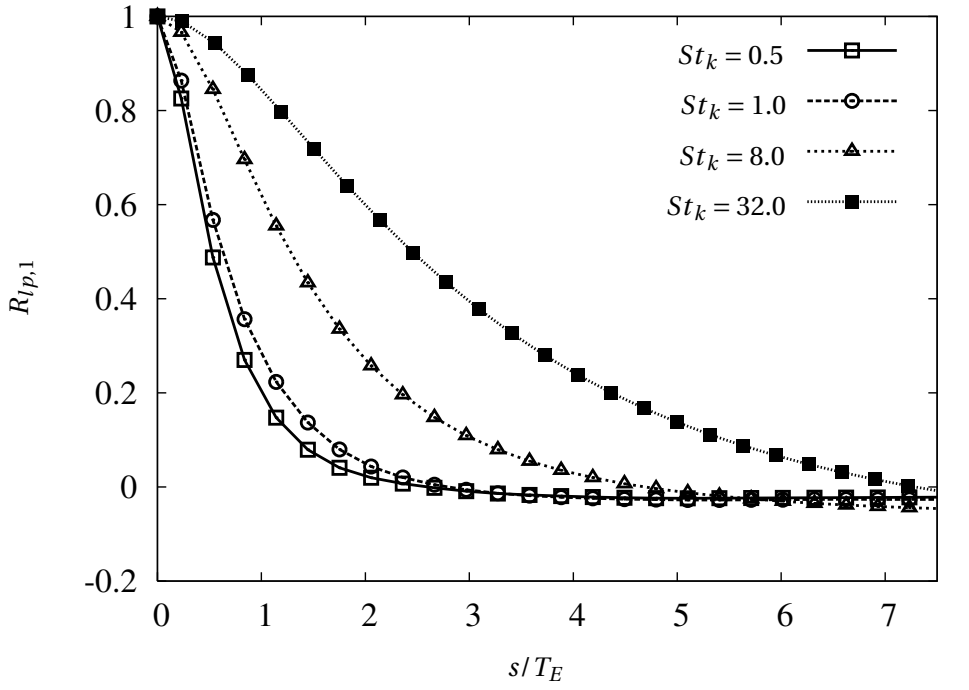

Figure 3.19: Lagrangian autocorrelation coefficient of particle velocity in x-direction, $R_{lp,1}$ at different Stokes numbers for Re_λ = 45.0. for zero gravity case. Note the time axis is non-dimensionalised using fluid turbulence eddy turnover time as reference.

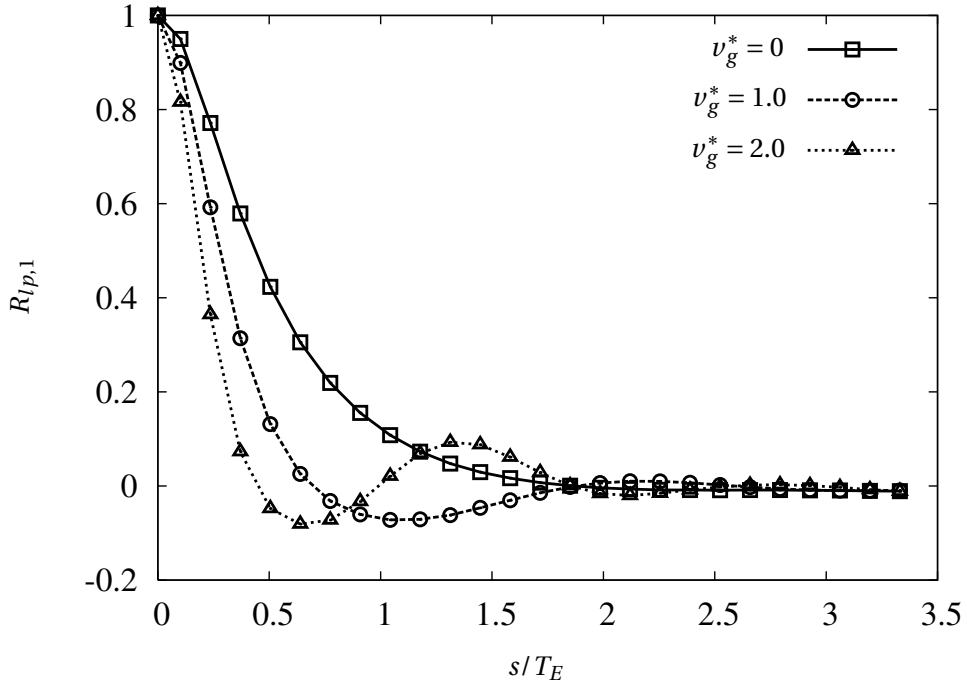

Figure 3.20: Lagrangian velocity autocorrelation of particles in x-direction, $R_{lp,1}$ at different non-dimensional gravitational settling velocities for $Re_\lambda = 24.2, St_k = 0.5$.

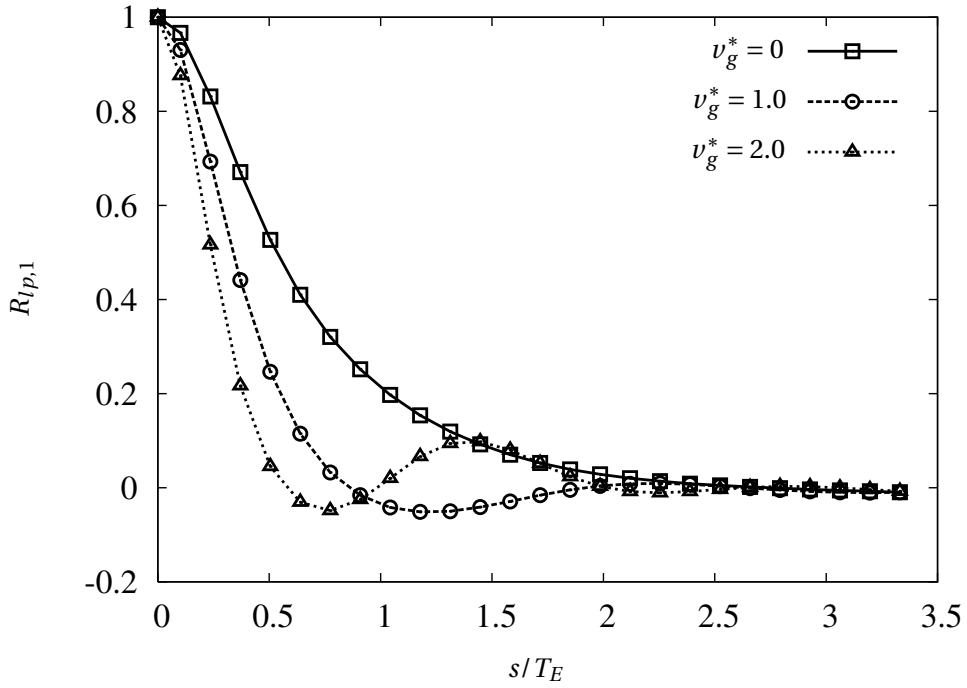

Figure 3.21: Lagrangian velocity autocorrelation of particles in x-direction, $R_{lp,1}$ at different non-dimensional gravitational settling velocities for $Re_\lambda = 24.2, St_k = 1.0$.

ticles in x-direction with time is shown for particles of different Stokes numbers for $Re_\lambda = 24.2$ in figure 3.22. It is seen that high Stokes number particles tend to disperse more due to their higher velocity autocorrelation.

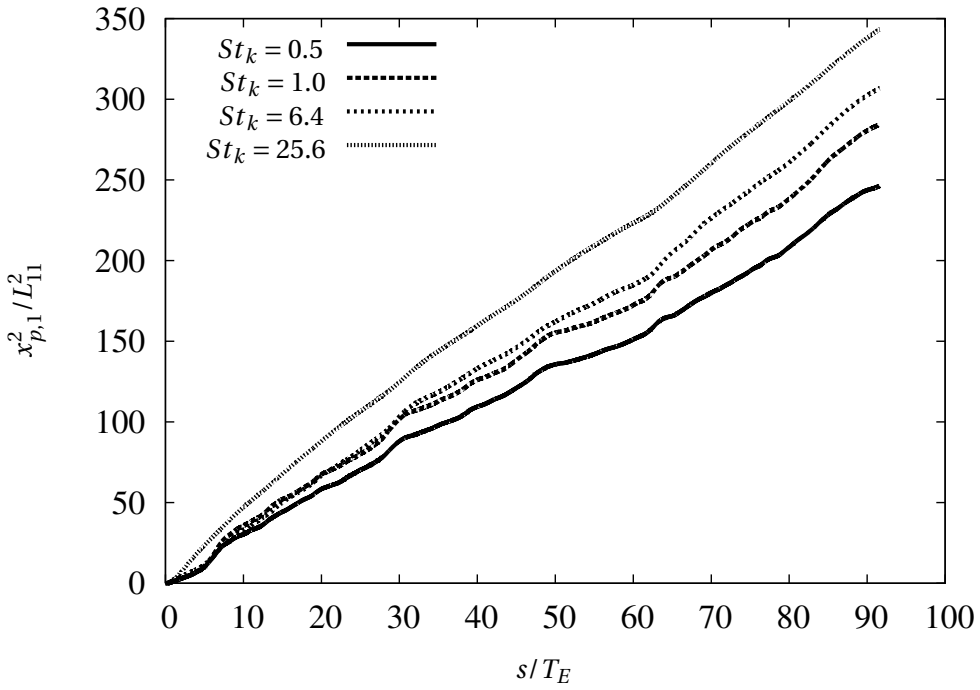

Figure 3.22: Normalised mean square displacement in x-direction at different Stokes numbers for $Re_\lambda = 24.2$.

Increasing v_g^* leads to significant reduction in dispersion, as seen in figure 3.23 for $St_k = 0.5$ particles. It is thus clear that the v_g^* values used in present work are sufficient to have an appreciable effect on particle dispersion characteristics.

The effect of increasing v_g^* on the different indicators of accumulation is explored next.

The effect of gravity is to mitigate accumulation for low Stokes number particles, as seen in figures 3.24, 3.25, 3.26. It is observed that increasing gravity reduces the preferential accumulation of particles in low enstrophy areas for low Stokes numbers. The gravitational force tends to counteract the centrifugal force on the particle due to the highly rotational eddies. This allows the particles to reside in high enstrophy areas. At the higher Stokes numbers, the accumulation is not pronounced even in the absence of gravity and thus increasing gravitational settling velocity does not have a significant effect. It is noted that increasing non-dimensional settling velocity from $v_g^* = 1.0$ to 2.0 leads to increased accumulation at high Stokes numbers.

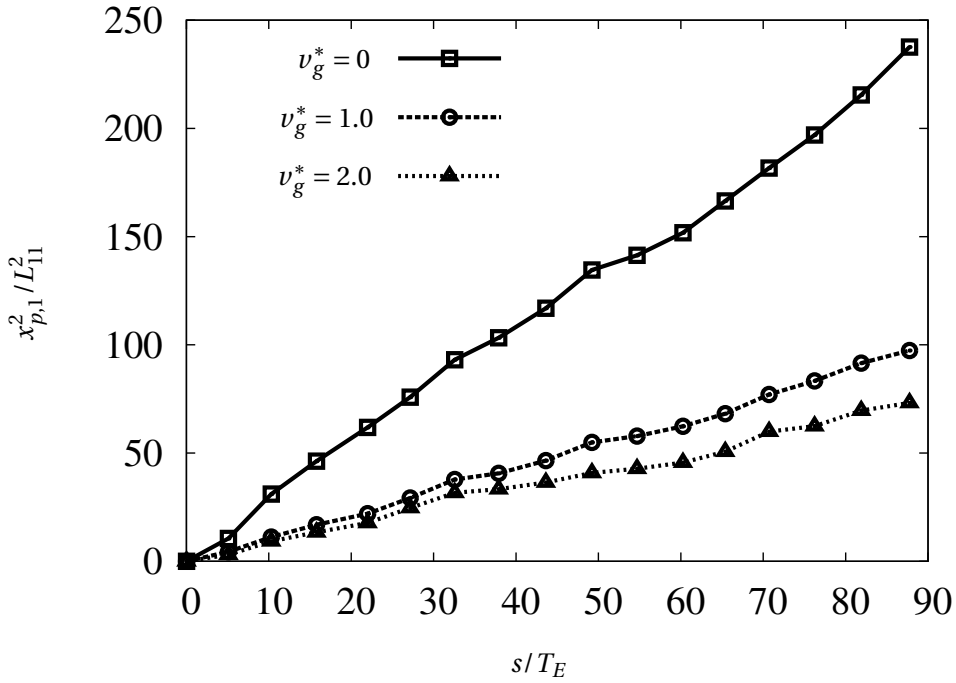

Figure 3.23: Normalised mean square displacement in x-direction at different non-dimensional gravitational settling velocities for $Re_\lambda = 24.2, St_k = 0.5$.

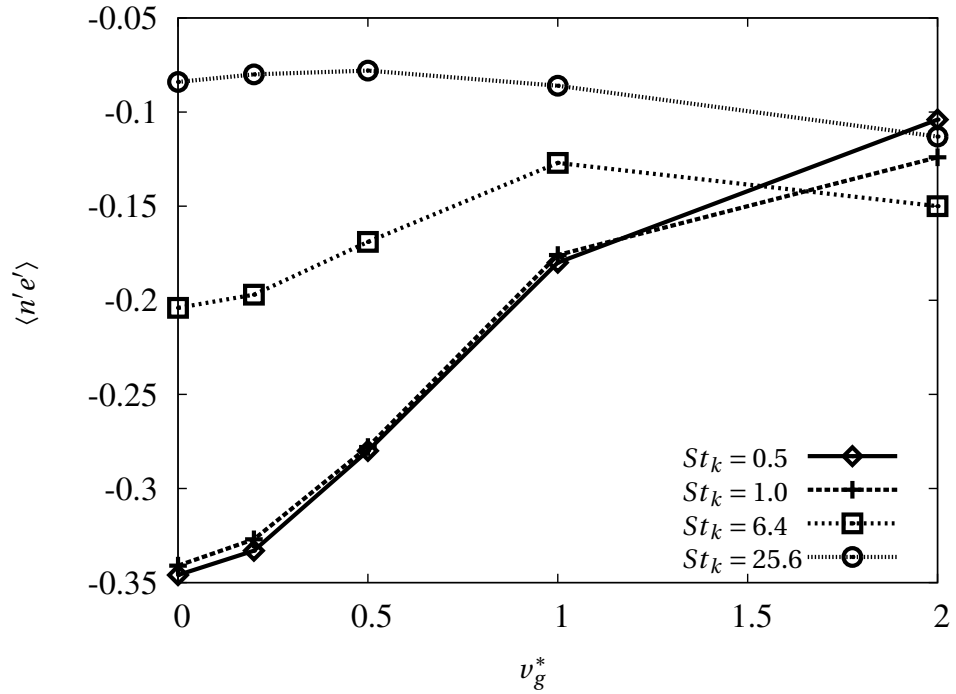

Figure 3.24: Variation of $\langle n'e' \rangle$ with non-dimensional gravitational settling velocity at different Stokes numbers for $Re_\lambda = 24.2$.

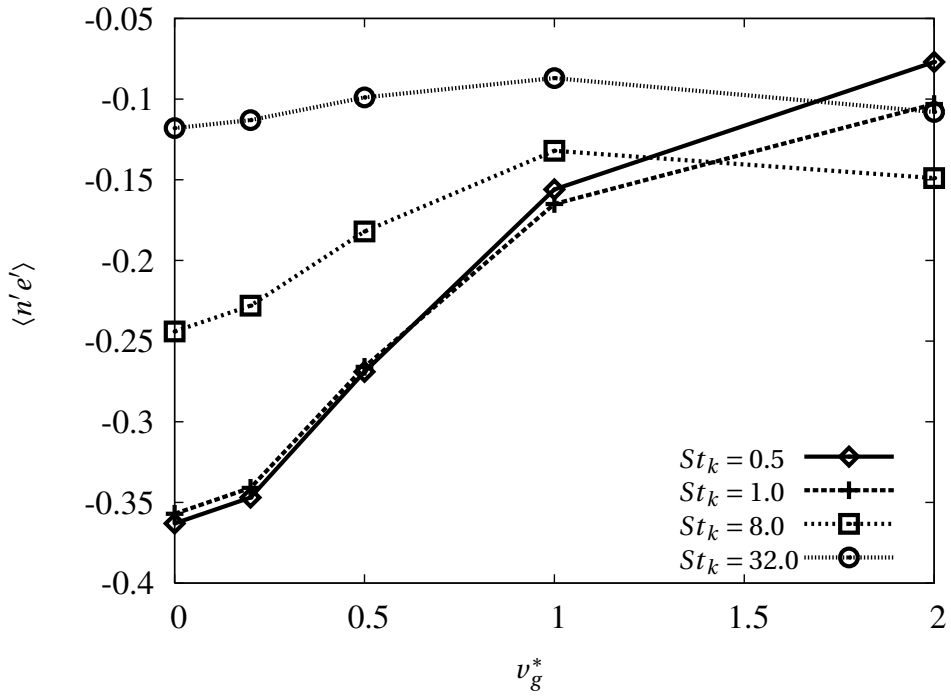

Figure 3.25: Variation of $\langle n'e' \rangle$ with non-dimensional gravitational settling velocity at different Stokes numbers for $Re_\lambda = 45.0$.

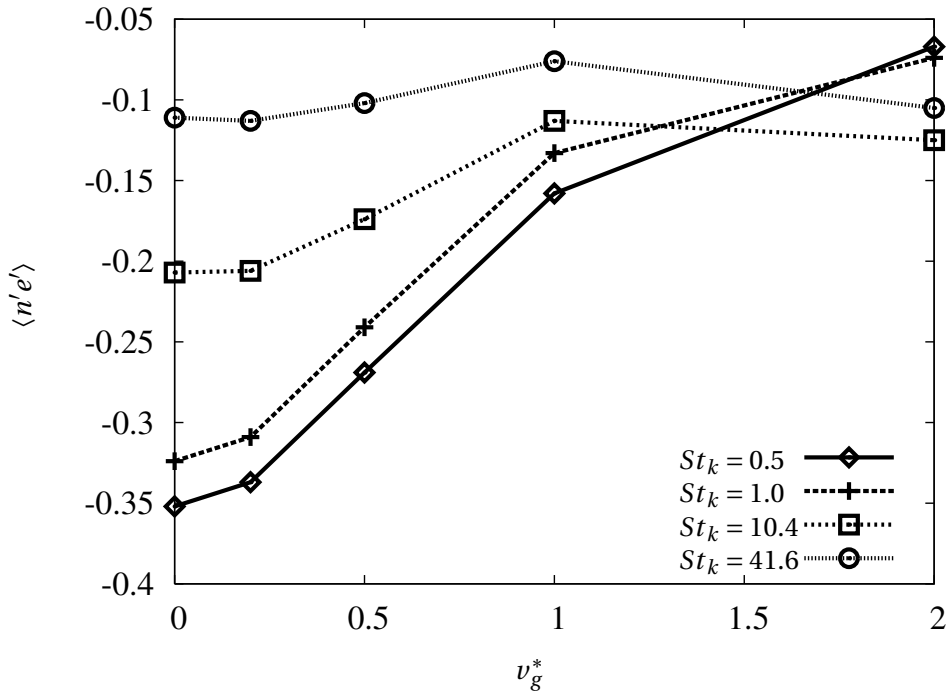

Figure 3.26: Variation of $\langle n'e' \rangle$ with non-dimensional gravitational settling velocity at different Stokes numbers for $Re_\lambda = 80.6$.

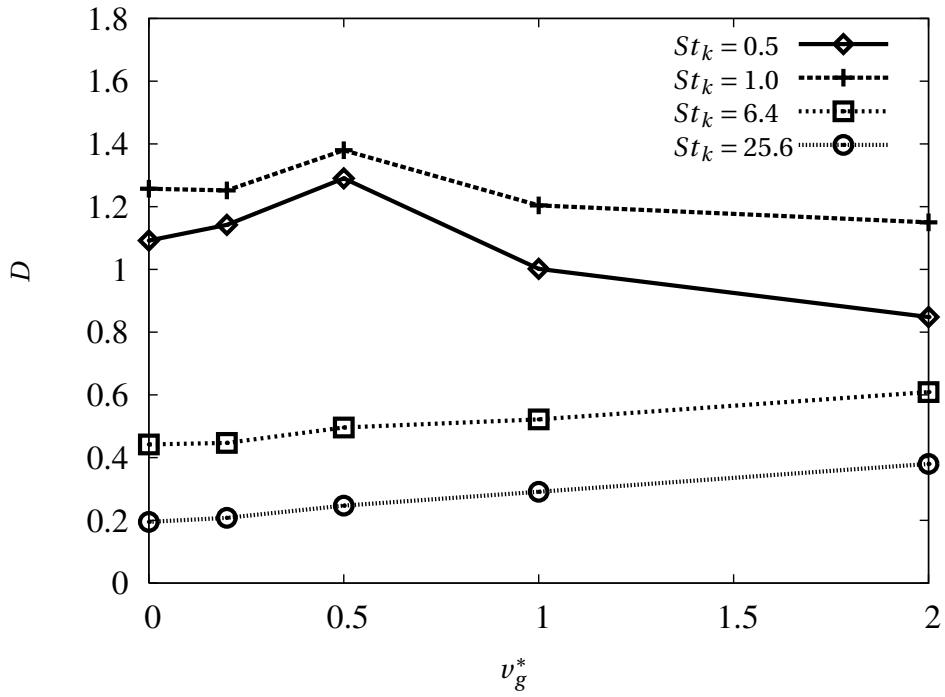

Figure 3.27: Variation of D measure with non-dimensional gravitational settling velocity at different Stokes numbers for $Re_\lambda = 24.2$.

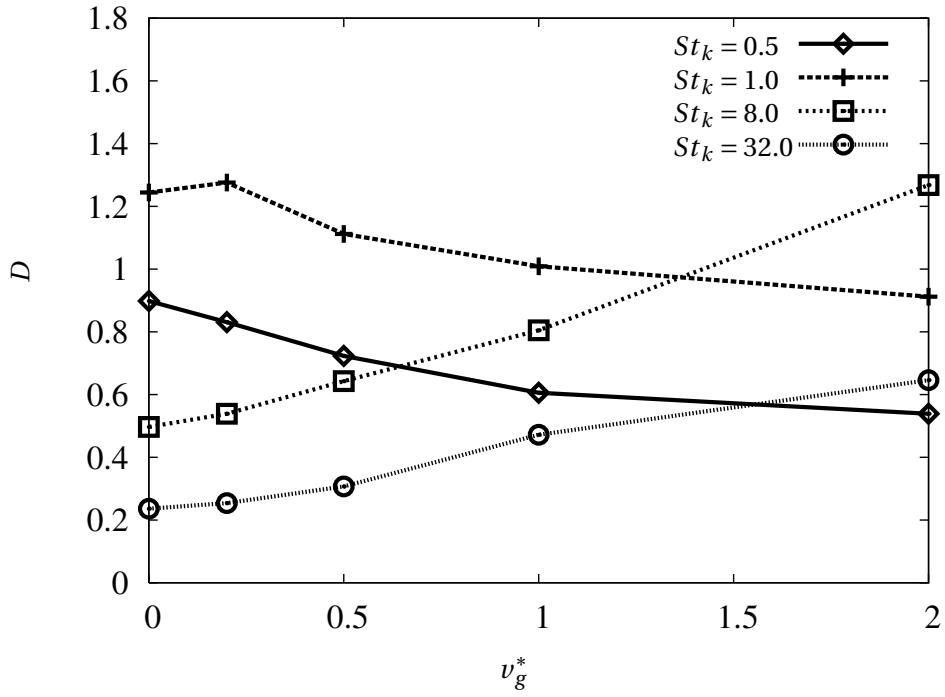

Figure 3.28: Variation of D measure with non-dimensional gravitational settling velocity at different Stokes numbers for $Re_\lambda = 45.0$.

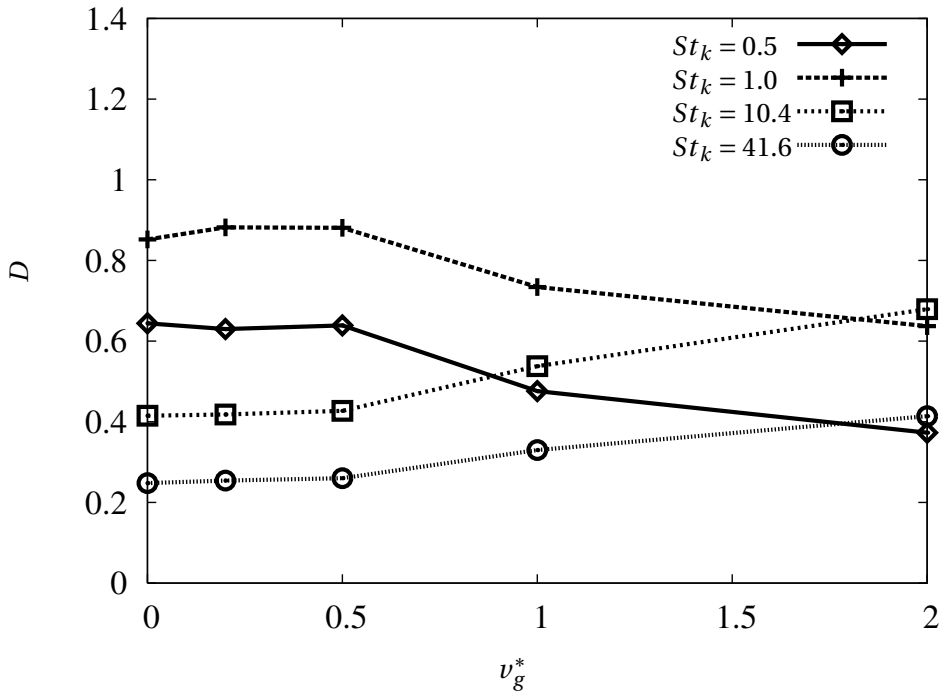

Figure 3.29: Variation of D measure with non-dimensional gravitational settling velocity at different Stokes numbers for $Re_\lambda = 80.6$.

The effect of introducing a gravitational force on D is seen in Figure 3.27 for $Re_\lambda = 24.2$. It is observed that at smaller Stokes numbers, gravity tends to promote accumulation for v_g^* up to around 0.5 and then attenuates accumulation. On the other hand, at large Stokes numbers, gravity tends to promote accumulation monotonically. The effect of gravity on increasing the particle separations up to 10η is weaker than the effect of charge. Increasing the gravitational settling velocity tends to arrange particles in elongated sheets along the direction of gravity. Low Stokes number particles respond to the Kolmogorov size eddies and thus the peaks observed in D measures for $St_k = 1.0$ correspond to settling velocities being nearly the same as Kolmogorov velocity scale. High Stokes number particles which are initially randomly distributed tend to show inhomogeneity in distribution due to arrangement in vertical sheets with increasing gravity effect. It is also useful to investigate the trend of variation of D measure with increasing gravity at higher Reynolds numbers. The results at higher Reynolds numbers (Figures 3.28, 3.29) confirm the trend observed in Figure 3.27. At the higher Reynolds numbers, there seems to be a more pronounced trend towards attenuation of accumulation at low Stokes numbers with increasing v_g^*.

The dependence of the RDF on gravity is demonstrated in Figures 3.30 and 3.31 for low and high

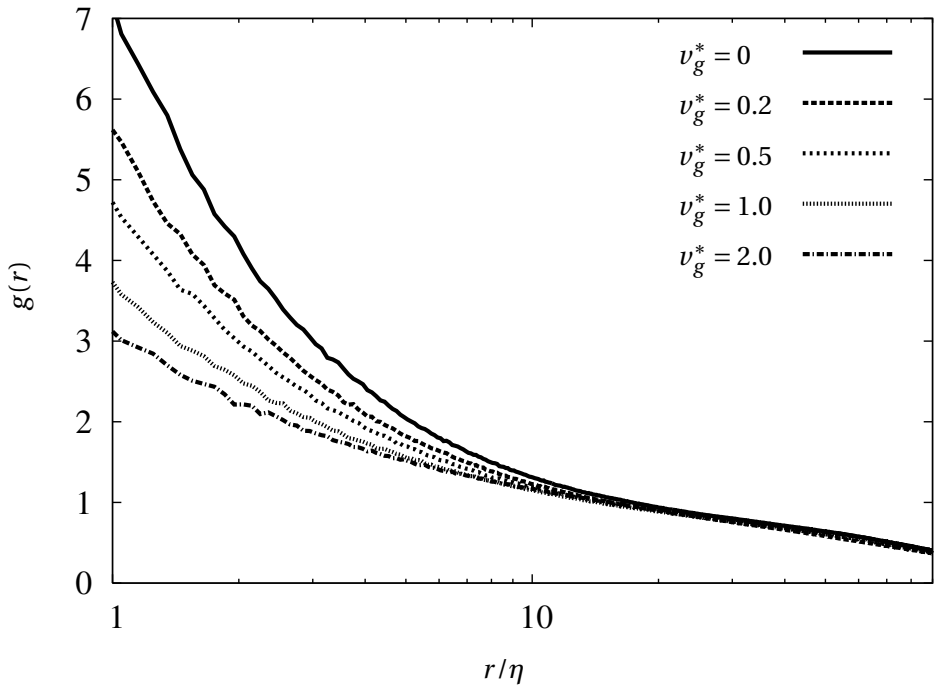

Figure 3.30: Radial distribution functions at different non-dimensional settling velocities for $Re_\lambda = 45.0$, $St_k = 0.5$.

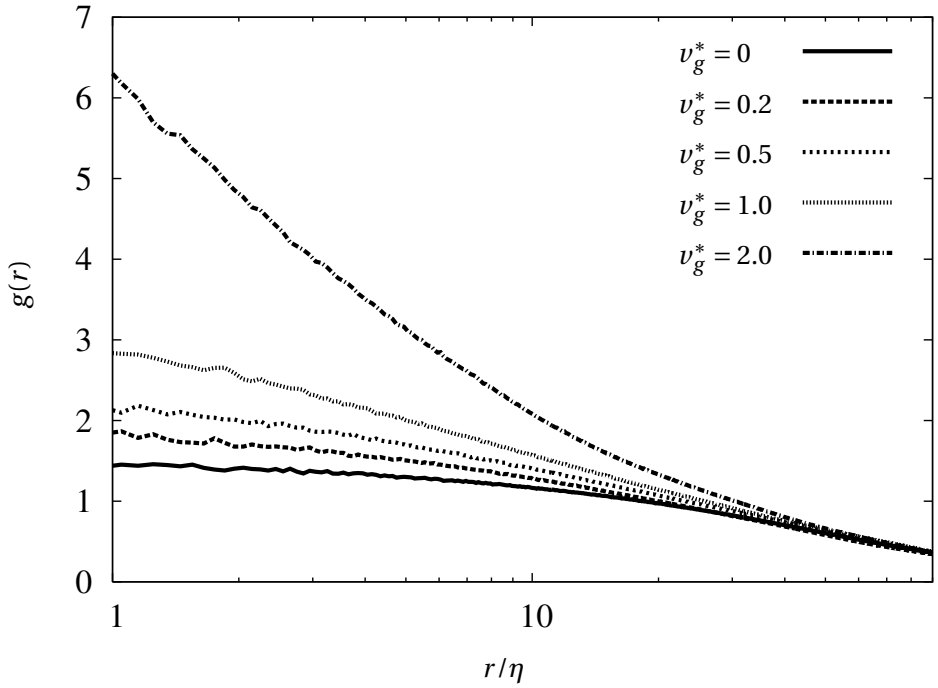

Figure 3.31: Radial distribution functions at different non-dimensional settling velocities for $Re_\lambda = 45.0$, $St_k = 8.0$.

Stokes numbers respectively at one of the Reynolds numbers investigated in this study. The same trend has been observed at other Reynolds numbers used in the study. The reduction in RDF for $St_k = 1.0$ particles with increasing v_g^* is evident from figure 3.32. Recent studies by Shaw et al. [9] attribute the reduction in RDF to the more even sampling of strain and rotational regions of fluid flow by inertial particles in the presence of gravity. It is seen from the present results that the effect of gravity on RDF is felt up to 10η particle separations.

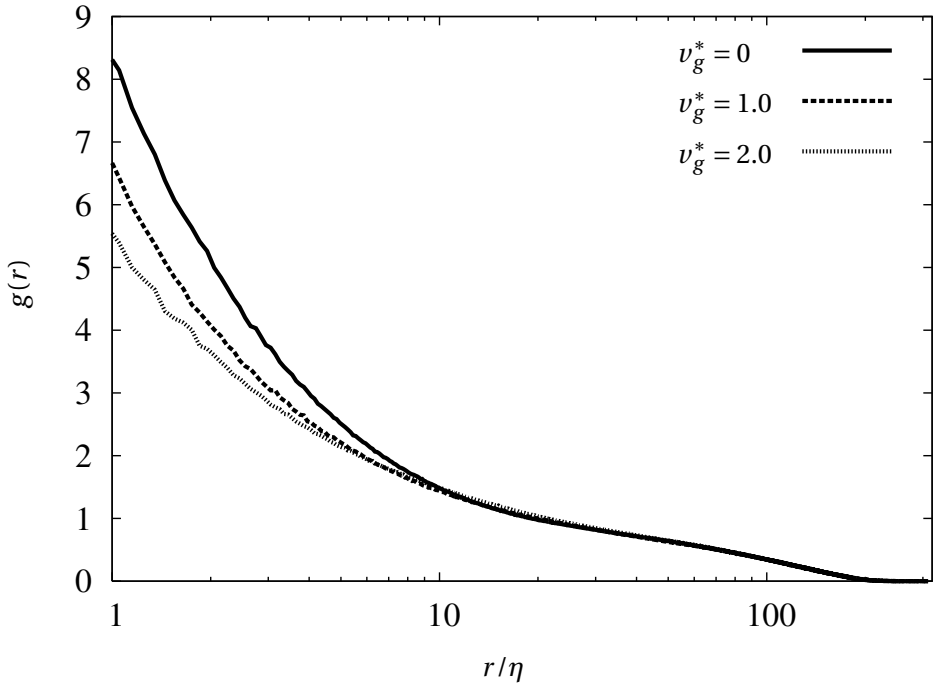

Figure 3.32: Radial distribution functions ($r/\eta > 1.0$) at different non-dimensional gravitational settling velocities for $Re_\lambda = 45.0, St_k = 1.0$.

The findings from simulations including and excluding the gravitational settling force are summarised in section 3.7.

3.7 Summary

In the present work, the phenomenon of preferential concentration has been examined over a wider range of Stokes numbers than in previous studies. The scaling of different measures with Reynolds number has been investigated to gain insight about clustering at high Reynolds num-

bers. This enhanced understanding would help in examining clustering at high Reynolds numbers such as those involved in rain formation in cumulus clouds. The findings from the investigations carried out in this chapter can be summarised as follows:

- The sizes of particle clusters in accumulated condition have been estimated by doing a systematic analysis of the bin-size dependence of the D measure (figures 3.5 to 3.8). The cluster sizes are estimated to be 2.1η, 4.7η, 7.4η and 18.2η for $Re_\lambda = 24.2$, $Re_\lambda = 45.0$, $Re_\lambda = 80.6$ and $Re_\lambda = 136.0$ respectively. It is observed that for a given Reynolds number, the range of sizes of particle clusters increases with Stokes number. At $St_k \approx 1.0$, a sharp peak is observed for the D measure, indicating that the particle number density field is composed predominantly of clusters of a single length scale. On the other hand, at higher Stokes numbers, there is an even distribution of clusters of all sizes.

- The scaling of the D measure with Reynolds number (figure 3.9), which has not been reported in previous studies, is presented in this work. At low Stokes numbers, it is observed that the peak D measure is reduced with increasing Reynolds numbers. This implies that though particles continue to cluster at high Reynolds numbers, the particle distribution is not dominated by clusters of a particular length scale, as is the case at lower Reynolds numbers.

- Using the clustering length scale, l_n, it is observed that the distance between clusters goes up in the accumulated condition (figure 3.12).

- Using the radial distribution function (RDF), it is observed that there is enormous clustering at Kolmogorov scales (figures 3.13 to 3.15).

- While the D measure showed a reduction with Reynolds number, the RDF evaluated at Kolmogorov scale separations increased with Reynolds number (figure 3.16). This is interpreted as follows. At high Reynolds numbers, the clustering is influenced not only by Kolmogorov scale eddies but also by eddy sizes much greater than the Kolmogorov length scale. Thus at high Reynolds numbers, the particle distribution is not dominated by clusters of a single length scale. However the Kolmogorov scale eddies are more intense at high Reynolds numbers and the clustering at that length scale is weakly enhanced as Reynolds number in-

creases. The correlation dimension, D_2, which characterises the structure of a particle cluster, is observed to be independent of Reynolds number (figure 3.17), thus implying that the fractal geometry of individual clusters remains the same irrespective of Reynolds number. It is argued that the RDF and correlation dimension probe the particle-to-particle spacing but do not contain information about size or spacing of particle clusters.

- In addition to studying clustering at zero gravity levels, simulations were also performed incorporating the effect of a gravitational settling force on the particles. In the present work, the gravitational settling force has been characterised by the non-dimensional settling velocity v_g^* defined using the RMS turbulence intensity as the reference velocity scale. It is seen that the settling force corresponding to $v_g^* = 1$ causes significant reduction in dispersion (figure 3.23). The low Stokes number particles, which are preferentially accumulated in the absence of a settling force, tend to be distributed more homogeneously in the presence of a settling force. On the other hand, the high Stokes number particles tend to be arranged in sheets in the direction of gravity resulting in an increase in values of the indicators of accumulation.

Chapter 4

Charged particle simulations

In the previous chapter it has been observed that under certain conditions, inertial particles which are initially homogeneously distributed, tend to get de-mixed by the action of turbulent eddies. This is particularly undesirable when the particles are treated as akin to fuel droplets in the combustion process. Accumulation of droplets in vortex structures is problematic since it leads to non-uniform fuel-air mixtures. This in turn leads to fuel rich and lean regions further leading to inefficient combustion and production of unwanted emissions. Electrical charging of fuel droplets has been experimentally demonstrated in previous studies to mitigate this problem. Electrically charged particles are also found in clouds and the charging combined with gravitational settling is thought to play an important role in clustering of droplets leading to rain initiation. Besides electrosprays and clouds, dispersion of electrically charged particles is an important process in colloids, dusty plasmas and protoplanetary nebulae. In this chapter, electrically charging of particles as a means of controlling preferential accumulation has been explored. Using DNS of charged particles, it has been demonstrated in the present work that charging of particles results in a repulsive Lorentz force which acts to diffuse particle clusters. The length scale at which the Lorentz force would be active depends on the total amount of charge present in the domain. A non-dimensional Coulomb terminal velocity has been defined to quantify the bulk charge density and charge levels required to mitigate accumulation both in the presence and absence of gravity. It is found that preferential accumulation is mitigated at bulk charge density levels that are practically relevant and commensurate with the first few centimeters of the spray plume in charged injection atom-

izers, the region where non-homogeneous particle concentration typically forms. Investigation of the combined effect of Lorentz force and gravitational settling force makes the present work comparable to experimental observations and potentially useful to practical applications, particularly to spray combustion applications.

Another interesting aspect is to note that even in the presence of charge on particles, a uniform distribution of particles would lead to a null electric field and thus no net Lorentz force on the particles. The Lorentz force is switched "on" only when the charged particles are non-homogeneously distributed. Inhomogeneous distribution of charged particles leads to generation of an electric field due to the non-homogeneous Eulerian charge density distribution. Combined with the observation of stationary statistics presented in the previous chapter, this situation lends itself to the following interesting questions - "Do charged particle simulations lead to a stationary particle concentration field?". And if so, "How does the stationary magnitude of preferential concentration, for a given Coulomb velocity, compare with the uncharged case ?" The attempt to answer these questions is the underlying motivation for this particular study.

4.1 Aims and Objectives

In the present study, the dependence of particle accumulation on turbulent fluctuations, particle inertia, gravity and bulk charge density has been systematically investigated. The fluid turbulence is characterised by its Taylor Reynolds number, Re_λ (introduced in section 2.4.1). The particle inertia and settling velocity are characterised by the non-dimensional parameters, St_k and v_g^* (introduced in section 2.4.2) respectively. The bulk charge density in the domain is characterised by defining a non-dimensional Coulomb velocity, v_c^* (introduced in section 4.3). Initially, the stationarity of particle distributions in the presence of Lorentz force is investigated by looking at several indicators outlined in section 3.2.

Here the attempt is to build both a qualitative and quantitative picture of the effect of an electric field on particle dispersion. The sequence of events is expected to be as follows. Initially the particles would be randomly distributed leading to a null electric field. The particles under certain conditions (as discussed in the previous chapter) would tend to be inhomogeneously distributed

under the action of turbulent eddies. This would lead to creation of a net electric field, the strength of which will depend both on bulk charge density level in the domain and the degree of inhomogeneity. For a sufficient bulk charge density level, the Lorentz force on the particles would be just sufficient to overcome the centrifugal force due to the action of turbulent eddies. Thus the particle distribution would tend to be restored to its original random configuration. However the reduced non-uniformity of particle distribution would be accompanied by commensurate weakening of the Lorentz force. Thus it is not clear *a priori* whether the particle distribution would attain a stationary state in the charged case. It has been observed in the previous chapter that indicators of "preferential concentration" imply a stationary state for the uncharged case. Also, this study aims to estimate the bulk charge density level required to substantially destroy the preferential concentration effect.The results presented in this chapter are limited to one-way coupling, neglecting the influence of particles on the fluid turbulence.

4.2 Background

It has been demonstrated in the previous chapter that particles tend to be distributed inhomogeneously under certain conditions. The practical applications where preferential accumulation might play a significant role range from coal fired combustors to electrostatic precipitators. This de-mixing of particles/droplets is undesirable in situations like fuel sprays, where de-mixing leads to enhanced soot formation. In spray combustion applications, typically once the liquid primary atomization process has completed, the only means to modify the drop trajectory is via the fluid mean and fluctuating flow fields. Given the possibility of de-mixing of particle population due to interaction with dissipation scales of fluctuating velocity, this represents a problematic situation. This rules out using the fluid velocity field to obtain uniform particle concentration. Ideally, the situation demands a responsive body force which switches itself 'on' once the particle distribution becomes non-uniform. In this chapter, we evaluate the viability of using Lorentz force to destroy the accumulation effect.

Bellan and Harstad [62] added to our understanding of combustion and evaporation of liquid droplets by modeling droplet evaporation in clusters of droplets. Bellan and Harstad [62] reported

that for a dense cluster of droplets, turbulence enhances evaporation and can lead to reduced evaporation times. Understanding mixing of fuel droplets in a turbulent gas phase is thus important for combustion applications. A further step is to attempt to control the homogeneity of the air-fuel mixture. Charging of droplets has already been proposed as a means to improve diluteness of sprays. Bellan [63] developed a model to demonstrate feasibility of charging fuel sprays in diesel engines. It was argued that a dilute spray would lead to lower soot formation and thus reduction in pollutant emissions. The work presented in this chapter lends evidence to the mitigation of clustering of particles by placing charges on them.

Charged injection atomizers are capable of generating electrically charged sprays of insulating hydrocarbon liquids and have been developed and refined. Electrically charged sprays offer several benefits such as lack of droplet agglomeration and control of the droplet size distribution and spray plume shape. Addition of electric charge leads to breakup of the jet by overcoming the balancing force due to surface tension. This leads to smaller mean diameters of the droplets and furthermore larger spray cone angles due to electrical repulsion between them. Numerous experimental studies have been carried out to study the operational characteristics of these atomizers. Details of spray characteristics of charge injection atomizers can be obtained from Rigit and Shrimpton [64]. Shrimpton and Yule [65] found a radial stratification of mean droplet diameter that evolved as the spray moved downstream. They found that the smaller droplets are more likely to be repelled away from the core region, where the radial electric field component, due to spray specific charge, was most intense. They reported that larger droplets were more likely to be found near the spray center line since they had typically much more inertia.

Very few studies have addressed the clustering of charged particles. Alipchenkov et al. [66] have suggested a statistical model to explain clustering of charged particles in isotropic turbulence. Lu et al. [8] reported measurements of clustering of charged particles in isotropic turbulence. In the previous chapter, we have observed that the RDF increases significantly at Kolmogorov scales for uncharged particles. This power-law behavior has been explained by Chun et al. [53] (equation 3.15). The experimental measurements of Lu et al. [8] clearly demonstrate that this power-law growth of the RDF is suppressed by the charging of particles. The charging introduces a length scale below which clustering of particles in suppressed. They also extended the theoretical frame-

work developed by Chun et al. [53] to include the "drift" due to Coulomb repulsion force between pair of particles. The functional form of the RDF for charged particles as derived by Lu et al. [8] results from a balance between the outward drift due to Coulomb repulsion and inward drift due to inertia and is as follows

$$g(r) = c_0\left(\frac{\eta}{r}\right)^{c_1} \exp\left[-c_2 St_k\left(\frac{E_{\text{charge}}}{E_{\text{turb}}}\right)\left(\frac{\eta}{r}\right)^3\right], \tag{4.1}$$

$$c_2 = \frac{2}{3B_{nl}}, \tag{4.2}$$

where B_{nl} is the dimensionless non-local coefficient for turbulent diffusivity. E_{charge} and E_{turb} are the energy of the Coulomb interaction at Kolmogorov scale and energy of the Kolmogorov eddies respectively, such that

$$E_{\text{charge}} = \frac{N_s q_p^2}{4\pi\epsilon_0 m_p \eta}, \tag{4.3}$$

$$E_{\text{turb}} = \left(\frac{\eta}{\tau_k}\right)^2, \tag{4.4}$$

where N_s is the number of real particles represented by a computational charged particle and q_p and m_p are the particle charge and mass respectively. Lu et al. [8] found that their measurements matched closely with the functional form of the RDF derived by them thus providing credence to the drift-diffusion description of inertial particle accumulation.

Shaw et al. [9] have extended the functional form of the RDF suggested by Lu et al. [8] to account for gravitational settling of charged particles. Gravity affects both the uncharged and charged term in the function of the RDF in a nontrivial way. They measured RDFs for water droplets in homogeneous, isotropic air turbulence. In the present work, the results obtained from numerical simulations have been compared with the experimental results presented in Shaw et al. [9].

4.3 Simulation parameters

In the previous chapter, the effect of adding a gravitational settling force in the particle equation of motion was systematically investigated. On similar lines, the effect of adding the Lorentz force on the particles is explored in this chapter. The relative magnitude of the electric field has been

characterised by defining a Coulomb velocity as follows,

$$v_c = \tau_p \frac{E_{\text{rms}} q_p}{m_p}, \tag{4.5}$$

where E_{rms} is the RMS magnitude of electric field in the domain, q_p is the charge on a single particle and m_p is the mass of a particle. Effectively, the Coulomb velocity represents the terminal velocity that a particle would attain due to the influence of a specified electric field. The corresponding non-dimensional parameter of interest is the Coulomb velocity normalised by the RMS turbulence velocity, u', defined as follows,

$$v_c^* = \frac{v_c}{u'}. \tag{4.6}$$

In this chapter, results are reported from a set of monosized particle simulations over a range of Taylor Reynolds numbers, Stokes numbers and non-dimensional Coulomb velocities. The effect of each of these parameters is systematically studied. The Taylor Reynolds numbers reported in this work are 24.2, 45.0 and 80.6. The Stokes numbers simulated in this study range from $0.5-42$ based on the Kolmogorov time scale of the fluid. The non-dimensional Coulomb velocities span from $0-2.5$. The non-dimensional Coulomb velocity is varied by controlling the total amount of charge present in the domain. Increasing the bulk charge density (charge per unit volume) in the domain leads to increase in the non-dimensional Coulomb velocities. Preferential accumulation has been quantified using the same measures as used in chapter 3. For all the simulations, 10^5 computational particles are tracked through the domain. The density of all the particles is 1000 kg/m^3. Each of the particles carries a certain amount of charge, q_p, which is a fraction of the Rayleigh limit for a droplet of a given size. The Rayleigh number (ratio of actual charge to the Rayleigh limit) for all the simulations is 0.8. Recall that the Rayleigh limit is given by,

$$Q_R = 8\pi\sqrt{\gamma\epsilon_0 r_d^3}. \tag{4.7}$$

The surface tension coefficient, γ used for all simulations is 0.05. The permittivity of free space, $\epsilon_0 = 8.854\times10^{-12}$. Table 4.1 lists the particle Stokes numbers and corresponding diameters d_p and

charges q_p for the $Re_\lambda = 24.2, 45.0$ and 80.6 charged particle simulations. For each combination of Reynolds number and Stokes number, the Coulomb velocity is varied to study the effect of strength of electric field on the particle distribution. It should be noted that the computational particles are stochastic in nature and represent an aggregate of N_s *real* particles. The value of N_s is adjusted to obtain the required Coulomb velocity in the domain. The different N_s values for all the simulations are also listed in Table 4.1.

Re_λ	St_k	d_p mm	$q_p \times 10^9$ Coulombs	N_s	ϕ_v	d_p/η
	0.5	7.2	2.89	85.8	7.86×10^{-5}	0.09
	1.0	10.2	4.86	51.0	2.22×10^{-4}	0.13
24.2	1.6	12.9	6.92	35.8	4.53×10^{-4}	0.17
	6.4	25.8	19.58	12.7	3.63×10^{-3}	0.34
	12.8	36.4	32.93	7.5	1.02×10^{-2}	0.48
	25.6	51.6	55.38	4.5	2.89×10^{-2}	0.68
	0.5	3.3	0.91	268.4	7.56×10^{-5}	0.08
	1.0	4.7	1.53	159.6	2.14×10^{-5}	0.12
45.0	2.0	6.6	2.52	94.9	6.07×10^{-5}	0.17
	8.0	13.2	7.13	33.6	4.85×10^{-4}	0.33
	16.0	18.6	12.0	20.0	1.36×10^{-3}	0.47
	32.0	26.3	20.18	11.9	3.84×10^{-3}	0.66
	0.5	1.7	0.34	900.3	9.44×10^{-7}	0.09
	1.0	2.5	0.59	535.5	2.67×10^{-6}	0.13
80.6	2.6	3.8	1.11	261.4	1.15×10^{-5}	0.21
	10.4	7.6	3.13	92.4	9.16×10^{-5}	0.42
	20.8	10.7	5.23	55.0	2.59×10^{-4}	0.59
	41.6	15.1	8.78	32.7	7.33×10^{-4}	0.84

Table 4.1: Particle diameters, charges, number of stochastic particles represented by a *computational* particle and volume fractions at different Reynolds and Stokes numbers for charged particle simulations

4.4 Results and discussion

The effect of adding a uniform electric charge on the particles is considered in this section. It is interesting to note that the particle distribution reaches a statistically steady state even in the presence of electric charge.

Initially, it is verified that the results obtained are independent of the initial distribution of par-

ticles. In all the simulations, particles are initially randomly distributed throughout the domain. Tests have been performed comparing the particle statistics obtained from both random and uniform initial distributions. For the uniform distribution, the particles are initialised at the discrete grid points where fluid velocity field is evaluated in physical space. It is observed from figure 4.1 that the D measures of preferential accumulation are independent of the initial particle distribution at $Re_\lambda = 45.0$. Similar agreement has been observed for other indicators of accumulation at the other Reynolds numbers reported in the present study.

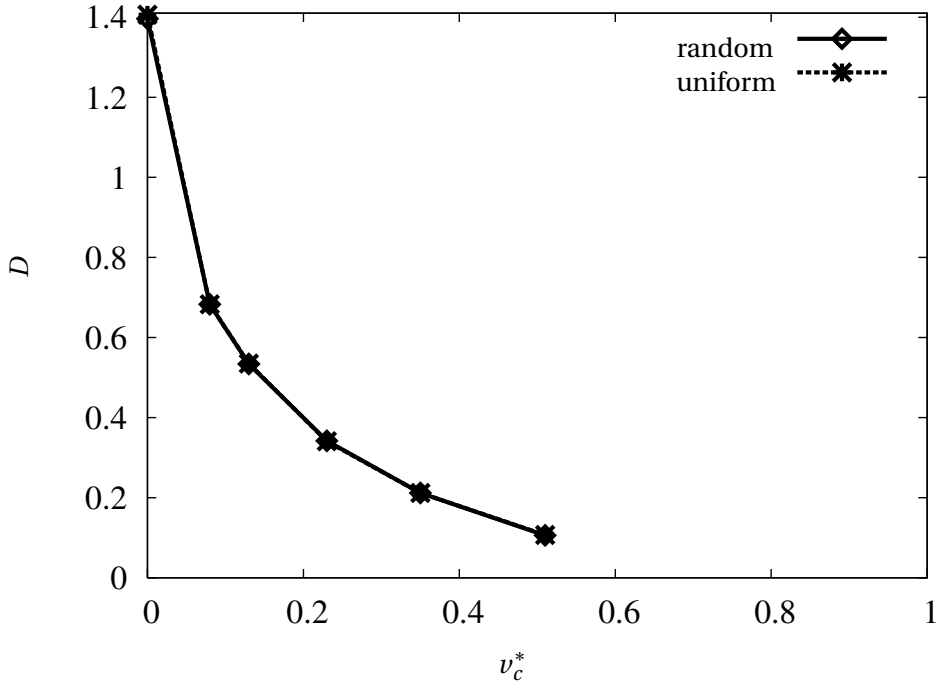

Figure 4.1: Variation of D measure with non-dimensional Coulomb velocity for both random and uniform initial particle distributions at $Re_\lambda = 45.0$. The number of particles used in both simulations is 262144 (=64^3).

Figure 4.2 shows the temporal variations of the D measure (bin-size, $h/\eta = 4.4$) of accumulation. The variance of the fluctuations in D measure is quite significant for the Coulomb velocity shown in the figure. It is observed (not shown here) that as the Coulomb velocity increases, the variance of the fluctuations goes down.

The effect of putting charge on particles is evident from Figures 4.3 and 4.4. The accumulation of particles is evident in Figure 4.3, which shows the particle distribution in absence of any electric field. Figure 4.4 on the other hand shows a random distribution of particles at $v_c^* = 0.62$ for the same fluid realisation at the same instant.

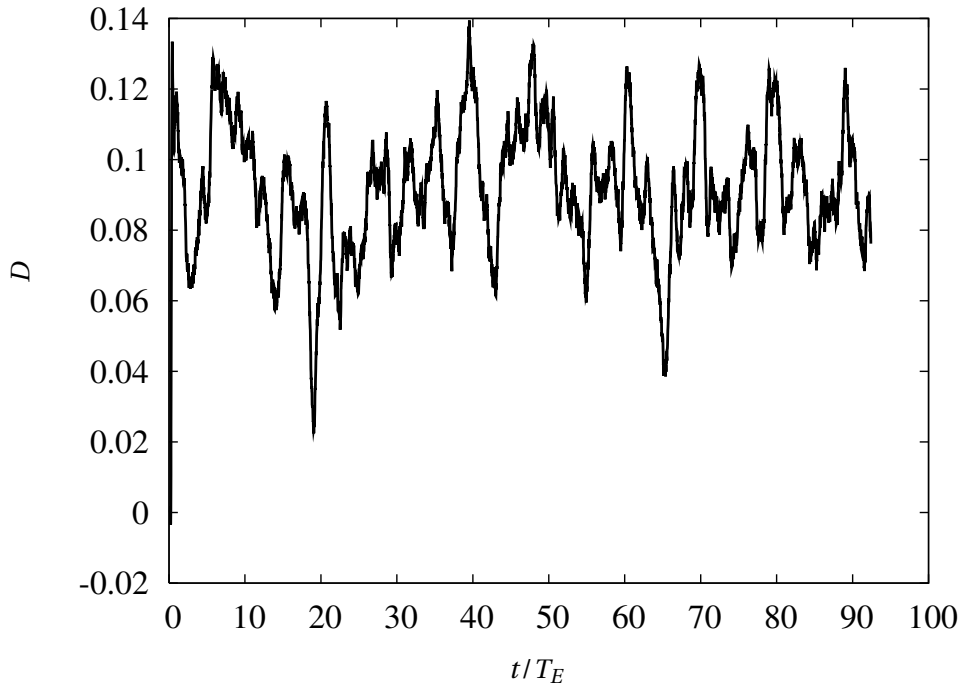

Figure 4.2: Time history of D measure for $Re_\lambda = 24.2$, $St_k = 1.0$ and $v_c^* = 0.62$

.

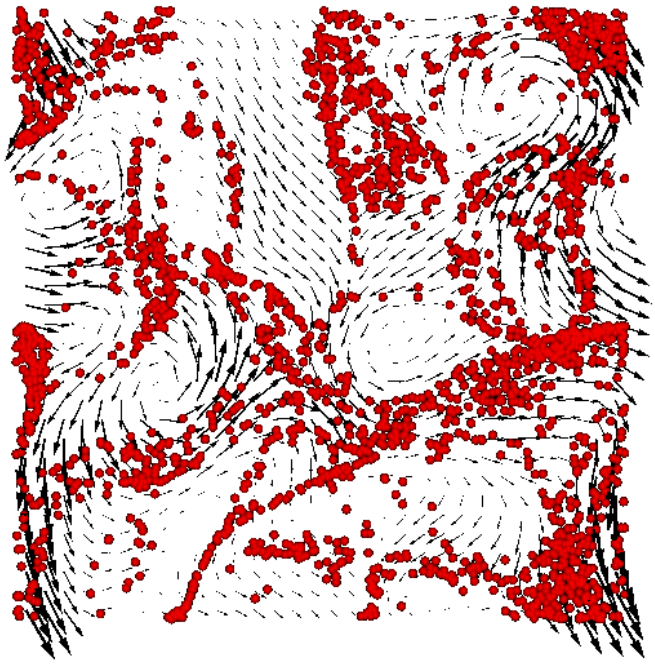

Figure 4.3: Particle positions and fluid velocity vectors for $Re_\lambda = 24.2$, $St_k = 1.0$ and no charge on particles.

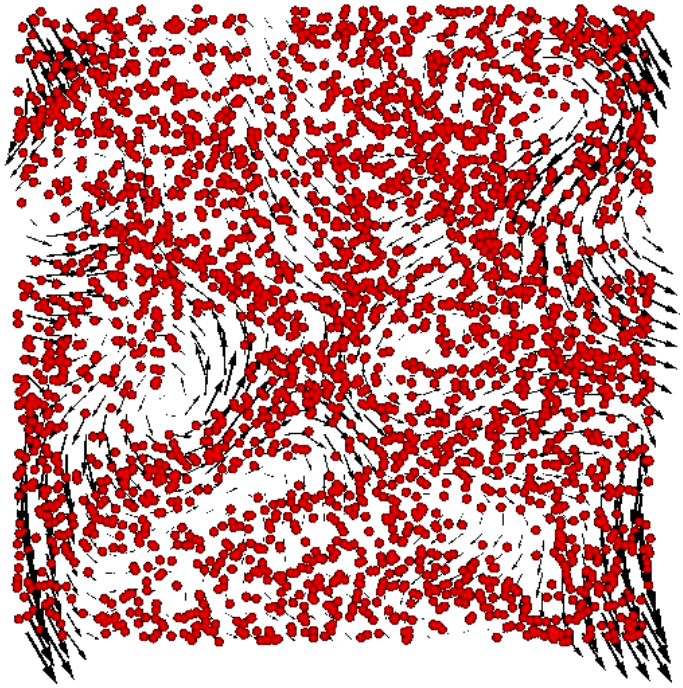

Figure 4.4: Particle positions and fluid velocity vectors for Re_λ = 24.2, St_k = 1.0 and non-dimensional Coulomb velocity, $v_c^* = 0.62$.

The effect of the strength of the electrostatic field is further illustrated by Figures 4.5 and 4.6, which show the particle positions and fluid velocity vectors for the same fluid realisations but different Coulomb velocity levels. It is evident that particle accumulation is greater for lower Coulomb velocity level.

Figures 4.7 and 4.8 show the electric field vectors and particle positions for both low and high Coulomb velocity levels. In the case of low charge density, it is seen that the electric field direction points to the center of the voids in the distribution. The tendency of the Lorentz force is to direct the particles to regions of low number density. At high Coulomb velocities, a nearly homogeneous distribution of particles is observed and thus the electric field vectors are randomly oriented.

High particle concentration regions are regions of higher potential, while the voids represent regions of low potential as seen from Figures 4.9 and 4.10.

It is observed from Figure 4.11 that increasing the Coulomb velocity leads to reduction in accumulation. It is observed that Coulomb velocity, $v_c^* \approx 1.0$ is sufficient to regain homogeneous distribution of particles. Higher values of Coulomb velocity correspond to higher Coulomb velocity

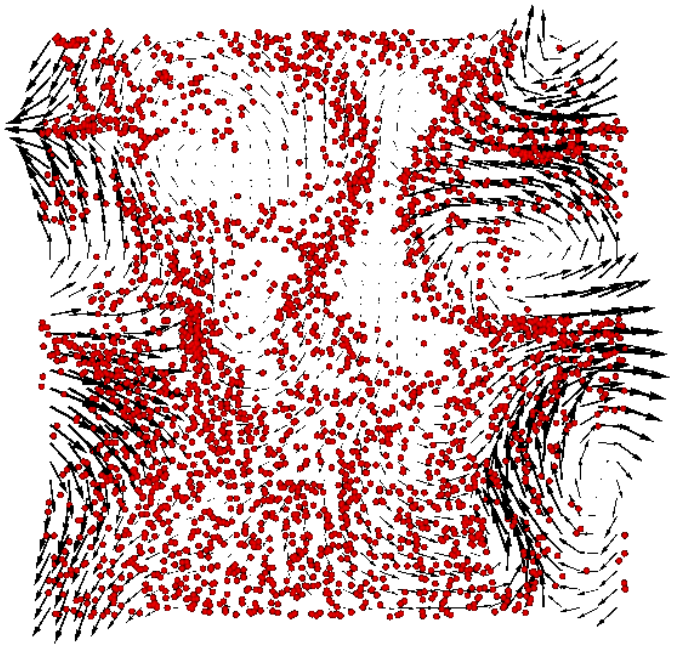

Figure 4.5: Fluid velocity vectors and particle positions for $Re_\lambda = 24.2$, $St_k = 1.0$ and non-dimensional Coulomb velocity, $v_c^* = 0.27$.

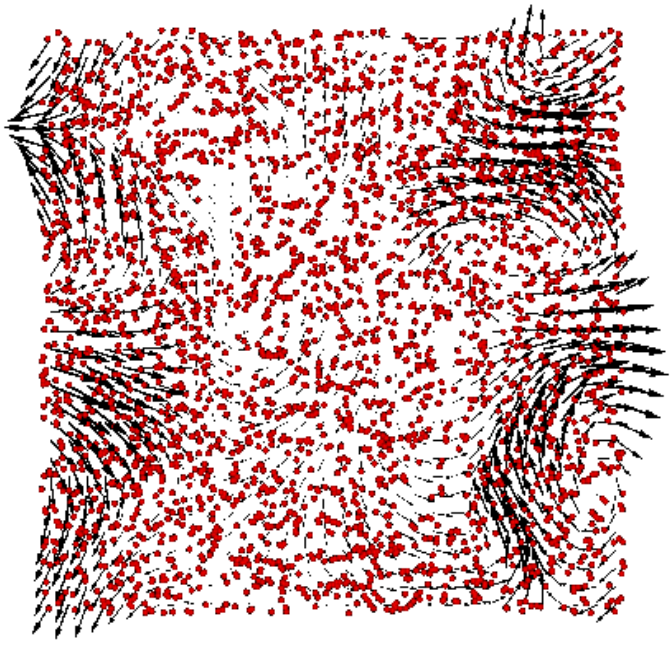

Figure 4.6: Fluid velocity vectors and particle positions for $Re_\lambda = 24.2$, $St_k = 1.0$ and non-dimensional Coulomb velocity, $v_c^* = 1.33$.

level in the domain. Thus increasing the Lorentz force strength causes the particles to reside in relatively high enstrophy areas of the flow. The influence of charge level on $\langle n'e' \rangle$ measure indi-

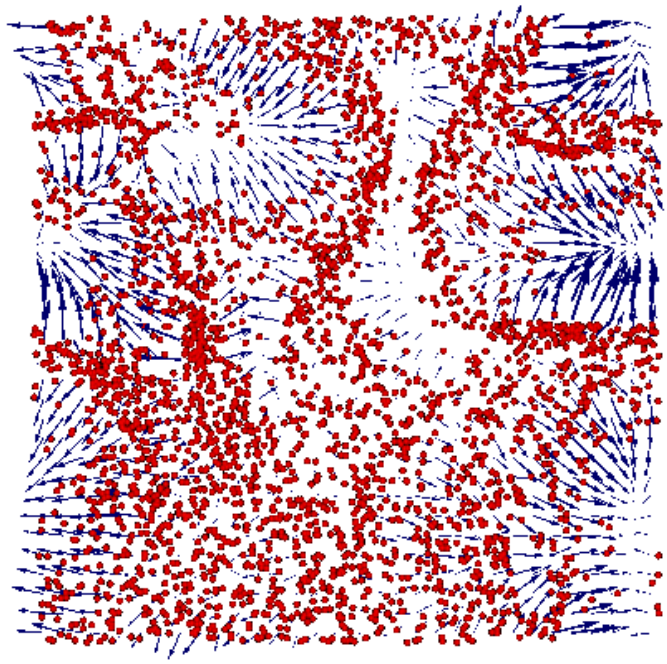

Figure 4.7: Electric field vectors and particle positions for $Re_\lambda = 24.2$, $St_k = 1.0$ and non-dimensional Coulomb velocity, $v_c^* = 0.27$.

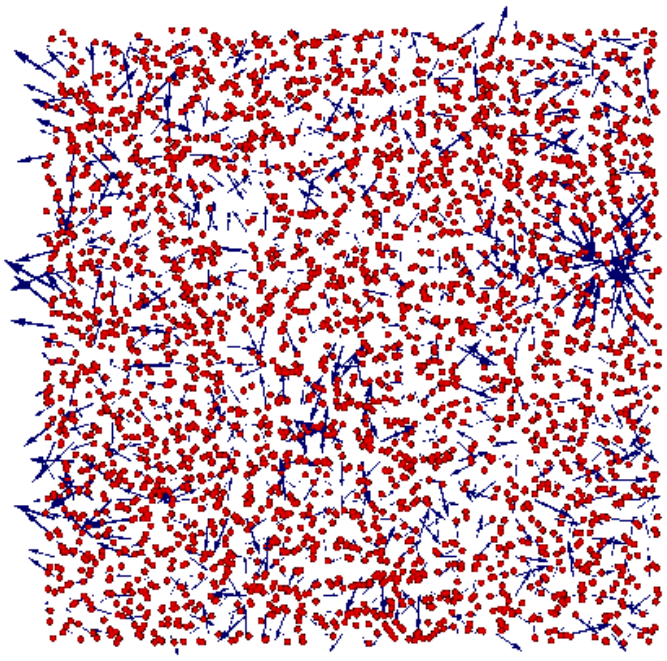

Figure 4.8: Electric field vectors and particle positions for $Re_\lambda = 24.2$, $St_k = 1.0$ and non-dimensional Coulomb velocity, $v_c^* = 1.33$.

cates that the Lorentz force enables the particles to mitigate the centrifugal effects in the core of vortices. Figures 4.12 and 4.13 show the reduction in accumulation with increasing Coulomb ve-

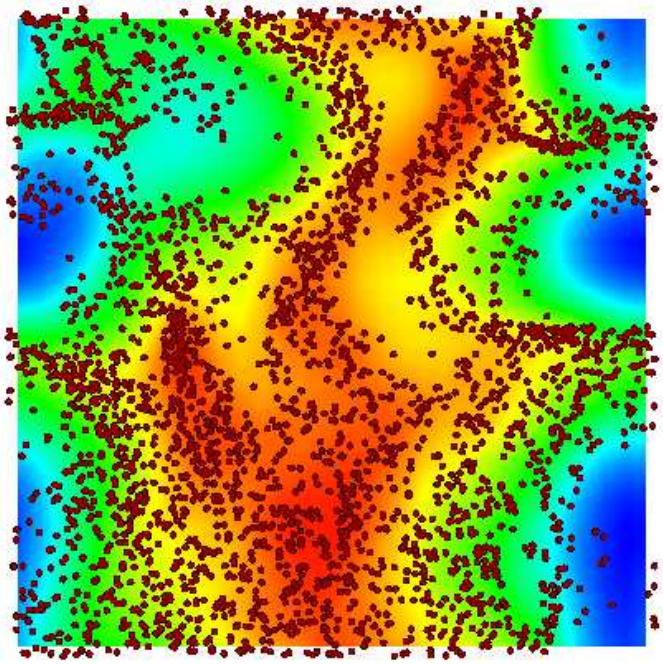

Figure 4.9: Electric potential and particle positions for $Re_\lambda = 24.2$, $St_k = 1.0$ and non-dimensional Coulomb velocity, $v_c^* = 0.27$.

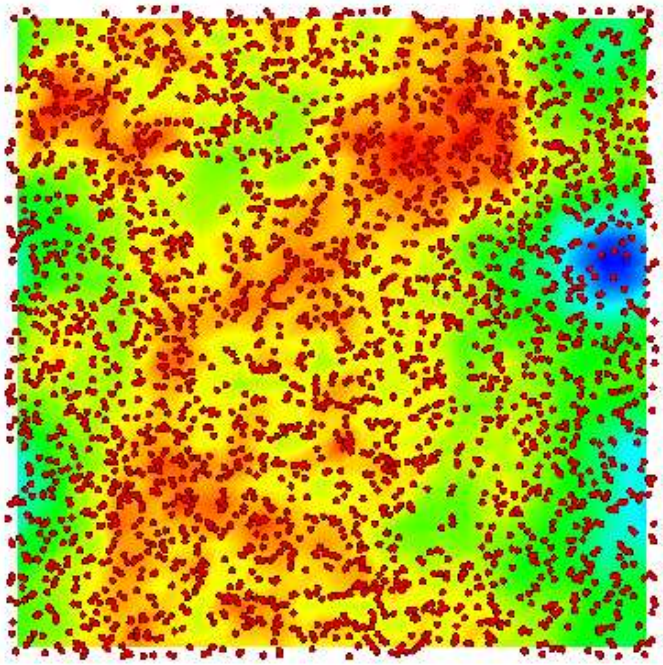

Figure 4.10: Electric potential and particle positions for $Re_\lambda = 24.2$, $St_k = 1.0$ and non-dimensional Coulomb velocity, $v_c^* = 1.33$.

locities for both $Re_\lambda = 45.0$ and $Re_\lambda = 80.6$. The Coulomb velocities investigated in this study are limited but there is a clear trend to reduction in accumulation. It can be extrapolated that $v_c^* \approx 1.0$ would lead to homogenisation of particle distribution.

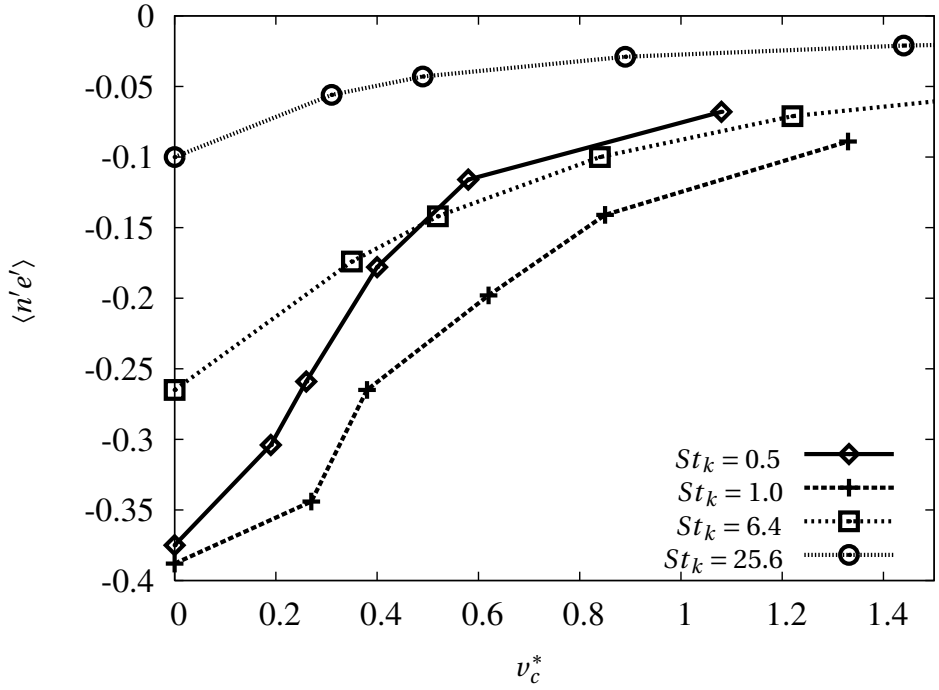

Figure 4.11: Variation of $\langle n'e' \rangle$ with non-dimensional Coulomb velocity at different Stokes numbers for $Re_\lambda = 24.2$.

The reduction in accumulation with increasing Coulomb velocities is also evident from figures 4.14, 4.15, 4.16. The D values shown in these figures are the peak values when evaluated over a range of bin sizes spanning from the sub-Kolmogorov to the integral scales. It is observed that $v_c^* \approx 1.0$ is sufficient to mitigate accumulation. This is clearly evident for the high Stokes number particles. At $Re_\lambda = 45.0, 80.6$, the range of non-dimensional Coulomb velocities investigated is limited for low Stokes number particles and thus conclusions can only be formed on the basis of the trend observed in the figures. The trend shows that $v_c^* \approx 1.0$ would be sufficient to regain a homogenous distribution even at low Stokes numbers. For low Stokes number particles at $Re_\lambda = 24.2$, there is a tendency for particles to cluster at Kolmogorov scales when Coulomb velocity is increased beyond $v_c^* \approx 0.8$.

The radial distribution function is representative of the number of particle pairs at a given separa-

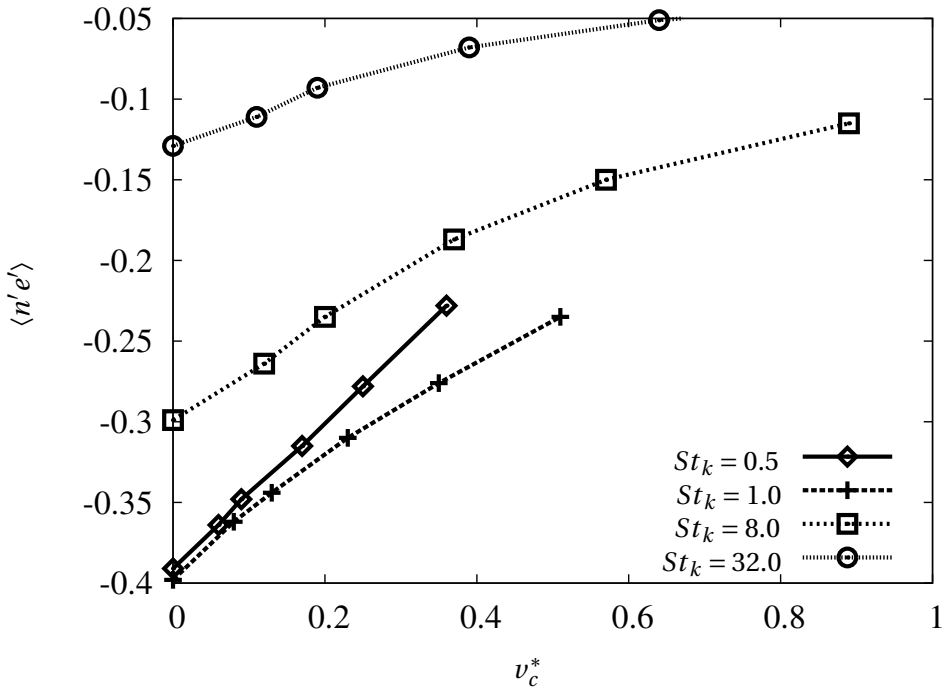

Figure 4.12: Variation of $\langle n'e' \rangle$ with non-dimensional Coulomb velocity at different Stokes numbers for $Re_\lambda = 45.0$.

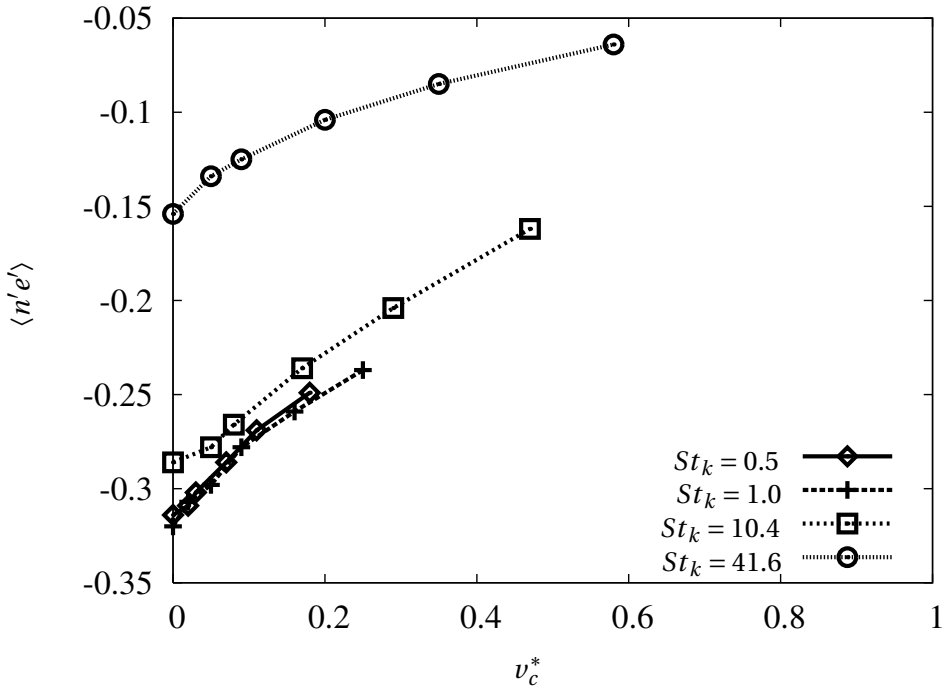

Figure 4.13: Variation of $\langle n'e' \rangle$ with non-dimensional Coulomb velocity at different Stokes numbers for $Re_\lambda = 80.6$.

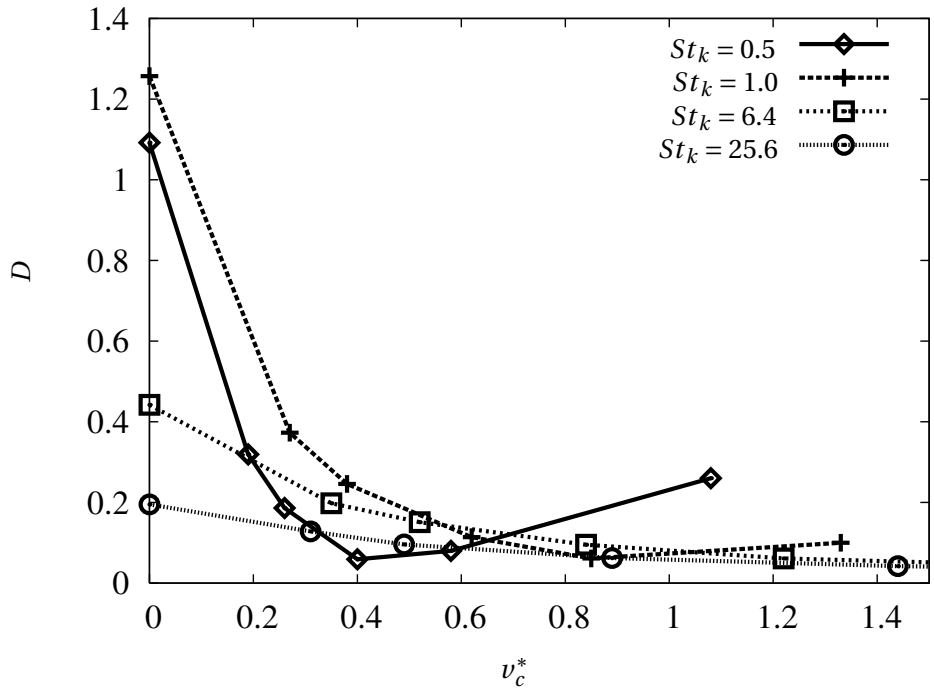

Figure 4.14: Variation of D measure with non-dimensional Coulomb velocity at different Stokes numbers for $Re_\lambda = 24.2$.

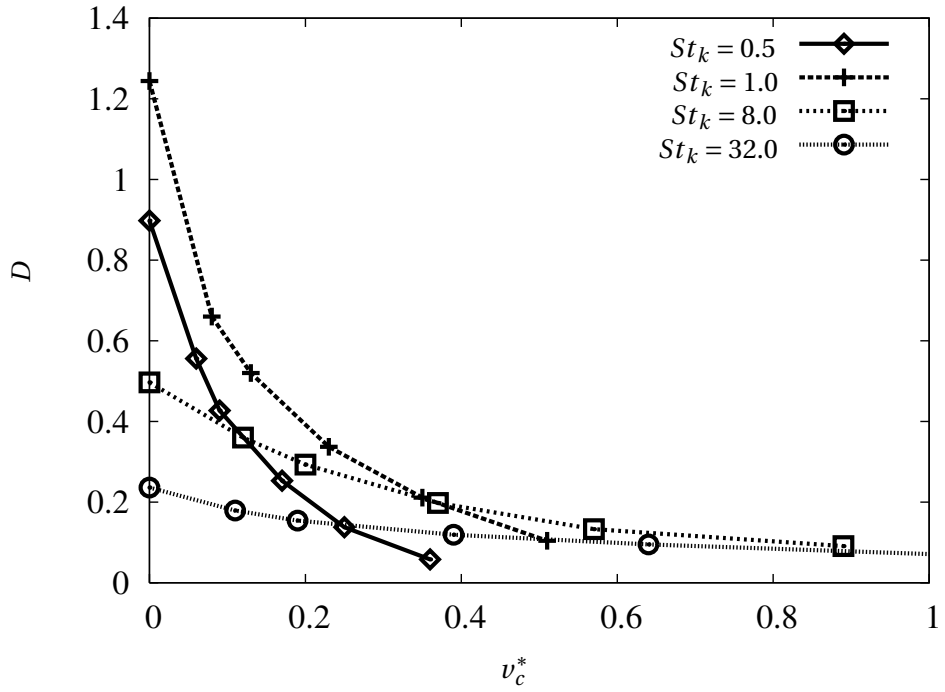

Figure 4.15: Variation of D measure with non-dimensional Coulomb velocity at different Stokes numbers for $Re_\lambda = 45.0$.

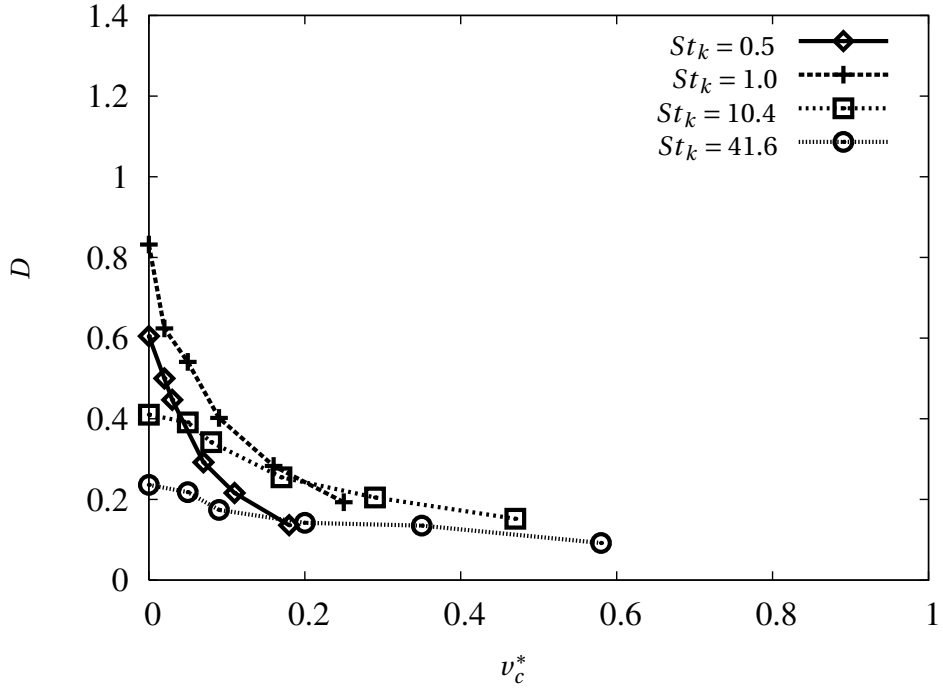

Figure 4.16: Variation of D measure with non-dimensional Coulomb velocity at different Stokes numbers for $Re_\lambda = 80.6$.

tion relative to that in the case of uniform distribution of particles. Qualitatively, the RDF is an indicator of particle-particle spacing in clusters of particles. The effect of increasing electric charge on the radial distribution function is seen in Figures 4.17, 4.18 and 4.19 for different Reynolds numbers. It is observed that the most significant effect of the presence of charge is to reduce the number of pairs with separations up to 10η. The reduced RDF values imply a reduced collision probability[42].

The correlation dimension, D_2, which derives itself from the slope of the RDF also captures the reduction in accumulation, as observed in figure 4.20. Note that increasing D_2 values correspond to a more uniform distribution. This indicates that inclusion of charges on particles not only allows the particles to overcome the centrifugal effects due to turbulent eddies (as evident from reduction in the $\langle n'e' \rangle$ and D measure) but charging also diffuses the particle clusters by increasing particle-particle spacing.

The D_2 values are computed by binning all the particle pairs $\mathrm{np}(r)$ according to their separation distance r, and calculating the slope of the curve $\ln(\mathrm{np}(r))$ versus $\ln(r)$ over the separation range

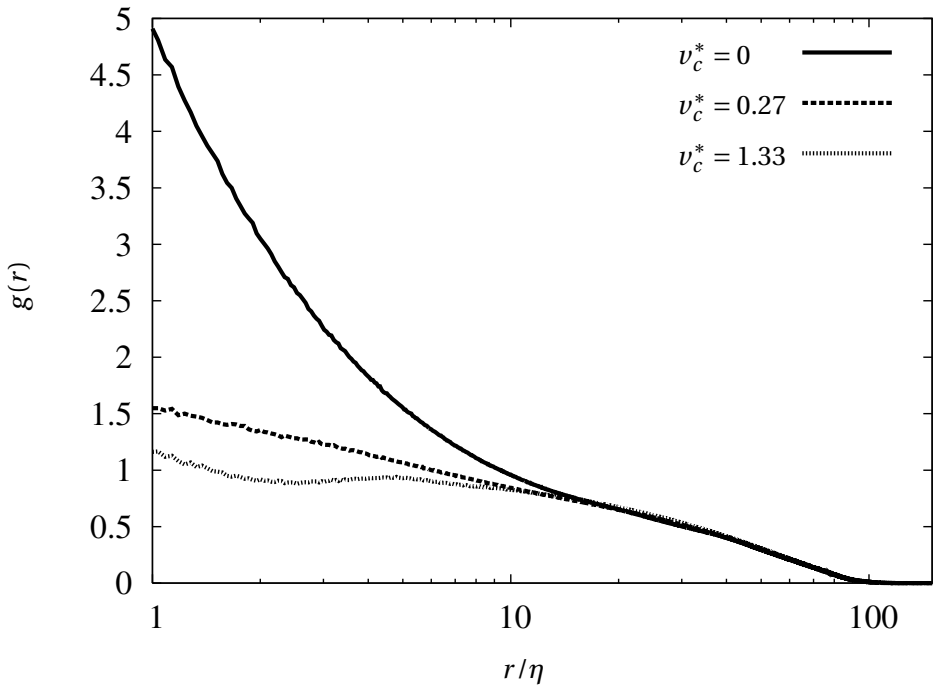

Figure 4.17: Radial distribution functions ($r/\eta > 1.0$) at different non-dimensional Coulomb velocities for $Re_\lambda = 24.2, St_k = 1.0$.

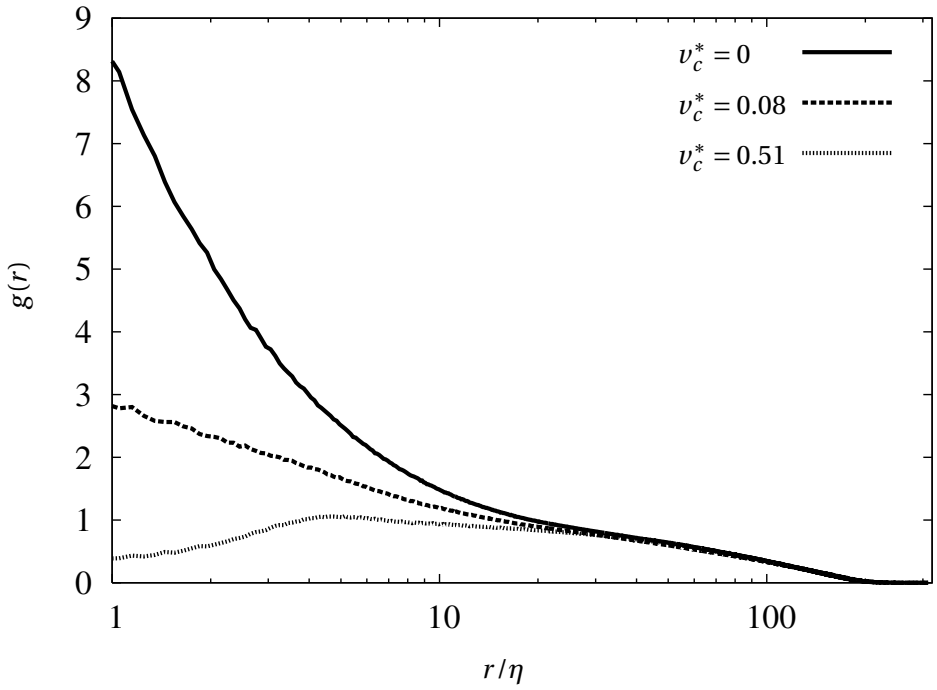

Figure 4.18: Radial distribution functions ($r/\eta > 1.0$) at different non-dimensional Coulomb velocities for $Re_\lambda = 45.0, St_k = 1.0$.

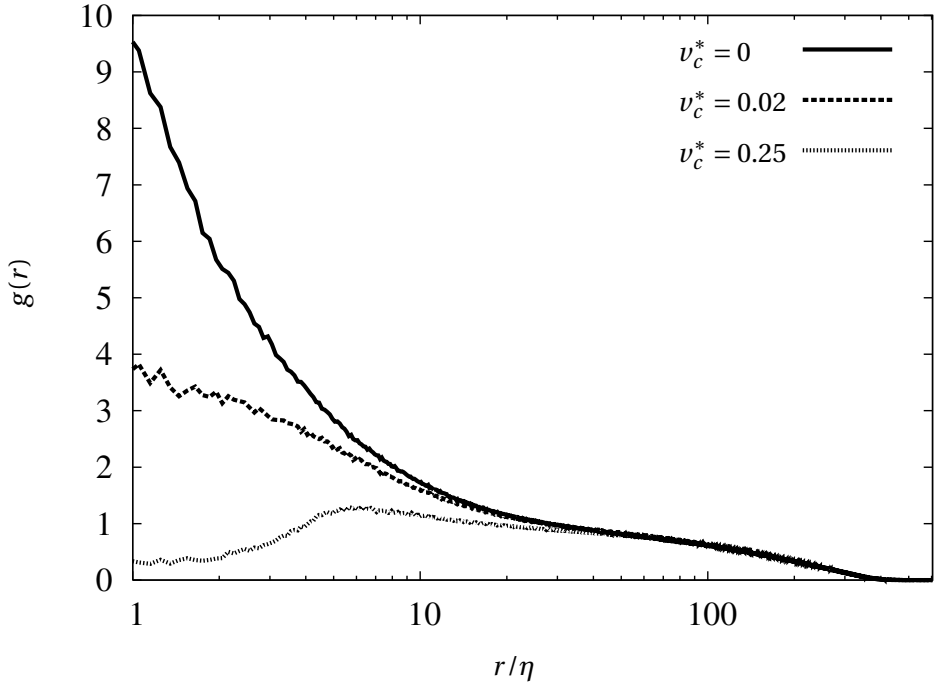

Figure 4.19: Radial distribution functions ($r/\eta > 1.0$) at different non-dimensional Coulomb velocities for $Re_\lambda = 80.6, St_k = 1.0$.

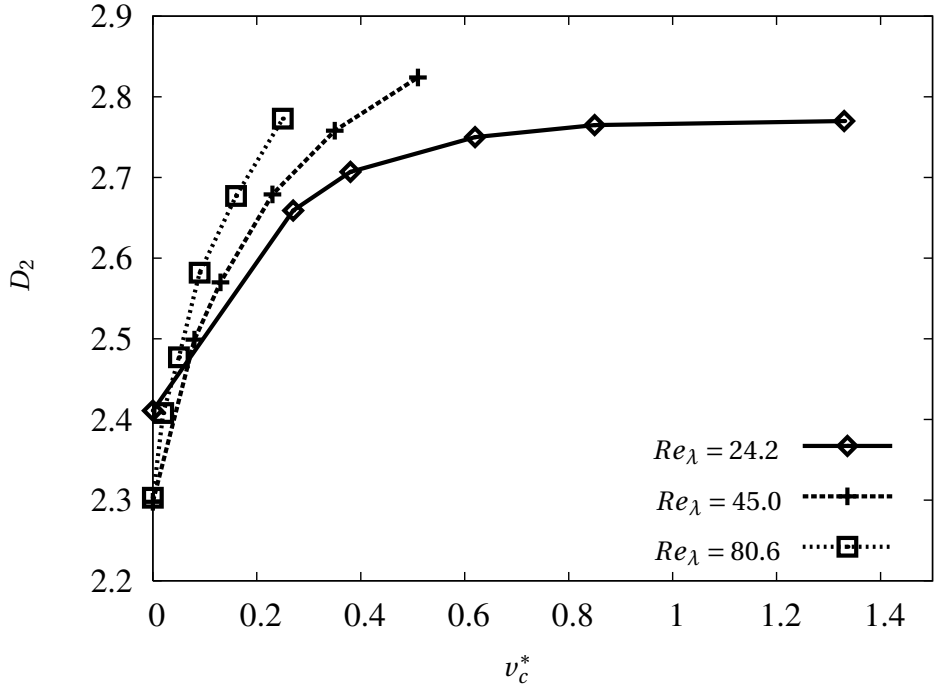

Figure 4.20: Variation of D_2 measure with non-dimensional Coulomb velocity for $Re_\lambda = 24.2, 45.0, 80.6$ at $St_k = 1.0$.

10η and 20η. The increase in D_2 values with increasing v_c^* is further elucidated by plotting the number of particle pairs at a given separation at different v_c^*. Figure 4.21 shows that the number of particle pairs with separations of the order of the Kolmogorov scale are greatly reduced in the presence of charge.

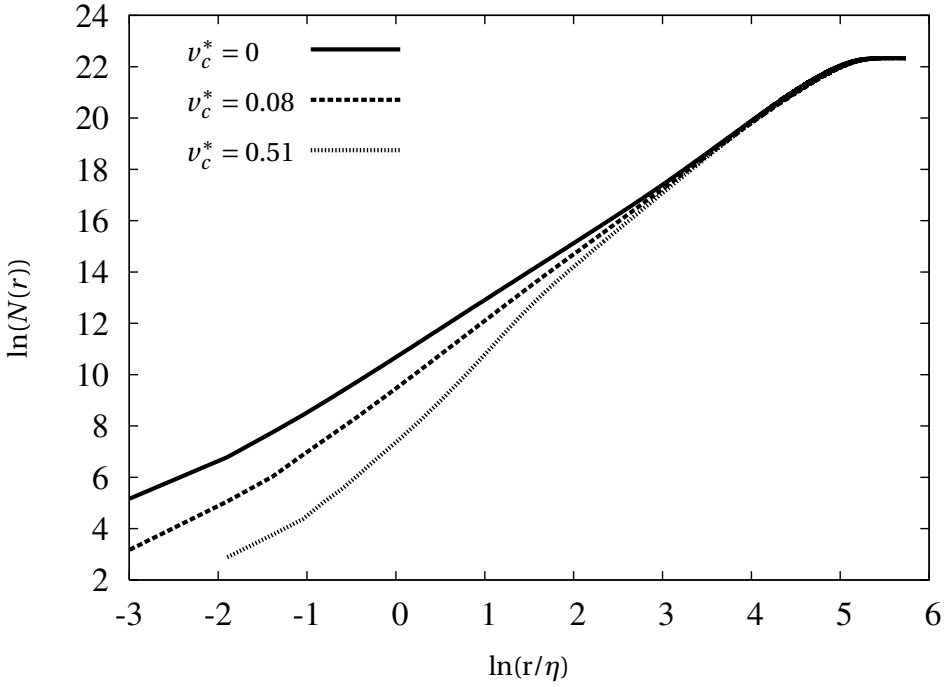

Figure 4.21: Number of particle pairs within separation r at different non-dimensional Coulomb velocities for $Re_\lambda = 45.0, St_k = 1.0$.

In the presence of a Lorentz force field, the particle distribution is governed by the relative magnitudes of drag and Lorentz forces acting on the particles. The balance between Lorentz and drag forces experienced by the particles is depicted in figure 4.22. When this ratio exceeds unity, the Lorentz force dominates the particle motion. For $Re_\lambda = 24.2$, this regime of Lorentz force dominance is seen to take over at $v_c^* \approx 0.5$, while for $Re_\lambda = 45.0$, it occurs at $v_c^* \approx 0.4$. It is noted that the range of Coulomb velocities simulated for $St_k = 1.0$ particles at the highest Reynolds number is limited to non-dimensional Coulomb velocities below 0.25. Thus the Lorentz forces experienced by the $St_k = 1.0$ particles at highest Reynolds number are always less than the drag force.

Figure 4.23 shows the distance to nearest particle, $x_{\min}$, averaged over all particles, for $Re_\lambda = 24.2$. In the accumulated condition, particles are closer to each other and thus $x_{\min}$ reduces. In general,

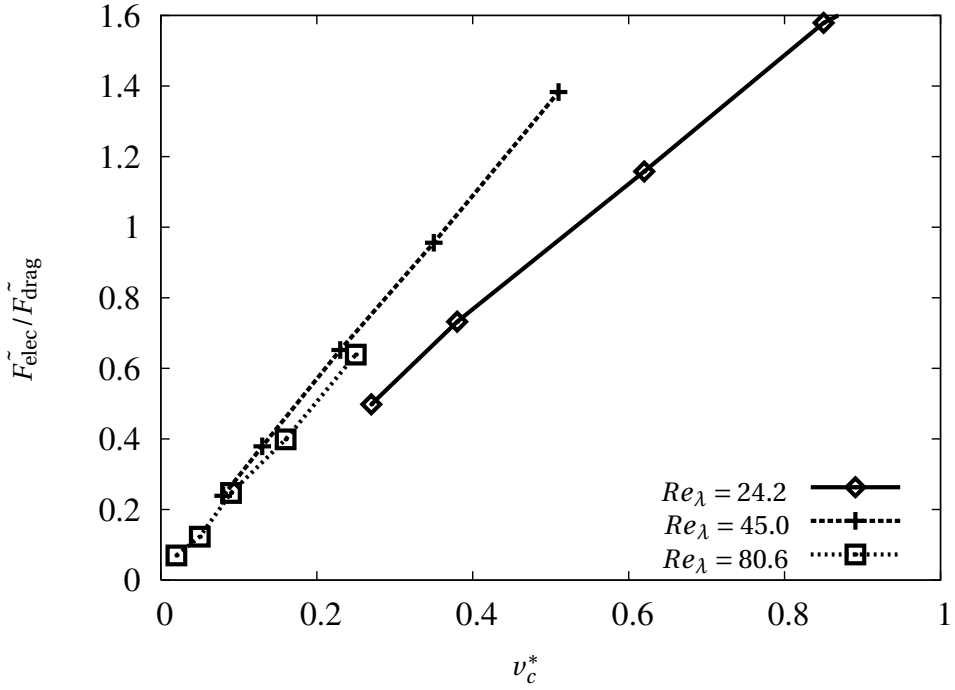

Figure 4.22: Lorentz force normalised by drag force averaged over all the particles for $St_k = 1.0$ particles at different non-dimensional Coulomb velocities and Reynolds numbers.

with increasing charge levels, this distance increases indicating reduction in accumulation phenomenon. However small Stokes number particles for this Reynolds number show reduction in distance to the nearest particle for non-dimensional Coulomb velocities of $v_c^* > 0.5$.

The electric field is calculated by taking into account the Eulerian variation of the charge density in the domain. This method implicitly assumes that the Lorentz force due to the nearest particle is small compared to the effect of all the particles combined. This assumption is verified by considering an electrical length scale, x_E, which denotes the separation between particles corresponding to the mean electric field attained in the domain, given by

$$x_E = \frac{q_p}{4\pi\epsilon_0 E_{\text{rms}}}. \tag{4.8}$$

Figure 4.24 justifies the assumption that the particle separations in the simulations are always greater than the electrical length scale, x_E.

The reduction in dispersion of particles with increasing charge levels is evident in figure 4.25. The reduction in dispersion in the x-direction due to charge at $v_c^* = 1.0$ is seen to be much less than

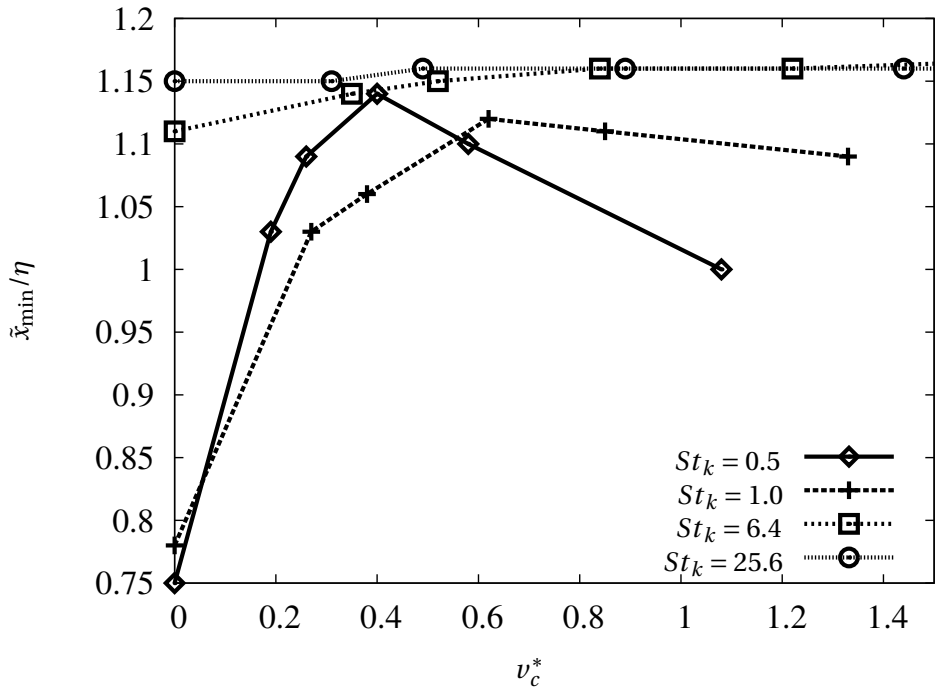

Figure 4.23: Variation of non-dimensional particle separation with non-dimensional Coulomb velocity at different Stokes numbers for $Re_\lambda = 24.2$.

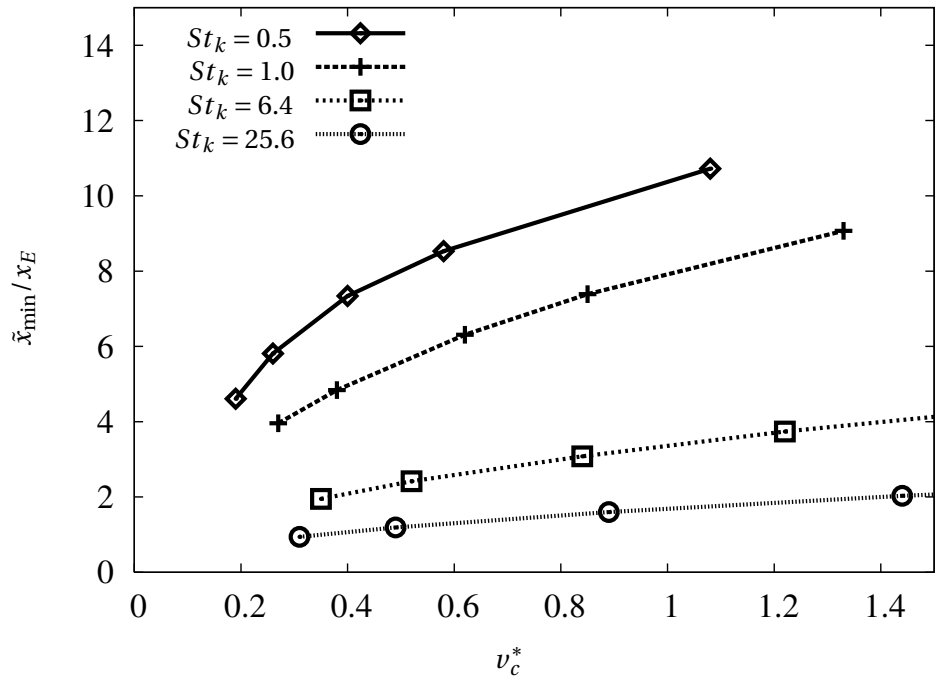

Figure 4.24: Variation of ratio of particle separation to electrical length scale with non-dimensional Coulomb velocity at different Stokes numbers for $Re_\lambda = 24.2$.

that due to gravity at $v_g^* = 1.0$ (figure 3.23). Correspondingly, a weak reduction in the Lagrangian autocorrelation of particle velocity in x-direction with increasing charge levels is seen in figure 4.26.

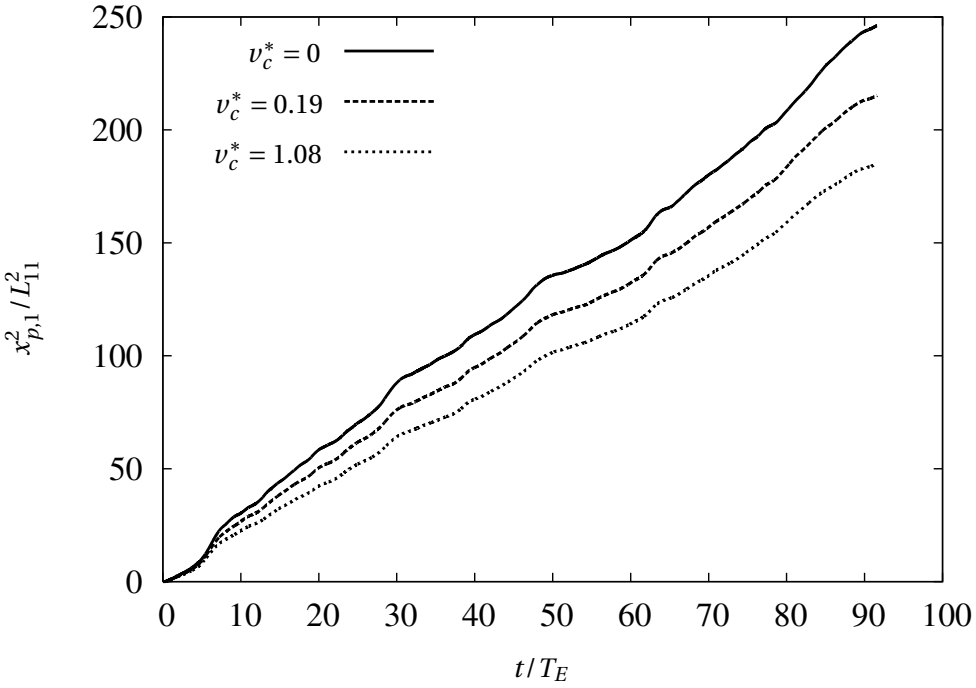

Figure 4.25: Normalised mean square displacement in x-direction at different non-dimensional Coulomb velocities for $Re_\lambda = 24.2, St_k = 0.5$.

4.5 Influence of gravity on charged particles

In order to make the charged particle analysis more practically realistic, gravitational force is also included in the analysis. The magnitude of the gravitational force is characterised by the non-dimensional gravitational settling velocity similar to analysis for uncharged particles (section 3.6).

The effect of gravity on charged particles with $St_k = 1.0$ is explored in figures 4.27, 4.28, 4.29. Stokes number, $St_k = 1.0$ is chosen since effect of gravity is significant at this Stokes number as seen from figures 3.24, 3.25, 3.26. It is observed that in the presence of gravity, less charge is required to mitigate preferential accumulation.

Figures 4.30, 4.31 and 4.32 show the values of the D measure at different charge levels in the pres-

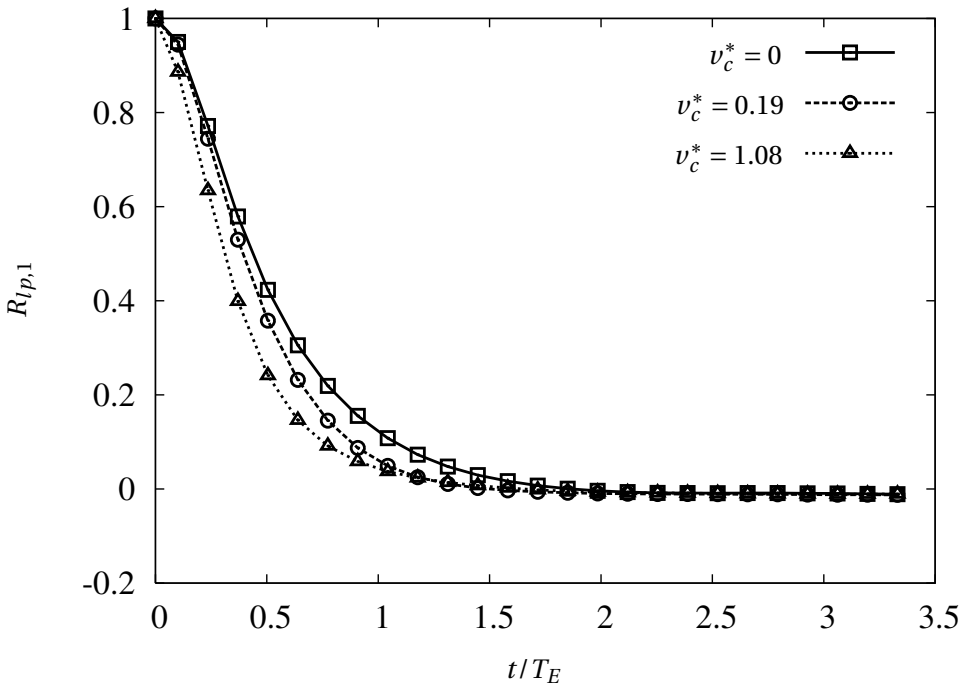

Figure 4.26: Lagrangian velocity autocorrelation of particles in x-direction, $R_{lp,1}$ at different non-dimensional Coulomb velocities for $Re_\lambda = 24.2, St_k = 0.5$.

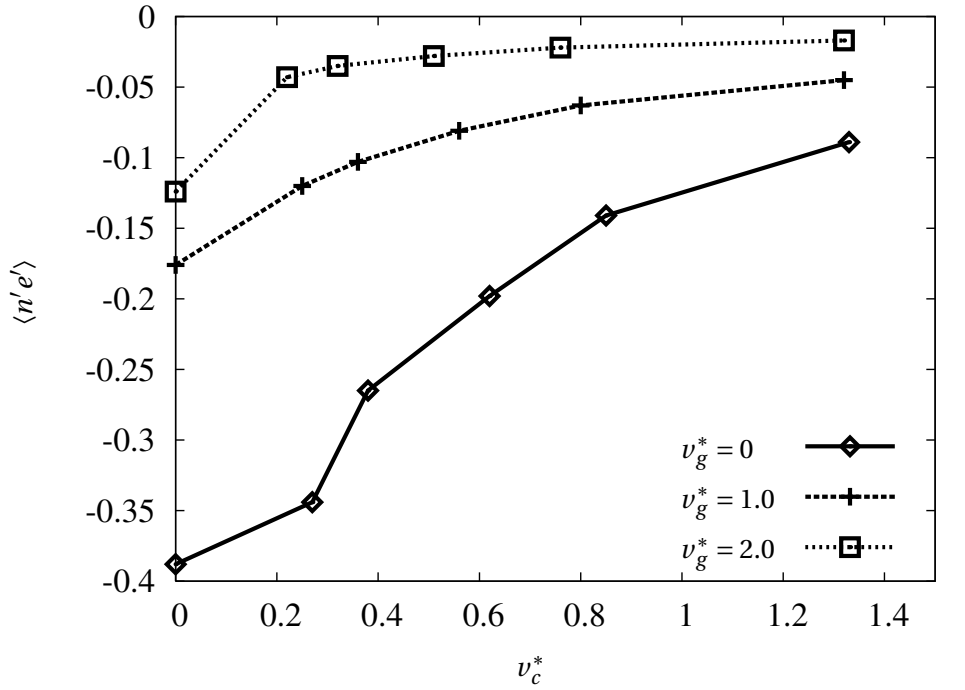

Figure 4.27: Variation of $\langle n'e' \rangle$ with non-dimensional Coulomb velocity at different gravitational settling velocities for $Re_\lambda = 24.2, St_k = 1.0$.

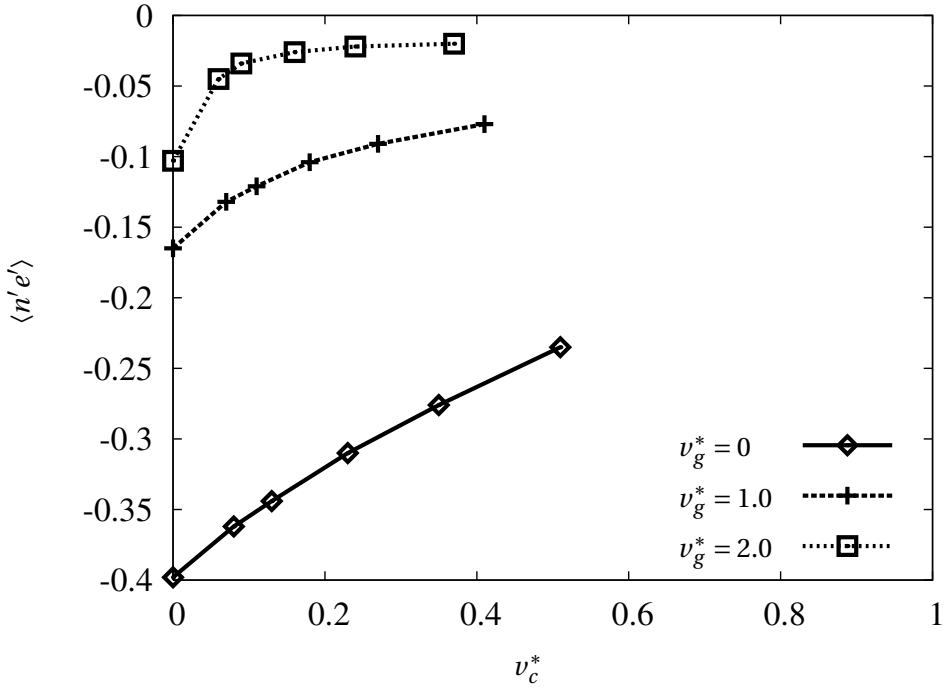

Figure 4.28: Variation of $\langle n'e' \rangle$ with non-dimensional Coulomb velocity at different gravitational settling velocities for $Re_\lambda = 45.0, St_k = 1.0$.

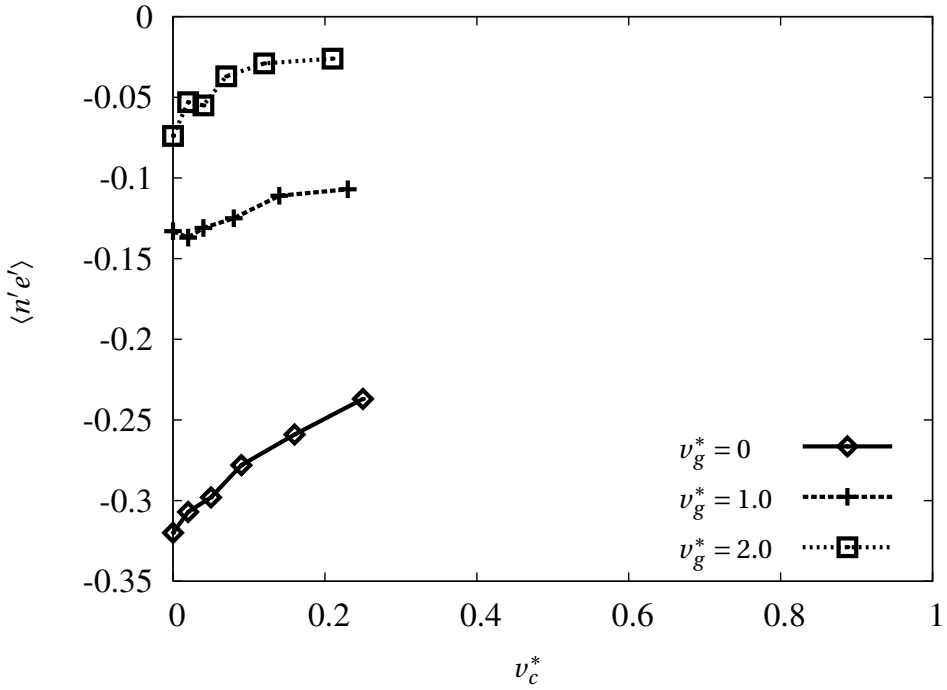

Figure 4.29: Variation of $\langle n'e' \rangle$ with non-dimensional Coulomb velocity at different gravitational settling velocities for $Re_\lambda = 80.6, St_k = 1.0$.

ence of gravity. These figures further confirm that less charge is required in the presence of gravity to mitigate accumulation. It is observed for $Re_\lambda = 24.2$ that at $v_g^* = 2.0$, a Coulomb velocity corresponding to $v_c^* \approx 0.6$ produces the same homogenization effect that $v_c^* = 1.0$ does in the absence of gravity.

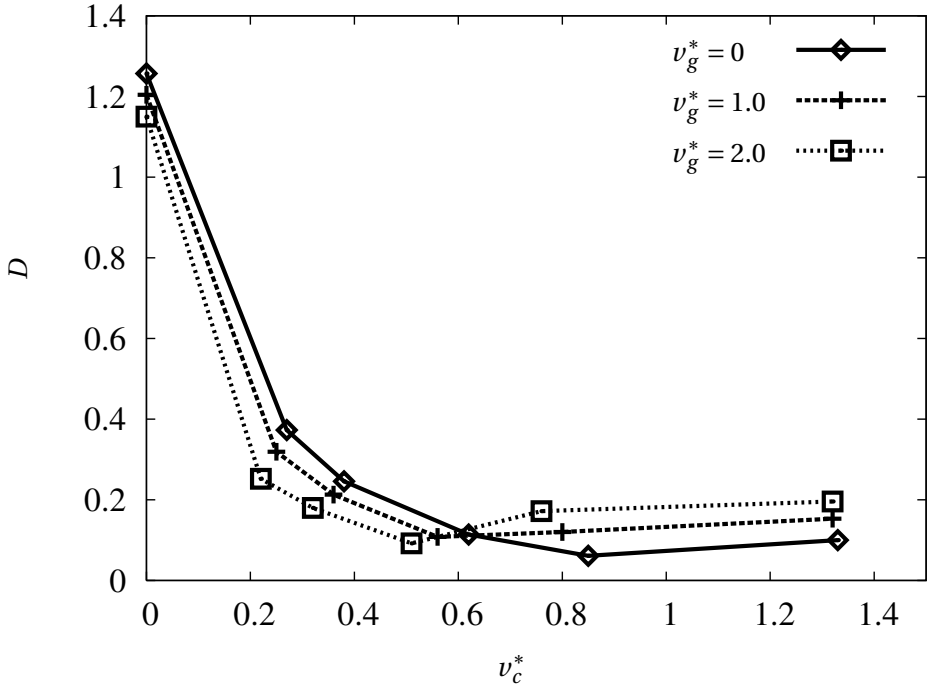

Figure 4.30: Variation of D measure with non-dimensional Coulomb velocity at different gravitational settling velocities for $Re_\lambda = 24.2, St_k = 1.0$.

Figure 4.33, 4.34 and 4.35 show the values of the correlation dimension, D_2, at different charge levels in the presence of gravity. These figures further confirm that less charge is required to homogenise particle distribution in the presence of gravity.

4.6 Comparison with experiments

Results from present simulations have been compared with the experimental results obtained by Lu et al. [8]. Figure 4.36 compares the RDF obtained from the present study with that reported in the experimental work of Lu et al. [8]. In their experiment, the charge level in the domain was characterised by the ratio $E_{\text{charge}}/E_{\text{turb}}$ and the N_s value in the simulations has been chosen to match

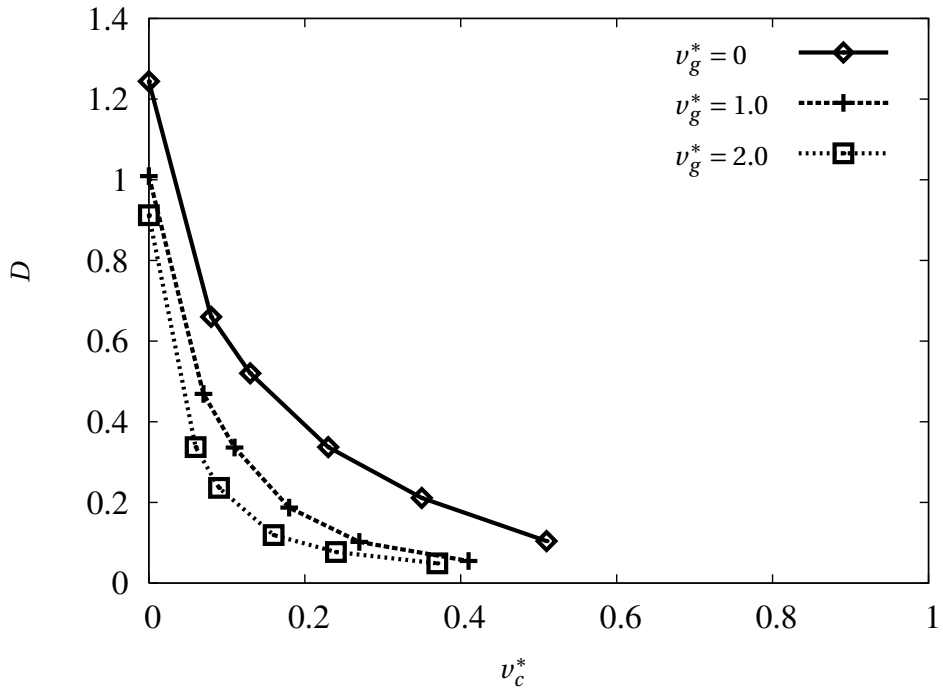

Figure 4.31: Variation of D measure with non-dimensional Coulomb velocity at different gravitational settling velocities for $Re_\lambda = 45.0, St_k = 1.0$.

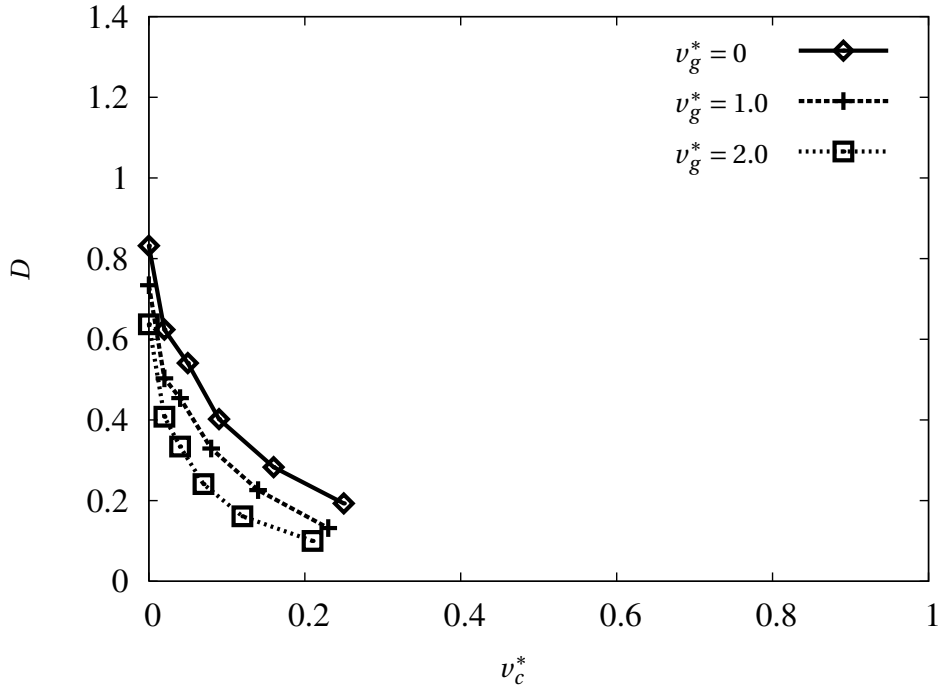

Figure 4.32: Variation of D measure with non-dimensional Coulomb velocity at different gravitational settling velocities for $Re_\lambda = 80.6, St_k = 1.0$.

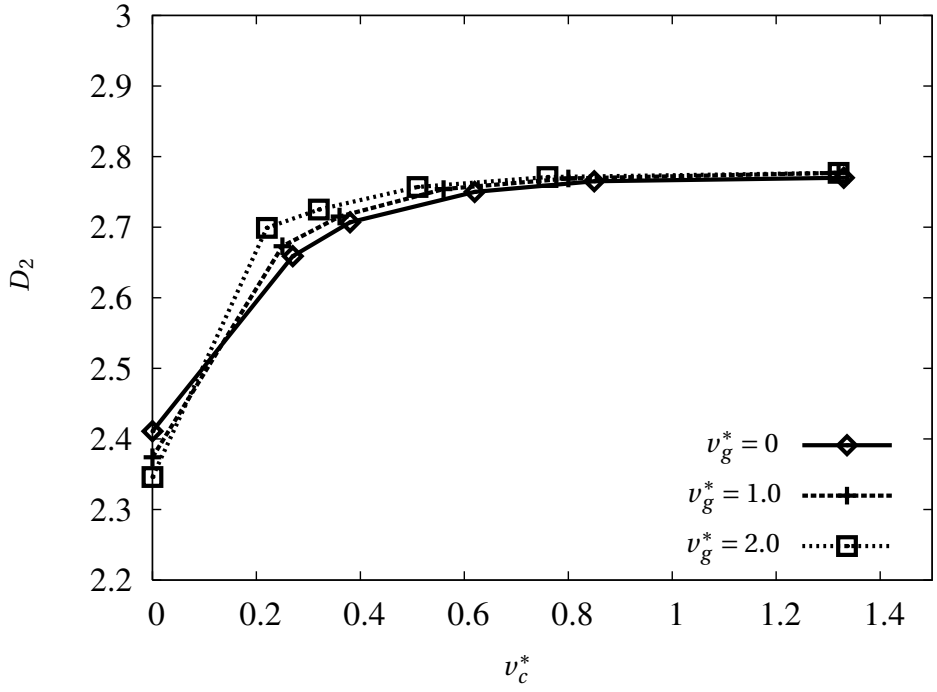

Figure 4.33: Variation of D_2 measure with non-dimensional Coulomb velocity at different gravitational settling velocities for $Re_\lambda = 24.2, St_k = 1.0$.

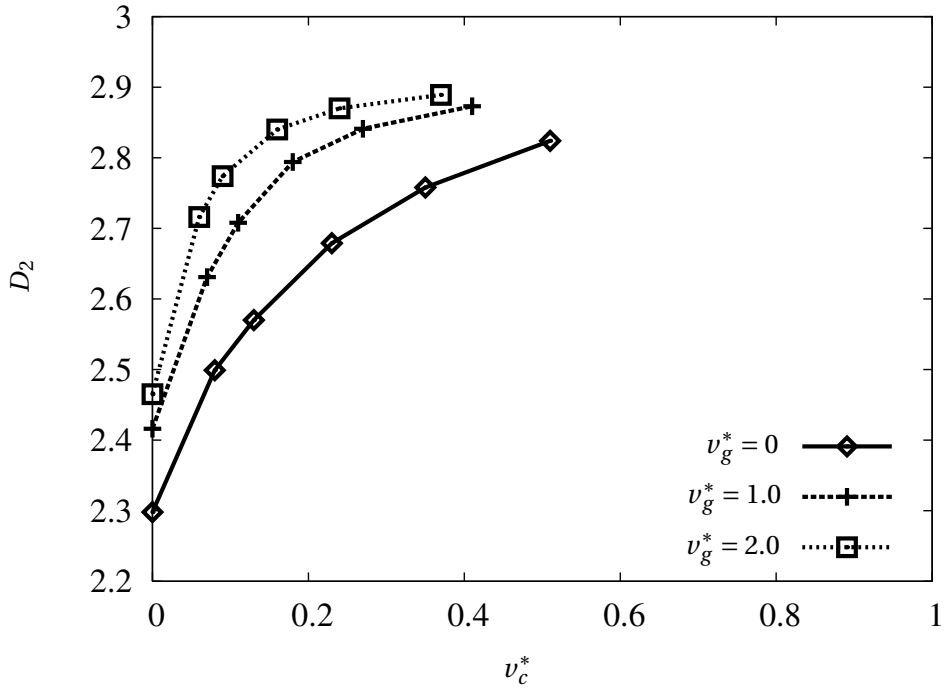

Figure 4.34: Variation of D_2 measure with non-dimensional Coulomb velocity at different gravitational settling velocities for $Re_\lambda = 45.0, St_k = 1.0$.

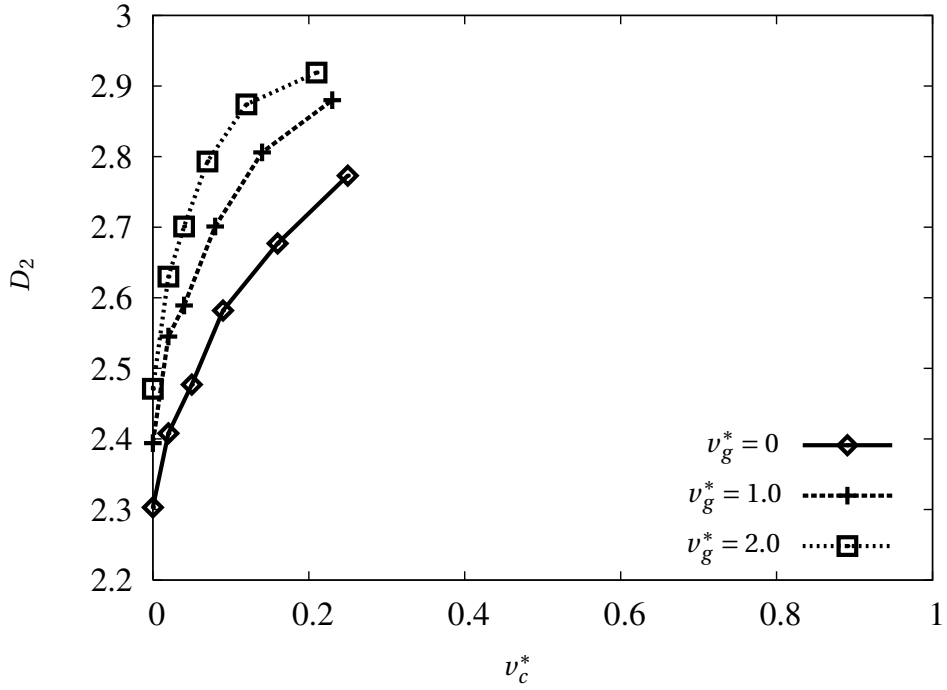

Figure 4.35: Variation of D_2 measure with non-dimensional Coulomb velocity at different gravitational settling velocities for $Re_\lambda = 80.6, St_k = 1.0$.

the energy ratio reported in the experiment. The non-dimensional Coulomb velocity corresponding to the experimental conditions is $v_c^* = 0.035$. Table 4.2 compares the turbulence, particle and charge parameters for the present study with that of Lu et al. [8]. It should be noted from Figure 4.36 that incorporating gravity ($v_g^* = 1.0$) leads to a better agreement with the experimental results. This is expected since the experiments were performed under the influence of gravity.

	Lu *et al.*	present
Re_λ	84	80.6
St_k	0.3	0.3
$E_{\text{charge}}/E_{\text{turb}}$	2.0	2.0

Table 4.2: Comparison of turbulence, particle and charge parameters for present study with those used by Lu et al. [8] (simulations labeled 1c in their paper)

Results from present work have also been compared with the experiments on settling charged particles conducted by Shaw et al. [9]. In their experiments, droplets with two sizes were used and subjected to increasing gravitational settling using an artificially imposed electric field to create the settling effect. The non-dimensional parameters in the simulations have been adjusted to match the corresponding experimental runs and are listed in table 4.3.

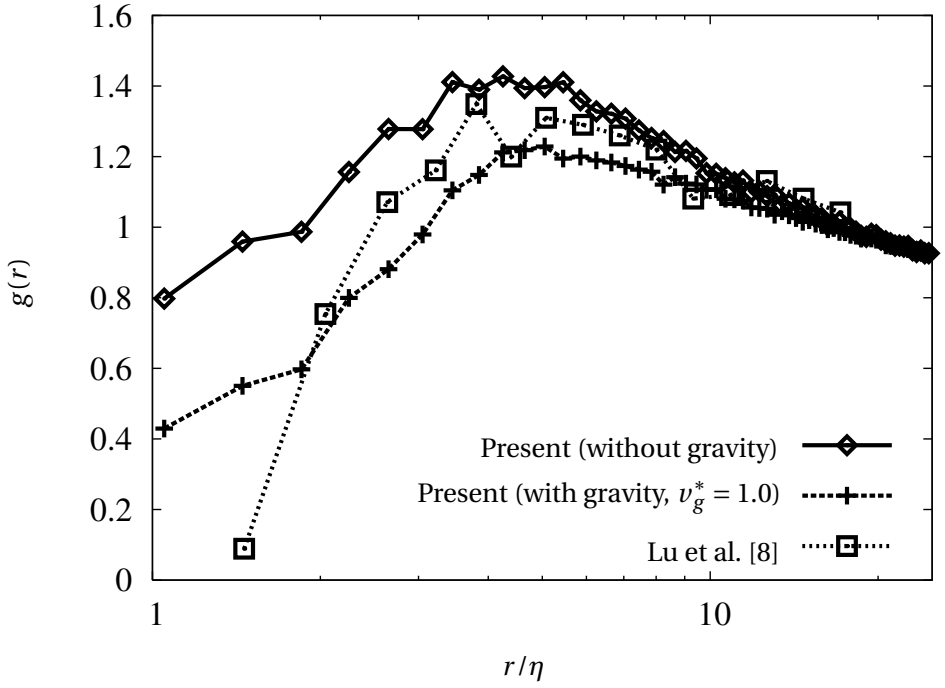

Figure 4.36: Radial distribution functions for present study compared with that reported in Lu et al. [8] (parameters have been listed in table 4.2).

	1s	2s	3s	1d	2d	3d
Re_λ	80	80	80	80	80	80
St_k	0.14	0.14	0.14	0.22	0.22	0.22
v_g^*	0.354	0.664	0.797	0.554	1.041	1.262
v_c^*	0.0067	0.0070	0.0068	0.022	0.021	0.021

Table 4.3: Non-dimensional parameters for present simulations corresponding to experimental conditions reported by Shaw et al. [9]. Simulations 1s, 2s, 3s correspond to the 'singlet' experimental runs at increasing gravity levels. Simulations 1d, 2d, 3d correspond to the 'doublet' experimental runs at increasing gravity levels.

Figures 4.37, 4.38 and 4.39 compare the results from the present simulations with the 'singlet' experimental results reported in Shaw et al. [9]. Figures 4.40, 4.41 and 4.42 compare the results from the present simulations with the 'doublet' experimental results reported in Shaw et al. [9]. Reasonably good agreement with experiments is observed given the uncertainties involved in the experiments. This agreement lends credence to the analysis of settling charged particles carried out in the present work. It can be noted that the non-dimensional Coulomb velocities for the experiments are very small, whereas the current analysis shows that $v_c^* \approx 1.0$ tends to appreciably mitigate accumulation. The results from the simulations match the functional form of the RDF for settling charged particles proposed by Shaw et al. [9]. However it should be borne in mind that

the theory is strictly valid only for $St_k \ll 1$ and interpretation of the present results at high Stokes numbers using the theory is strictly not permissible.

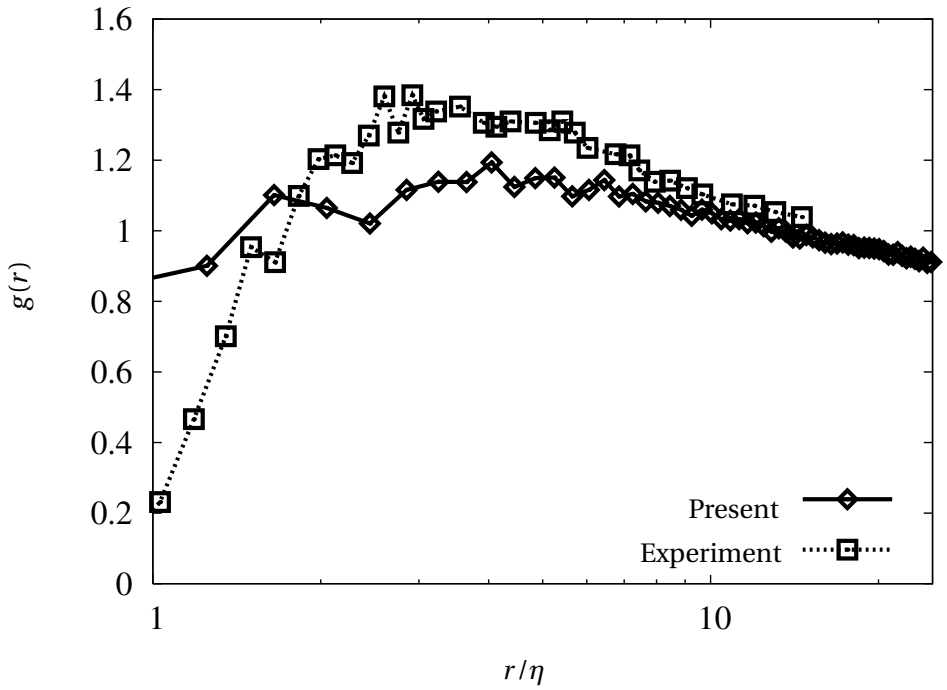

Figure 4.37: Radial distribution functions for present study compared with that reported in Shaw et al. [9] for Run 1s (refer table 4.3).

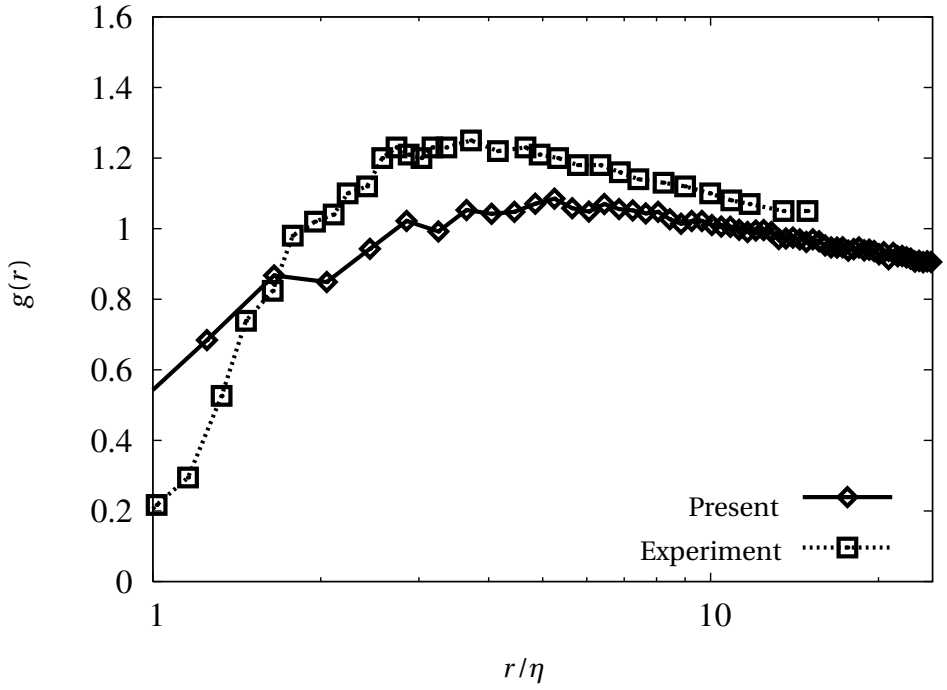

Figure 4.38: Radial distribution functions for present study compared with that reported in Shaw et al. [9] for Run 2s (refer table 4.3).

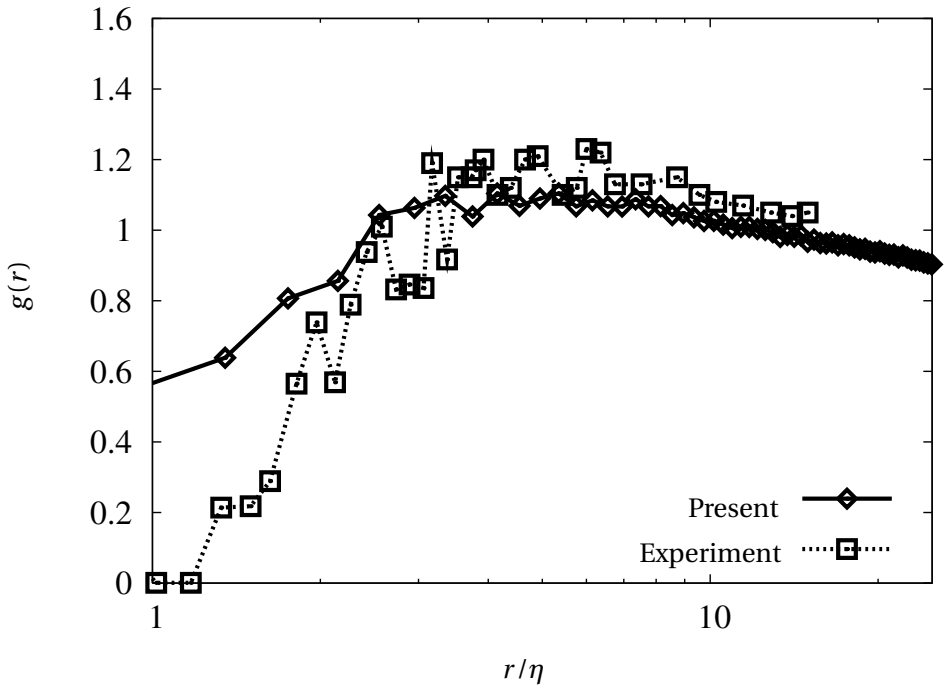

Figure 4.39: Radial distribution functions for present study compared with that reported in Shaw et al. [9] for Run 3s (refer table 4.3).

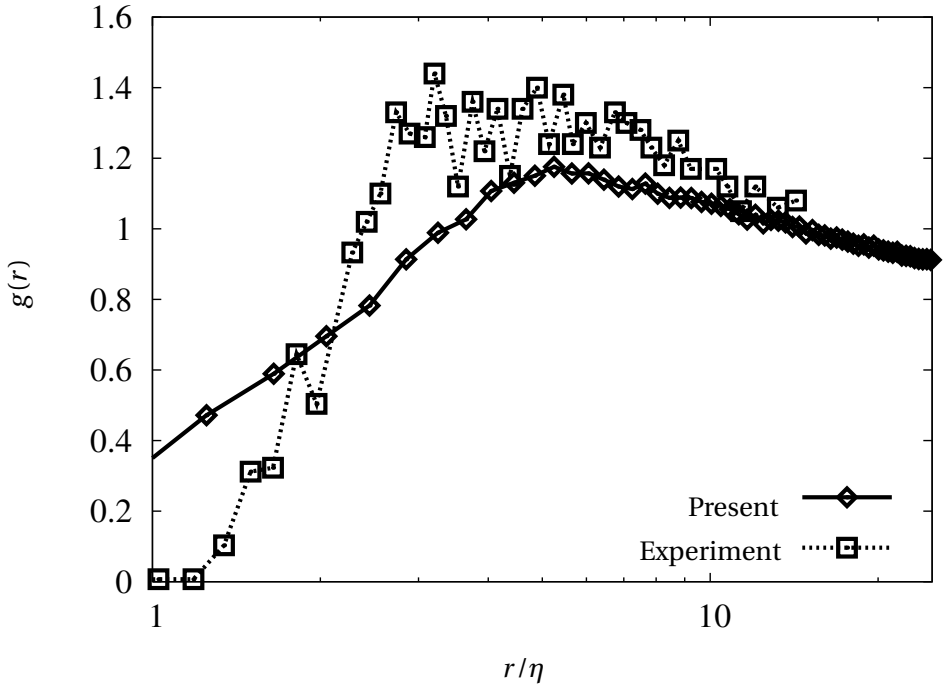

Figure 4.40: Radial distribution functions for present study compared with that reported in Shaw et al. [9] for Run 1d (refer table 4.3).

4.7 Summary

Charging of particles has been proposed as a means of mitigating preferential accumulation. Results from simulations of charged particles in isotropic turbulence have been presented. Results

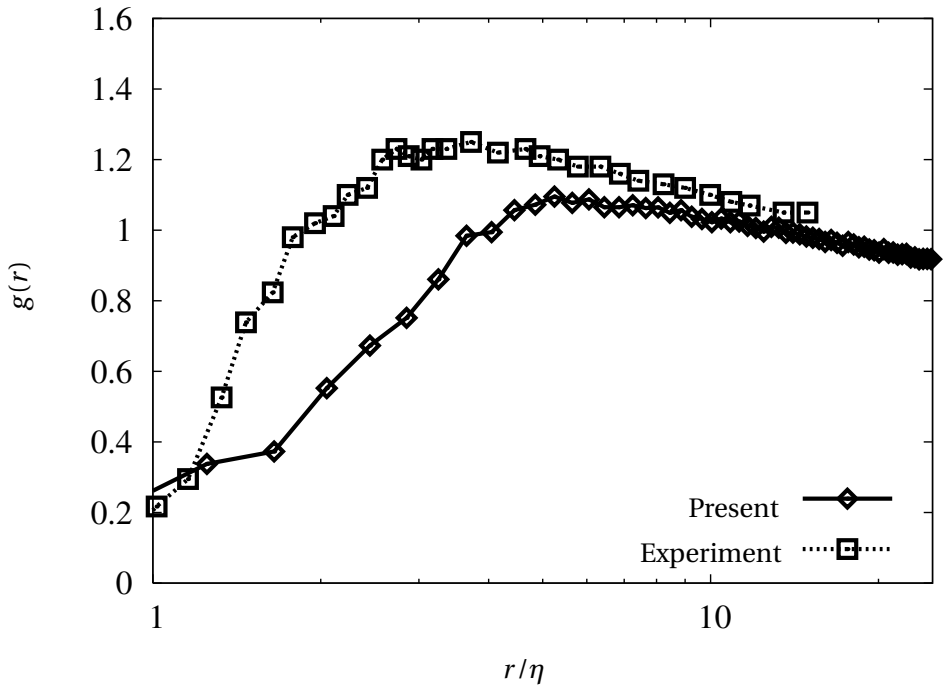

Figure 4.41: Radial distribution functions for present study compared with that reported in Shaw et al. [9] for Run 2d (refer table 4.3).

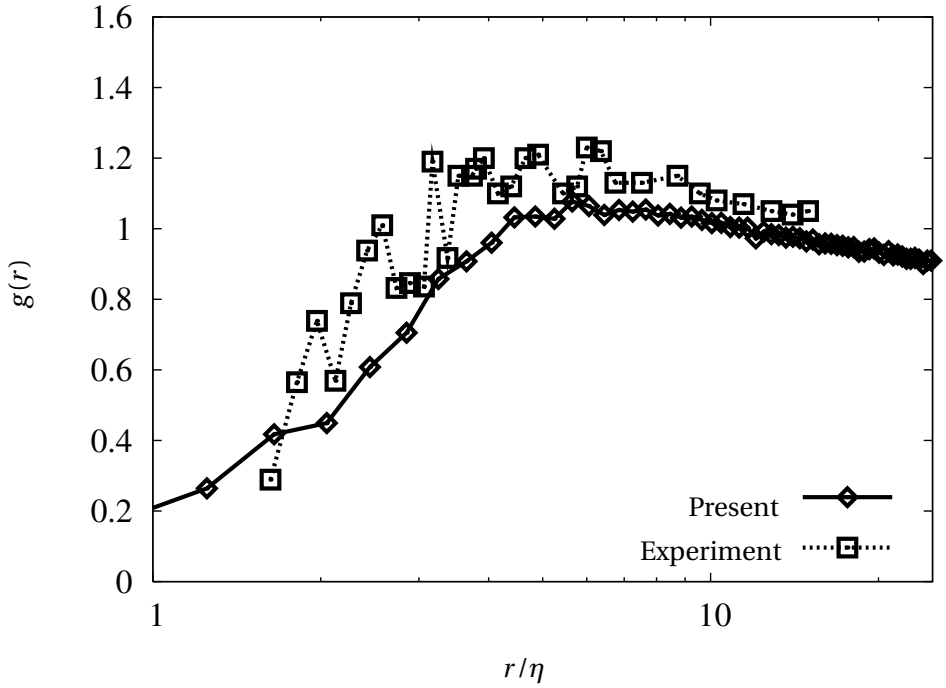

Figure 4.42: Radial distribution functions for present study compared with that reported in Shaw et al. [9] for Run 3d (refer table 4.3).

have been presented both neglecting and including the effect of gravity. The findings from the investigations carried out in this chapter can be summarised as follows:

- It is observed that the particle distribution reaches a statistically steady state even in the presence of charges on particles. This is by no means obvious since the electric field is generated only due to non-uniformity of particle distribution. Simulations have been carried out by systematically varying the charge on particles to study the effect of the magnitude of the electric field on particle distribution. The magnitude of electric field is characterised by the non-dimensional Coulomb velocity, v_c^*.

- In the absence of gravity, it is estimated that $v_c^* \approx 1.0$ is sufficient to homogenise a preferentially accumulated particle distribution. It is seen that charging drastically reduces the RDF values at Kolmogorov scale separations. This implies that charging the particles is an efficient means to destroy particle clusters.

- The presence of charge reduces the dispersion of particles. The reduction in dispersion due to the presence of charge on particles at $v_c^* = 1.0$ is much less than the reduction due to gravity at $v_g^* = 1.0$.

- On incorporating the gravitational force, the amount of charge required to homogenise the particle distribution is reduced. It is estimated that $v_c^* \approx 0.6$ is sufficient to homogenise particle distribution at $v_g^* = 2.0$. This estimation is corroborated by several different indicators of accumulation.

- It is shown that the bulk charge density levels required to homogenise particle distribution correspond to those attained around 2cms from tip of the nozzle in practical charged injection atomizers. Thus placing charges on particles holds the promise of creating a more homogeneous mixture downstream of the spray. This is especially useful in the context of combustion where de-mixing of the fuel-vapor mixture results in incomplete combustion and formation of soot and other pollutants.

- The results from simulations carried out in the present work agree reasonably well with corresponding experiments reported in the literature. The RDF obtained from simulations matches the functional form of the RDF proposed initially by Chun et al. [53] and the extended form for settling charged particles suggested by Shaw et al. [9]. Thus the drift-diffusion model of Chun et al. [53] seems to be an appropriate starting point to explain the clustering of inertial particles.

Chapter 5

Two-way coupled investigations

5.1 Background

The modulation of turbulence due to the presence of particles is a phenomenon of interest in numerous engineering applications such as pneumatic conveyers, process industries, etc. Understanding the mechanisms of modification of carrier phase turbulence has proved difficult, since there are several mechanisms which act simultaneously. Balachandar and Eaton [67] have recently reviewed numerous experimental and numerical investigations of turbulence modification.

Experiments have shown that dynamics of particle-laden turbulent flows are governed by many different parameters, like particle size, Stokes number, mass loading, particle Reynolds number and particle-wall collision dynamics. Often, more than one of these parameters is dominant and thus it is not simple to predict the effect of particles on carrier phase turbulence. Gore and Crowe [68] compiled data from numerous investigations of pipe and jet flows to identify how particle size influences carrier phase turbulence intensity. They observed that particles less than 1/10 of the integral length scale of the fluid turbulence attenuate turbulence intensity whereas particles larger than this size augment it. The different regimes of interaction proposed by Elghobashi [2] (Figure 1.1) indicate that particles can augment or attenuate turbulence depending on their Stokes numbers.

One of the consistent observations among several studies has been the attenuation of turbulence due to particles smaller than the Kolmogorov length scale. Hwang and Eaton [69] conducted experiments with small heavy particles in homogeneous isotropic turbulence and observed attenuation of turbulent kinetic energy in their experiments. They conducted experiments at two turbulence levels and mass loading up to $\phi_p = 0.29$ for particles with Stokes number nearly 60. At the highest mass loading, they observed that the ratio of loaded to unloaded turbulent kinetic energy $k/k_{\phi_p=0} = 0.61$. Their results show that particles increasingly dissipate fluid kinetic energy with increased loading, with the reduction in kinetic energy being relatively independent of the particle relaxation time. Squires and Eaton [70] observed that increased mass loading attenuated an increasing fraction of the turbulence energy and that the fraction of turbulence kinetic energy in the high wavenumbers was increased relative to the energy in the low wavenumbers, for increasing values of the mass loading. Yang and Shy [71] conducted experiments on settling of particles in homogeneous isotropic turbulence. Their experiments have helped further our understanding of particle settling rate, preferential accumulation and turbulence modification. They proposed a simple energy balance model for turbulence modification to explain the observed results. Boivin et al. [35] investigated turbulence modification using DNS of stationary isotropic turbulence with monosized particle population at $Re_\lambda = 62$. Particles with Stokes numbers ranging from 1.26 to 11.38 were used in the simulations and mass loadings up to $\phi_p = 1.0$ were investigated. Gravity was neglected in all the simulations. They found that the fluid energy spectrum is non-uniformly modified by the particles with the small scales showing a relative increase in kinetic energy. At the highest mass loading, they found that the ratio of loaded to unloaded turbulent kinetic energy, $k/k_{\phi_p=0}$, is 0.44 for the smallest (Stokes number) particles. Recently, Lucci et al. [72] observed reduction in turbulent kinetic energy due to Taylor length scale size particles in decaying isotropic turbulence.

Elgobashi and Truesdell [73] have examined modification of decaying homogeneous turbulence due to interaction with dispersed particles. They showed that particles increase the fluid turbulence energy at high wavenumbers but the turbulence energy eventually decays faster than in the case of one-way coupling. In a gravitational environment, they noted that a reverse cascade of turbulence kinetic energy occurs, leading to reduction in its rate of decay. Truesdell and Elgobashi [74] have examined the effects of two-way interaction on particle dispersion. They reported that

two-way coupling enhances the Lagrangian velocity autocorrelation of the particle, the fluid point, and the surrounding fluid, compared to that in one-way coupling. The mean-square displacement of the solid particles increased as a result.

In the present study, two-way coupling has been implemented in PANDORA , a solver previously capable of only one-way coupled simulations[1]. The reduction of carrier phase turbulent kinetic energy with increasing mass loading has been verified, consistent with previous reported literature. Non-uniform modification of the energy spectrum with increased energy at high wavenumbers is observed for small Stokes numbers.

5.2 Numerical implementation

Crowe et al. [75] reviewed the numerical models used for two-phase turbulent flows including several methods of implementing two-way coupling. Pseudo-spectral DNS has been previously employed by researchers to investigate two-way coupled particle-laden flows [35, 76]. In the present work, the effect of particles on the fluid was incorporated using the particle-source-in-cell method (described in section 2.2.2). In this method, the net force exerted on the fluid by all particles contained in a computational box is incorporated at the corresponding computational node (centroid of box). Numerous computational studies of turbulence modification have used this technique[35] and it has been reviewed by Eaton [77].

5.3 Simulation parameters

Simulations were carried out at three configurations, 32^3, 64^3 and 128^3 corresponding to Taylor Reynolds numbers 24.2, 45.0 and 80.6 respectively. The Stokes numbers (based on Kolmogorov scale) explored for each of these Reynolds numbers is $0.2, 0.5, 1.0, 3.0, 6.0$ and 10.0. Particle mass loadings up to 1.0 have been investigated for each combination of Reynolds number and Stokes number. The particle phase is assumed to be dilute in all the simulations reported here and particle-particle collisions have been neglected.

5.4 Results

Figures 5.1 and 5.2 capture the attenuation of turbulent kinetic energy with increased mass loading. It is observed that smaller particles (lower St_k) dissipate more kinetic energy than the larger particles.

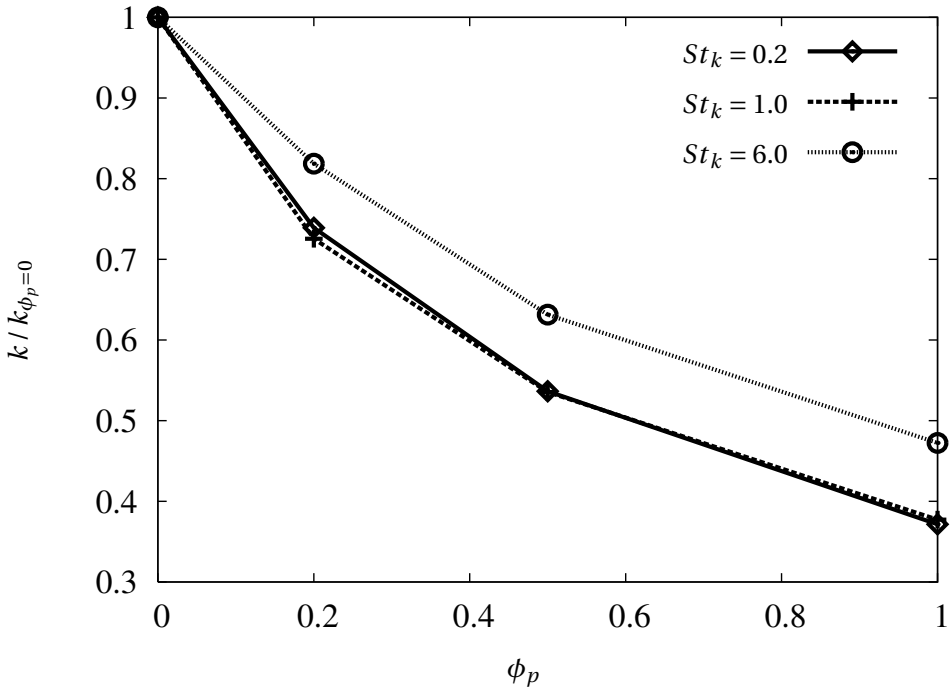

Figure 5.1: Attenuation of turbulent kinetic energy, k, with increasing mass loading, ϕ_p for different Stokes numbers at $Re_\lambda = 24.2$.

The effect of mass loading on the modification of turbulent kinetic energy is probed further by looking at the modification of the kinetic energy spectrum. The non-uniform modification of the spectrum, reported in previous studies[35], is observed in Figures 5.3, 5.4, 5.5 for $Re_\lambda = 24.2$. For $St_k = 0.2$, we see a clear cross-over point in the energy spectrum, wave-numbers above which contain more energy for the loaded case ($\phi_p = 1.0$) than the unloaded case.

It is observed that increasing mass loading leads to attenuation of accumulation at low Stokes numbers while the effect is reversed at higher Stokes numbers for $Re_\lambda = 24.2$ (Figures 5.6, 5.7). This is consistent with observations made by Squires and Eaton [70].

The reduction of accumulation at low Stokes numbers is also reflected in the radial distribution

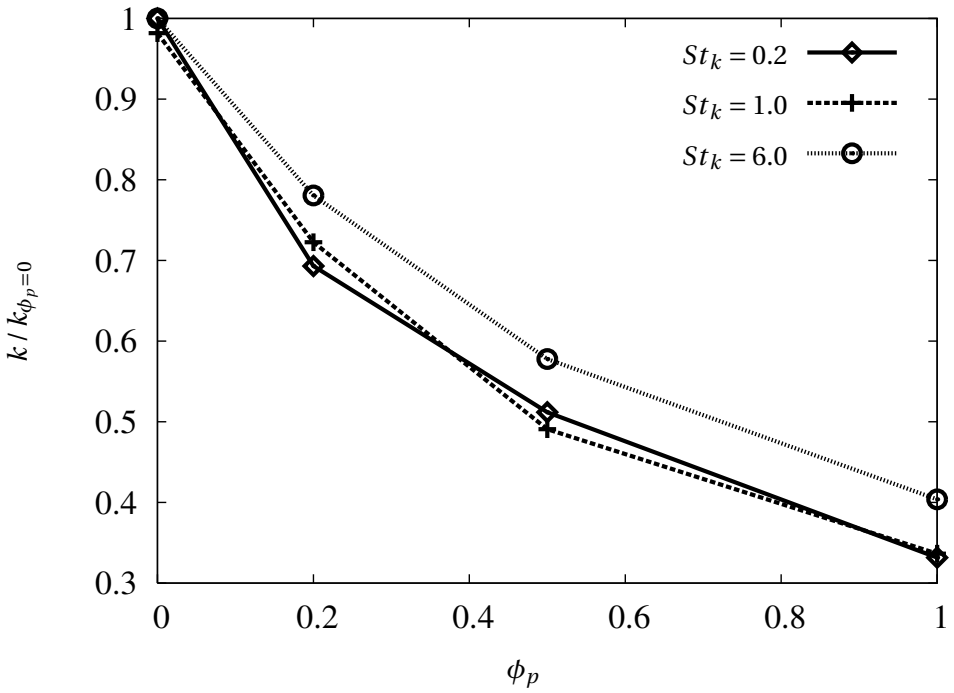

Figure 5.2: Attenuation of turbulent kinetic energy, k, with increasing mass loading, ϕ for different Stokes numbers at $Re_\lambda = 45.0$.

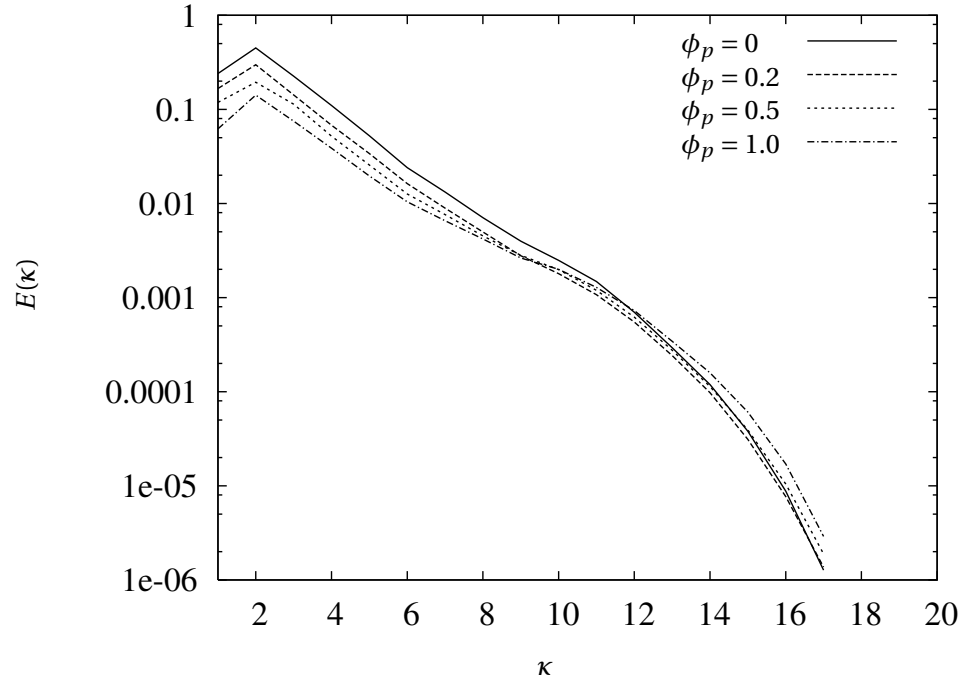

Figure 5.3: Turbulent kinetic energy spectra for different mass loadings at $Re_\lambda = 24.2$, $St_k = 0.2$.

function (Figure 5.8). This suggests that the particle-particle spacing is reduced with increasing mass loading for smaller particles. At high Stokes numbers, the clusters of particles are already

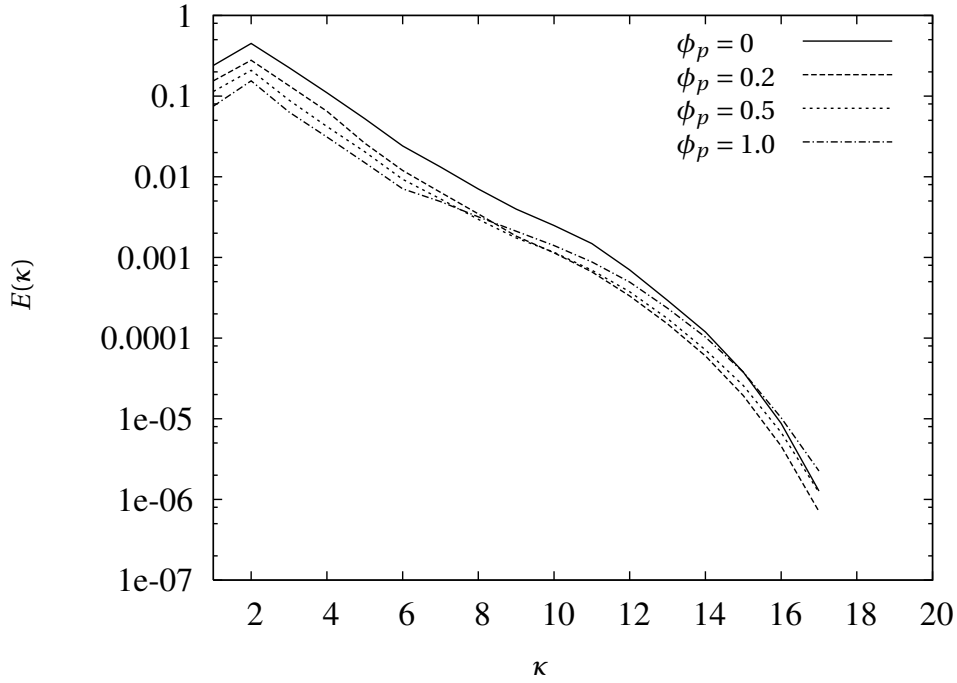

Figure 5.4: Turbulent kinetic energy spectra for different mass loadings at $Re_\lambda = 24.2$, $St_k = 1.0$.

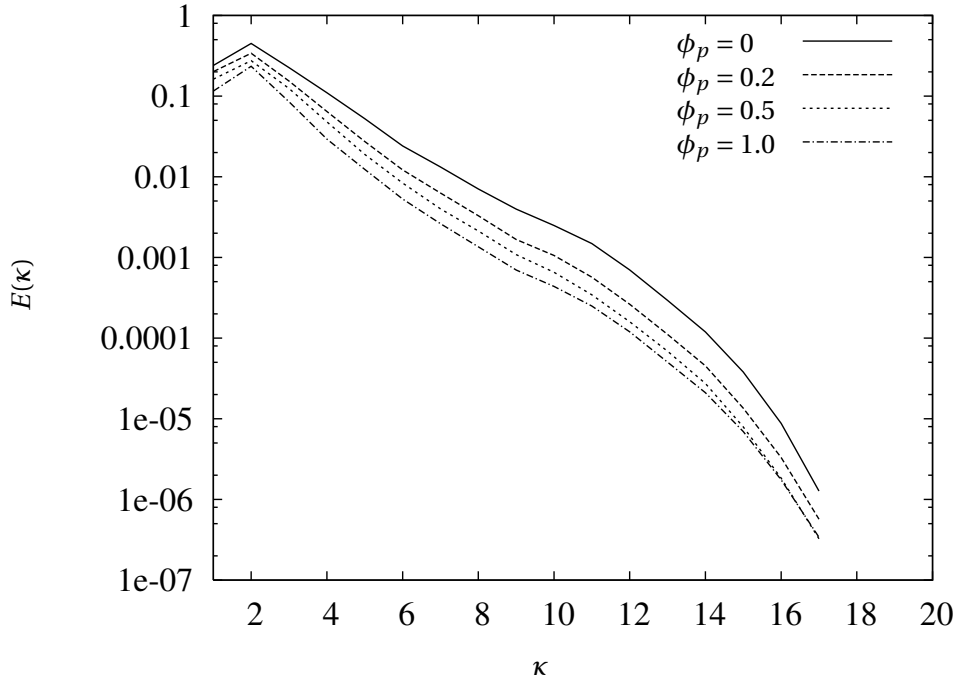

Figure 5.5: Turbulent kinetic energy spectra for different mass loadings at $Re_\lambda = 24.2$, $St_k = 6.0$.

diffuse in the unloaded case, but show a marginal increase in the radial distribution function with increasing mass loading (Figure 5.9).

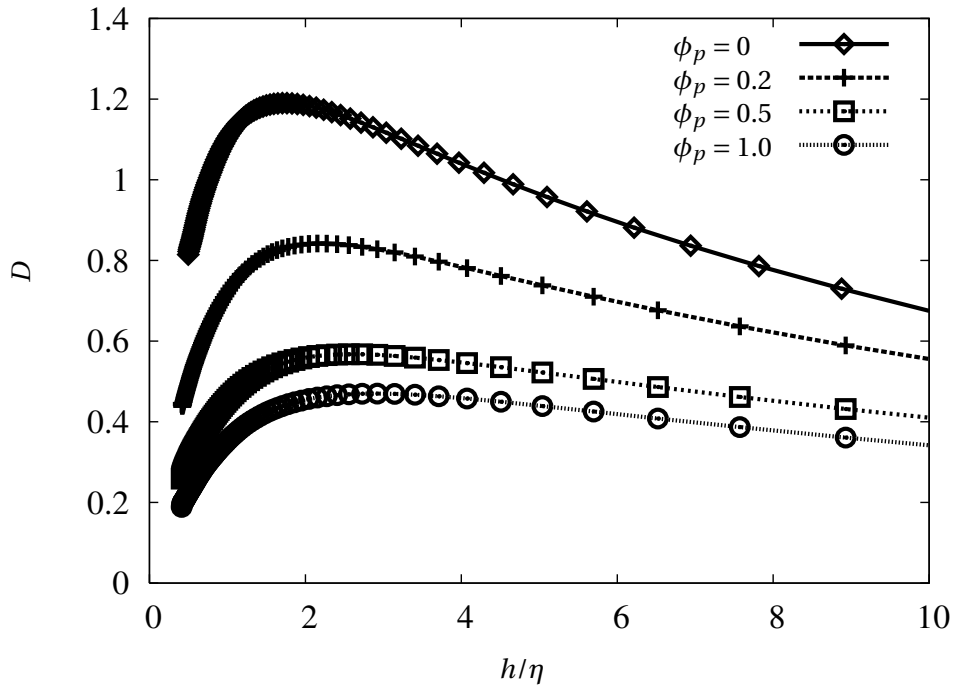

Figure 5.6: dependence of D measure on normalised bin-size, h/η, at different mass loadings for $Re_\lambda = 24.2$, $St_k = 0.5$.

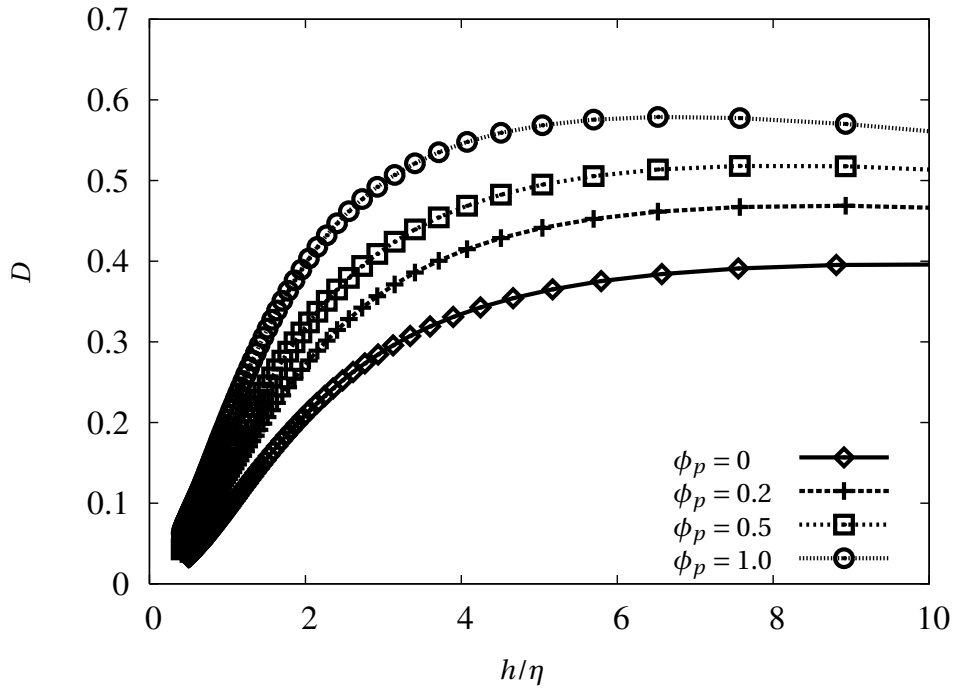

Figure 5.7: Dependence of D measure on normalised bin-size, h/η, at different mass loadings for $Re_\lambda = 24.2$, $St_k = 6.0$.

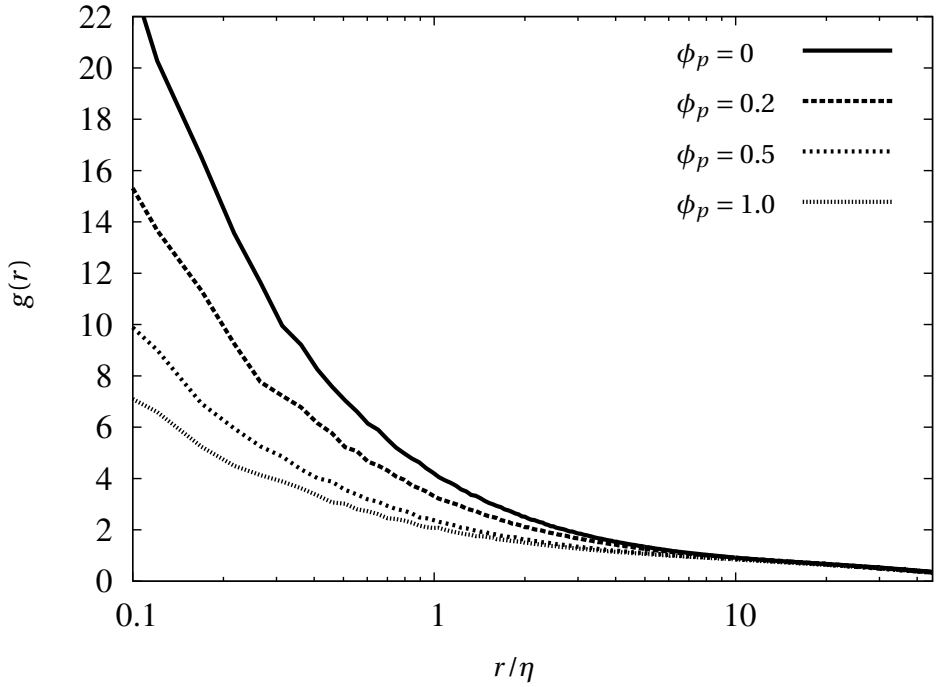

Figure 5.8: Radial distribution functions for different mass loadings at $Re_\lambda = 24.2$, $St_k = 0.5$..

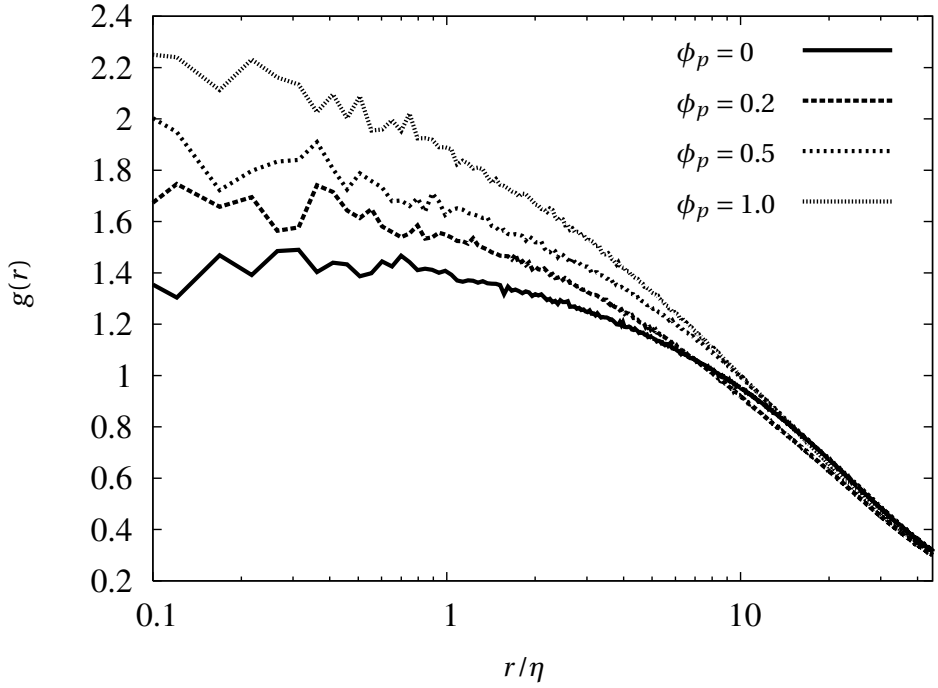

Figure 5.9: Radial distribution functions for different mass loadings at $Re_\lambda = 24.2$, $St_k = 6.0$..

Chapter 6

Conclusions and Further Work

6.1 Conclusions

Simulations of heavy particles in isotropic turbulence have been performed using a point-particle DNS solver, PANDORA . In the situation where the effect of particles on the fluid turbulence is neglected (one-way coupling), it is observed that particles which were initially randomly distributed in the domain tend to be distributed inhomogeneously depending on fluid and particle parameters. This phenomenon, referred to as preferential concentration has been quantified in present work using several different measures. This systematic analysis reveals the length scales associated with maximum clustering and thus identifies the eddy sizes that are predominantly responsible for clustering. Measures probing the particle-particle separations reveal that clustering occurs not only at length scales greater than Kolmogorov length scale, but at sub-Kolmogorov scales too. The scaling of different indicators of accumulation with Reynolds number gives an insight into the multi-scale nature of clustering reported in several previous studies. The effect of a gravitational force on preferential concentration has also been explored.

The insight into the phenomenon of preferential concentration has been used to develop a technique to mitigate accumulation. It has been demonstrated that introducing sufficient charge on particles can destroy the accumulation effect. Charging of particles restores the homogeneity of particle distribution by enabling particles to overcome the drag force due to action of eddies. The

Lorentz force field associated with inhomogeneous distribution of particles also tends to diffuse the particle clusters by reducing correlation between pairs of particles. Good agreement between the present simulations and experiments of settling charged particles has been obtained.

In two-way coupled simulations, the attenuation of turbulent kinetic energy and asymmetric distortion of turbulence spectra due to mass loading of particles have been demonstrated. Two-way coupling effects show a dependence on the Stokes number of the particles. At low Stokes numbers, the accumulation of particles seems to be attenuated while at high Stokes numbers, a marginal increase in indicators of accumulation is observed.

6.2 Future Work

The present work potentially lends itself to benefit the following areas of research in the context of dispersed phase flows.

6.2.1 Two-way coupled studies

The modification of carrier phase turbulence by single particles as well as particle clusters deserves further investigation. The present work has shown that in the accumulated condition, the size of particle clusters is around 10η. Thus the question of attenuation or enhancement of carrier phase turbulence is not straightforward. While the sub-Kolmogorov size individual particles may attenuate turbulence, the larger particle clusters may enhance carrier phase turbulence due to complex wake interactions. It has been observed that small Stokes number particles enhance the energy in the high wavenumber range of the energy spectrum while high Stokes number particles damp the energy at all scales. This observation motivates the need for polydispersed two-way coupled simulations. While some polydispersed simulations were carried out by the author (not reported here), a more detailed analysis can form a fruitful area of research in the future.

A point-particle assumption has been made in the present work. A more realistic analysis would involve modeling the wakes behind individual particles. With the present computing power, such

an analysis is limited to very few particles [78, 79] but with advent of new computing technology (e.g. graphics processor units etc.) it may be possible to conduct more statistically useful simulations. Recent work by Xu and Subramaniam [80] has provided guidelines on consistent modeling of interphase momentum transfer in point-particle DNS and these guidelines should be examined in future work.

Also, the charged particle work reported in the present study has been limited to one-way coupling. This work can be extended using two-way coupling. Such work would yield further insight into the amount of charge required to mitigate preferential accumulation at high particle mass loadings. It has been observed that the RDF obtained from the present simulations closely matches the functional form of the RDF for settling charged particles proposed by Shaw et al. [9]. In the future, simulations could be used to estimate the matching constants in the theoretical model. Thus simulations hold the potential to aid further development of the drift diffusion model for clustering of inertial particles.

6.2.2 Collision models

The present study has neglected particle-particles collisions. In the future work, the collision algorithm outlined by Sundaram and Collins [41] may be incorporated in PANDORA to enable studies on collision statistics. Simulations at high volume loadings may be set up with a view to aid development of better models [81] for prediction of collision frequency at different fluid and particle parameters. Such a study may lead to improved models for coalescence of sub-micron droplets in clouds leading to warm rain initiation. Previous studies have shown that the RDF is of primary importance in determining the collision frequency of droplets. In the present work, the RDF has been reported under different conditions of gravity and future theoretical models could benefit by comparing the expected behavior with DNS results from the present study. Thus the present work could also aid in development of theoretical models for particle collisions.

6.2.3 Large eddy simulation

All the work reported in the present study used DNS technique to simulate fluid turbulence. Though this lends accuracy to the fluid statistics, the Reynolds numbers feasible using this technique are very limited. In order to move closer to real-world Reynolds numbers, it would be useful to employ the large-eddy simulation (LES) technique. However implementation of LES for dispersed phase flows is not as straightforward as in single phase flows. Since sub-grid scale fluctuations can potentially have a significant effect on particle trajectories, a robust model would be required to account for the effect of sub-grid scales on particle motion. The need to account for the effect of sub-grid fluctuations on particle motion has been highlighted by Shotorban and Mashayek [82] using LES of particle-laden decaying isotropic turbulence. LES of two-way coupled particle-laden flows by Boivin et al. [83] have pointed out that the dynamic mixed subgrid model yields the best results when the particle response time is greater than the characteristic time of subgrid-scale turbulence. Studies have pointed out that while particle dispersion is affected only when a significant amount of energy is removed from the velocity field, accumulation and collision phenomena are significantly affected when particle response times are comparable to the Lagrangian integral timescale measured along particle trajectories [84, 85]. Future work incorporating LES in PANDORA may benefit from the insights gathered in the studies cited here.

6.2.4 Homogeneous anisotropic turbulence

The present work considers only homogeneous isotropic turbulence and thus is not applicable in situations involving strong mean velocity gradients. As a first step towards making PANDORA more generally applicable, it has been extended by the author to simulate plane strain and linear shear cases following the algorithm of Rogallo [24]. More work is needed in the future to validate the solver for both fluid and particle statistics. Here a few studies of particle-laden homogeneous shear and plane strain flows are cited which can be used for validating PANDORA in the future. Ahmed and Elghobashi [86] reported results on dispersion and preferential accumulation of particles in DNS of homogeneous shear flow. Ahmed and Elghobashi [87] also examined mechanisms of two-way coupling in homogeneous shear flows. A recent study by Gualtieri et al. [88] has fo-

cused on preferential accumulation and orientation of particle clusters in homogeneous shear flow. Dispersion of particles in homogeneous plane strain turbulent flows has been studied by Barre et al. [89]. One of the limitations in these simulations is that the integral length scale continues to increase indefinitely. Thus the simulation can be run only for a limited time thus limiting the time over which accurate statistics can be gathered. Also some of the situations like plane strain lead to loss of particles in area of interest and a large number of particles (or many stochastic simulations) may be required to generate robust statistics.

Simulation of homogeneous dispersed phase flows involving mean velocity gradients are invaluable for developing Eulerian models for such flows. The closure terms for such models require estimation of correlations between the particle diameter and fluid velocity sampled by the particles. DNS of homogeneous flows is an invaluable tool to estimate these closure terms. Aiding Eulerian modeling of dispersed phase flows in future has been a significant motivation for present work and future work is expected to focus on this aspect. Sengupta et al. [90] have reported a comprehensive data bank for both monodispersed and polydispersed homogeneous dispersed flows which could be useful for model development and validation in the future. The study by Pandya and Mashayek [91] is one of the encouraging attempts at developing closure models for dispersed flows using DNS data.

Appendix A

Publications

- Karnik, A. U., Shrimpton J. S., *Destruction of Preferential Accumulation by Lorentz force interaction*, 22^{nd} European conference on Liquid Atomization and Spray Systems, Sep.8-10, 2008, Italy.
- Scott, S.J., Karnik, A.U., Shrimpton, J.S., *On the Quantification of Preferential Accumulation*, International Journal of Heat and Fluid Flow, Vol. 30(4), 789-795, 2009.
- Karnik, A. U., Shrimpton J. S., *Mitigation of Preferential Concentration of Small Inertial Particles in Stationary Isotropic Turbulence Using Electrical and Gravitational Body Forces*, Accepted for publication in Physics of Fluids.

References

[1] S. J. Scott. *A PDF Based Method for Modelling Polysized Particle Laden Turbulent Flows Without Size Class Discretization.* PhD thesis, Imperial College London, 2006.

[2] S. Elghobashi. On predicting particle-laden turbulent flows. *Applied Scientific Research*, 52 (4):309–329, 1994.

[3] J. R. Fessler, J. D. Kulick, and J. K. Eaton. Preferential concentration of heavy-particles in a turbulent channel flow. *Physics of Fluids*, 6(11):3742–3749, 1994.

[4] A. M. Wood, W. Hwang, and J. K. Eaton. Preferential concentration of particles in homogeneous and isotropic turbulence. *International Journal of Multiphase Flow*, 31(10-11):1220–1230, 2005.

[5] J. Bec, L. Biferale, M. Cencini, A. Lanotte, S. Musacchio, and F. Toschi. Heavy particle concentration in turbulence at dissipative and inertial scales. *Physical Review Letters*, 98(8), 2007.

[6] R. C. Hogan and J. N. Cuzzi. Stokes and reynolds number dependence of preferential particle concentration in simulated three-dimensional turbulence. *Physics of Fluids*, 13(10):2938–2945, 2001.

[7] M. van Aartrijk and H. J. H. Clercx. Preferential concentration of heavy particles in stably stratified turbulence. *Physical Review Letters*, 100(25), 2008.

[8] J. Lu, H. Nordsiek, E. W. Saw, and R. A. Shaw. Clustering of charged inertial particles in turbulence. *Physical Review Letters*, 104(18):184505(1)–184505(4), 2010.

[9] R. A. Shaw, J. A. Lu, and H. Nordsiek. Clustering of settling charged particles in turbulence: theory and experiments. *New Journal of Physics*, 12, 2010.

[10] P. K. Yeung and S. B. Pope. Lagrangian statistics from direct numerical simulations of isotropic turbulence. *Journal of Fluid Mechanics*, 207:531–586, 1989.

[11] R. A. Shaw. Particle-turbulence interactions in atmospheric clouds. *Annual Review of Fluid Mechanics*, 35:183–227, 2003.

[12] J. N. Cuzzi, R. C. Hogan, J. M. Paque, and A. R. Dobrovolskis. Size-selective concentration of chondrules and other small particles in protoplanetary nebula turbulence. *Astrophysical Journal*, 546(1):496–508, 2001.

[13] L. P. Wang and M. R. Maxey. Settling velocity and concentration distribution of heavy-particles in homogeneous isotropic turbulence. *Journal of Fluid Mechanics*, 256:27–68, 1993.

[14] M. R. Maxey. The gravitational settling of aerosol-particles in homogeneous turbulence and random flow-fields. *Journal of Fluid Mechanics*, 174:441–465, 1987.

[15] C. Crowe, M. Sommerfeld, and Y. Tsuji. *Multiphase flows with droplets and particles*. CRC Press, 1998.

[16] K. R. Sreenivasan. Fluid turbulence. *Rev. Mod. Phys.*, 71:S383–S395, 1999.

[17] G. K. Batchelor and I. Proudman. The effect of rapid distortion of a fluid in turbulent motion. *Quart. Journ. Mech. and Applied Math.*, 7(1), 1954.

[18] A. N. Kolmogorov. Local structure of turbulence in an incompresible fluid at very high reynolds numbers. *C. R. Acad. Sci. USSR*, 30:201, 1941.

[19] P. Moin and K. Mahesh. Direct numerical simulation: A tool in turbulence research. *Annual Review of Fluid Mechanics*, 30:539–578, 1998.

[20] F. Mashayek and R. V. R. Pandya. Analytical description of particle/droplet-laden turbulent flows. *Progress in Energy and Combustion Science*, 29(4):329–378, 2003.

[21] R. S. Rogallo and P. Moin. Numerical simulation of turbulent flows. *Annual Review of Fluid Mechanics*, 16:99–137, 1984.

[22] S. A. Orszag and G. S. Patterson. Numerical simulation of three-dimensional homogeneous isotropic turbulence. *Physical Review Letters*, 28(2):76–79, 1972.

[23] J. J. Riley and G. S. Patterson. Diffusion experiments with numerically integrated isotropic turbulence. *Physics of Fluids*, 17(2):292–297, 1974.

[24] R. S. Rogallo. Numerical experiments in homogenous turbulence. Technical Memorandum NASA-TM-81315, NASA, 1981.

[25] S. A. Orszag. Spectral methods for problems in complex geometries. *Journal of Computational Physics*, 37(1):70–92, 1980.

[26] C. Canuto, M. Y. Hussaini, A. Quarteroni, and T. A. Zang. *Spectral methods in fluid dynamics*. Springer series in computational physics. Springer-Verlag, 1988.

[27] M. Frigo and S. G. Johnson. The design and implementation of FFTW3. In *Proceedings of the IEEE*, volume 93, pages 216–231, 2005.

[28] V. Eswaran and S. B. Pope. An examination of forcing in direct numerical simulations of turbulence. *Computers & Fluids*, 16(3):257–278, 1988.

[29] P. K. Yeung, S. B. Pope, and B. L. Sawford. Reynolds number dependence of lagrangian statistics in large numerical simulations of isotropic turbulence. *Journal of Turbulence*, 7(58):1–12, 2006.

[30] M. R. Overholt and S. B. Pope. Direct numerical simulation of a passive scalar with imposed mean gradient in isotropic turbulence. *Physics of Fluids*, 8(11):3128–3148, 1996.

[31] M. R. Maxey and J. J. Riley. Equation of motion for a small rigid sphere in a uniform flow. *Phys. Fluids*, 26:883–889, 1983.

[32] S. Elghobashi and G. C. Truesdell. Direct simulation of particle dispersion in a decaying isotropic turbulence. *Journal of Fluid Mechanics*, 242:655–700, 1992.

[33] J. Ferziger and M. Peric. *Computational methods for fluid dynamics*. Springer Verlag, 1996.

[34] C. T. Crowe. Numerical models for dilute gas-particle flows. *Journal of Fluids Engineering*, 104:297–303, 1982.

[35] M. Boivin, O. Simonin, and K. D. Squires. Direct numerical simulation of turbulence modulation by particles in isotropic turbulence. *Journal of Fluid Mechanics*, 375:235–263, 1998.

[36] G. I. Taylor. Statistical theory of turbulence. *Proceedings of the Royal Society of London. Series A, Mathematical and Physical Sciences*, 151:421–444, 1935.

[37] K. D. Squires and J. K. Eaton. Preferential concentration of particles by turbulence. *Physics of Fluids A-Fluid Dynamics*, 3(5):1169–1179, 1991.

[38] R. M. Kerr. Higher-order derivative correlations and the alignment of small-scale structures in isotropic numerical turbulence. *Journal of Fluid Mechanics*, 153, 1985.

[39] L. P. Wang, A. S. Wexler, and Y. Zhou. Statistical mechanical description and modelling of turbulent collision of inertial particles. *Journal of Fluid Mechanics*, 415:117–153, 2000.

[40] L. R. Collins and A. Keswani. Reynolds number scaling of particle clustering in turbulent aerosols. *New Journal of Physics*, 6, 2004.

[41] S. Sundaram and L. R. Collins. Collision statistics in an isotropic particle-laden turbulent suspension .1. Direct numerical simulations. *Journal of Fluid Mechanics*, 335:75–109, 1997.

[42] W. C. Reade and L. R. Collins. Effect of preferential concentration on turbulent collision rates. *Physics of Fluids*, 12(10):2530–2540, 2000.

[43] E. W. Saw, R. A. Shaw, S. Ayyalasomayajula, P. Y. Chuang, and A. Gylfason. Inertial clustering of particles in high-Reynolds-number turbulence. *Physical Review Letters*, 100(21):214501(1)–214501(4), 2008.

[44] P. Grassberger and I. Procaccia. Measuring the strangeness of strange attractors. *Physica D*, 9 (1-2):189–208, 1983.

[45] L. Tang, F. Wen, Y. Yang, C. T. Crowe, J. N. Chung, and T. R. Troutt. Self-organizing particle dispersion mechanism in a plane wake. *Physics of Fluids a-Fluid Dynamics*, 4(10):2244–2251, 1992.

[46] C. T. Crowe, J. N. Chung, and T. R. Troutt. Particle mixing in free shear flows. *Progress in Energy and Combustion Science*, 14(3):171–194, 1988.

[47] D. W. I. Rouson and J. K. Eaton. On the preferential concentration of solid particles in turbulent channel flow. *Journal of Fluid Mechanics*, 428:149–169, 2001.

[48] H. Yoshimoto and S. Goto. Self-similar clustering of inertial particles in homogeneous turbulence. *Journal of Fluid Mechanics*, 577:275–286, 2007.

[49] A. Aliseda, A. Cartellier, F. Hainaux, and J. C. Lasheras. Effect of preferential concentration on the settling velocity of heavy particles in homogeneous isotropic turbulence. *Journal of Fluid Mechanics*, 468:77–105, 2002.

[50] J. K. Eaton and J. R. Fessler. Preferential concentration of particles by turbulence. *International Journal of Multiphase Flow*, 20:169–209, 1994.

[51] G. R. Ruetsch and M. R. Maxey. The evolution of small-scale structures in homogeneous isotropic turbulence. *Physics of Fluids A-Fluid Dynamics*, 4(12):2747–2760, 1992.

[52] Y. Zhou, A. S. Wexler, and L. P. Wang. On the collision rate of small particles in isotropic turbulence. ii. Finite inertia case. *Physics of Fluids*, 10(5):1206–1216, 1998.

[53] J. H. Chun, D. L. Koch, S. L. Rani, A. Ahluwalia, and L. R. Collins. Clustering of aerosol particles in isotropic turbulence. *Journal of Fluid Mechanics*, 536:219–251, 2005.

[54] J. P. L. C. Salazar, J. De Jong, L. J. Cao, S. H. Woodward, H. Meng, and L. R. Collins. Experimental and numerical investigation of inertial particle clustering in isotropic turbulence. *Journal of Fluid Mechanics*, 600:245–256, 2008.

[55] G. Boffetta, F. De Lillo, and A. Gamba. Large scale inhomogeneity of inertial particles in turbulent flows. *Physics of Fluids*, 16(4):L20–L23, 2004.

[56] E. Balkovsky, G. Falkovich, and A. Fouxon. Intermittent distribution of inertial particles in turbulent flows. *Physical Review Letters*, 86(13):2790–2793, 2001.

[57] M. I. Yudine. Physical considerations on heavy-particle diffusion. *Atmospheric Diffusion and Air pollution: Adv. Geophys.*, 6:185–191, 1959.

[58] G. T. Csanady. Turbulent diffusion of heavy particles in the atmosphere. *Journal of the Atmospheric Sciences*, 20(3):201–208, 1963.

[59] S. Goto and J. C. Vassilicos. Self-similar clustering of inertial particles and zero-acceleration points in fully developed two-dimensional turbulence. *Physics of Fluids*, 18(11):115103(1)–115103(10), 2006.

[60] L. Chen, S. Goto, and J. C. Vassilicos. Turbulent clustering of stagnation points and inertial particles. *Journal of Fluid Mechanics*, 553:143–154, 2006.

[61] S. Goto and J. C. Vassilicos. Sweep-stick mechanism of heavy particle clustering in fluid turbulence. *Physical Review Letters*, 100(5):4, 2008.

[62] J. Bellan and K. Harstad. Turbulence effects during evaporation of drops in clusters. *International Journal of Heat and Mass Transfer*, 31(8):1655–1668, 1988.

[63] J. Bellan. A new approach to soot control in diesel engines by fuel-drop charging. *Combustion and Flame*, 51:117–119, 1983.

[64] A. R. H. Rigit and J. S. Shrimpton. Spray characteristics of charged injection electrostatic atomizers with small orifice diameters. *Atomization and Sprays*, 16:421–442, 2006.

[65] J. S. Shrimpton and A. J. Yule. Characterisation of charged hydrocarbon sprays for application in combustion systems. *Experiments in Fluids*, 26(5):460–469, 1999.

[66] V. M. Alipchenkov, L. I. Zaichik, and O. F. Petrov. Clustering of charged particles in isotropic turbulence. *High Temperature*, 42(6):919–927, 2004.

[67] S. Balachandar and J. K. Eaton. Turbulent dispersed multiphase flow. *Annual Review of Fluid Mechanics*, 42:111–133, 2010.

[68] R. A. Gore and C. T. Crowe. Modulation of turbulence by a dispersed phase. *Journal of Fluids Engineering-Transactions of the Asme*, 113(2):304–307, 1991.

[69] W. T. Hwang and J. K. Eaton. Homogeneous and isotropic turbulence modulation by small heavy (St $\approx$ 50) particles. *Journal of Fluid Mechanics*, 564:361–393, 2006.

[70] K. D. Squires and J. K. Eaton. Particle response and turbulence modification in isotropic turbulence. *Physics of Fluids*, 2(7):1191–1203, 1990.

[71] T. S. Yang and S. S. Shy. Two-way interaction between solid particles and homogeneous air turbulence: particle settling rate and turbulence modification measurements. *Journal of Fluid Mechanics*, 526:171–216, 2005.

[72] F. Lucci, A. Ferrante, and S. Elghobashi. Modulation of isotropic turbulence by particles of taylor length-scale size. *Journal of Fluid Mechanics*, 650:5–55, 2010.

[73] S. Elgobashi and G. C. Truesdell. On the two-way interaction between homogeneous turbulence and dispersed solid particles. i: Turbulence modification. *Physics of Fluids*, 5(7): 1790–1801, 1993.

[74] G. C. Truesdell and S. Elgobashi. On the two-way interaction between homogenous turbulence and dispersed solid particles. ii. particle dispersion. *Physics of Fluids*, 6(3):1405–1407, 1994.

[75] C. T. Crowe, T. R. Troutt, and J. N. Chung. Numerical models for two-phase turbulent flows. *Annual Review of Fluid Mechanics*, 28:11–43, 1996.

[76] R. C. Hogan and J. N. Cuzzi. Cascade model for particle concentration and enstrophy in fully developed turbulence with mass-loading feedback. *Physical Review E*, 75(5):056305(1)–056305(9), 2007.

[77] J. K. Eaton. Two-way coupled turbulence simulations of gas-particle flows using point-particle tracking. *International Journal of Multiphase Flow*, 35(9):792–800, 2009.

[78] P. Bagchi and S. Balachandar. Response of the wake of an isolated particle to an isotropic turbulent flow. *Journal of Fluid Mechanics*, 518:95–123, 2004.

[79] A. Ten Cate, J. J. Derksen, L. M. Portela, and H. E. A. Van Den Akker. Fully resolved simulations of colliding and monodisperse spheres in forced isotropic turbulence. *Journal of Fluid Mechanics*, 519:233–271, 2004.

[80] Y. Xu and S. Subramaniam. Consistent modeling of interphase turbulent kinetic energy transfer in particle-laden turbulent flows. *Physics of Fluids*, 19(8):085101, 2007.

[81] L. I. Zaichik, O. Simonin, and V. M. Alipchenkov. Two statictical models for predicting collision rates of inertial particles in homogeneous isotropic turbulence. *Physics of Fluids*, 15(10): 2995–3005, 2003.

[82] B. Shotorban and F. Mashayek. A stochastic model for particle motion in large eddy simulation. *Journal of Turbulence*, 7(18):1–13, 2006.

[83] M. Boivin, O. Simonin, and K. D. Squires. On the prediction of gas-solid flows with two-way coupling using large eddy simulation. *Physics of Fluids*, 12(8):2080–2090, 2000.

[84] V. Armenio, U. Piomelli, and V. Fiorotto. Effect of the subgrid scales on particle motion. *Physics of Fluids*, 11(10):3030–3042, 1999.

[85] P. Fede and O. Simonin. Numerical study of the subgrid fluid turbulence effects on the statistics of heavy colliding particles. *Physics of Fluids*, 18(4):045103, 2006.

[86] A. M. Ahmed and S. Elghobashi. Direct numerical simulation of particle dispersion in homogeneous turbulent shear flows. *Physics of Fluids*, 13(11):3346–3364, 2001.

[87] A. M. Ahmed and S. Elghobashi. On the mechanisms of modifying the structure of turbulent homogeneous shear flows by dispersed particles. *Physics of Fluids*, 12(11):2906–2930, 2000.

[88] P. Gualtieri, F. Picano, and C. M. Casciola. Anisotropic clustering of inertial particles in homogeneous shear flow. *Journal of Fluid Mechanics*, 629:25–39, 2009.

[89] C. Barre, F. Mashayek, and D. B. Taulbee. Statistics in particle-laden plane strain turbulence by direct numerical simulation. *International Journal of Multiphase Flow*, 27(2):347–378, 2001.

[90] K. Sengupta, K. Russell, W. J. Minkowycz, and F. Mashayek. Numerical simulation data for assessment of particle-laden turbulent flow models. *International Journal of Heat and Mass Transfer*, 48(15):3035–3046, 2005.

[91] R. V. R. Pandya and F. Mashayek. Non-isothermal dispersed phase of particles in turbulent flow. *Journal of Fluid Mechanics*, 475:205–245, 2003.